POLITECNICO DI TORINO

UPC EEBE

MASTER'S DEGREE IN MECHANICAL ENGINEERING

Politecnico di Torino

UNIVERSITAT POLITÈCNICA DE CATALUNYA BARCELONATECH

MASTER'S DEGREE THESIS

DEVELOPMENT OF A DATA PROCESSING TOOL FOR AI-BASED SENSORS IN CONDITION MONITORING OF REVERSIBLE PUMP-TURBINES

Supervisors

Prof. DANIELA ANNA MISUL

Prof. MAGDA RUIZ

Prof. ALFREDO ZABALETA

Candidate

VALERIO VALENTI

10 APRIL 2026

Abstract

Renewable energies represent one of the most effective responses to the environmental and energy challenges of our time. The transition to clean energy sources has become a necessity to reduce CO2 emissions. These technologies stand out for their ability to harness inexhaustible natural resources, such as the sun, wind, Earth's heat, and water. Among the oldest and most efficient renewable sources is hydroelectric energy, which utilizes the power of water to generate electricity. This technology, based on the use of rivers and water reservoirs, has enabled energy production in a reliable and sustainable way for centuries. Today, it is one of the leading resources for global energy production, accounting for more than 15% of the world's electricity. In recent years, the power grid has been increasingly supplied with energy generated from renewable sources. Hydropower stands out as one of the most reliable and high-quality energy sources. Water reservoirs associated with dams can be conceptually likened to large-scale energy storage systems, where energy is released on demand through the controlled discharge of water masses across hydroelectric turbines. Hydroelectric turbines are engineered to operate within specific design parameters that ensure optimal efficiency and structural integrity. However, deviations from these optimal conditions, known as off-design conditions, can lead to significant challenges. Such conditions often result in mechanical vibrations and complex fluid dynamic phenomena, including turbulence and vortex formation, which adversely affect turbine performance and longevity. These instabilities cause pressure fluctuations and unsteady forces on turbine components, contributing to mechanical vibrations and potential structural damage. To address these challenges, the research project **STOR-HY**, funded under the Horizon Europe programme was established with the overarching goal of developing an AI-based virtual sensor for turbine monitoring. Within this broader context, the specific contribution of this thesis represents the initial phase of the project, establishing the data processing foundation upon which the virtual sensor will be based. Through the spectral analysis of experimental vibration data, this study focuses on feature extraction and the definition of condition-monitoring thresholds. By identifying the frequency patterns associated with off-design instabilities, the developed tool provides the essential preliminary signal-processing steps. This ensures that the future AI sensor will be trained on robust, physically meaningful data, allowing for a preventive approach to structural monitoring and maintenance.

Table of Contents

List of Figures

List of Tables

Acronyms

RE	Renewable Energy.
PHES	Pumped Hydro Energy Storage.
SHP	Small Hydropower Plant.
CRHP	Cascaded Reservoir Hydropower Plant.
BEP	Best Efficiency Point.
PT	Pump Turbine.
RSI	Rotor Stator Interaction.
ND	Nodal Diameter.
VS	Vaneless Space.
BPF	Blade Passing Frequency.
FEM	Finite Element Model.
AE	Acoustic Emission.
PL	Part-Load.
HL	High-Load.
FFT	Fast Fourier Transform.
ANN	Artificial Neural Network.
MLP	Multi-Layer Perceptron.

MLR	Multivariate Linear Regression.
LOWESS	Locally Weighted Scatterplot Smoothing.
SDI	Scattered Data Interpolation.
MSE	Mean Squared Error.
RMS	Root Mean Square.
preR^2	Predicted Determination Coefficient.
LM	Levenberg–Marquardt.

List of Symbols

p	Pressure [Pa]
ρ	Water density [kg/m^3]
g	Gravitational acceleration [m/s^2]
γ	Specific weight of the fluid [N/m^3]
m	Mass [kg]
L_i	Internal work per unit mass [N]
L_w	Work of resistance per unit mass [N]
$(L_i)_{\mathbf{obt}}$	Internal work obtained from the fluid per unit mass [N]
Δh	Variation of the enthalpy per unit mass [J/kg]
η	Efficiency
η_y	Hydraulic efficiency of the turbine
η_C	Efficiency of the penstock
η_v	Volumetric efficiency of the penstock
η_m	Mechanical efficiency
η_t	Total efficiency
η_g	Global efficiency
Q	Volumetric flow rate [m^3/s]
$\dot{m}$	Mass flow rate [kg/s]
H	Net geodetic head [m]
H_O	Total head [m]
H_D	Available head [m]
H_W	Head losses in the turbine [m]
Y	Head loss in the penstock [m]
T	Torque produced by the runner [Nm]
ω	Angular velocity of the runner [rad/s]
χ	Degree of reaction (dimensionless)
f	Frequency [Hz]
P	Power output [W]
P_i	Internal power [W]
P_u	Useful power [W]
A	Area of the section [m^2]
p_1, p_2	Static pressure
u_1, u_2	Peripheral velocities at runner outlet (1) and inlet (2) [m/s]

c_1, c_2	Absolute velocity vectors of water at inlet (1) and outlet (2) [m/s]
c_{u1}, c_{u2}	Tangential components of c_1 and c_2 [m/s]
c_{m1}, c_{m2}	Axial components of c_1 and c_2 [m/s]
w_1, w_2	Relative velocity vectors of fluid with respect to the runner [m/s]
α_1, α_2	Angles between the absolute velocity and tangential direction [deg]
r_1, r_2	Radii at outlet and inlet of runner [m]
z_1, z_2	Elevation of the section measured with respect to a vertical z-axis
P_F	Mechanical power of the Francis turbine [W]
n_s	Specific speed (dimensionless)
n_c	Characteristic speed (dimensionless)
Z_r	Number of rotor blade
Z_s	Number of stator blade

Chapter 1

Introduction to Renewable Energy Systems

1.1 Overview of Renewable Hydropower Systems

Due to the increasing global demand, especially in both developed and developing countries, there is a growing need for more sustainable energy technologies to replace conventional electricity generation resources, such as fossil fuels. Fossil fuel-based energy sources have contributed significantly to environmental issues, including global warming and climate change, with greenhouse gas emissions from power generation having risen exponentially over the past few decades. To mitigate this ongoing environmental crisis, Renewable Energy (RE) technologies such as solar, wind, hydro, biomass, geothermal, and hydrogen have been introduced as viable alternatives for electricity generation. These technologies are gaining increased attention because of their environmentally friendly characteristics and their capacity to produce power with little to no emissions of harmful pollutants, a feature that aligns with the growing societal awareness of the need for a clean environment.

Renewable energy technologies also offer significant economic benefits. They contribute to economic sustainability by reducing the costs of electricity generation, utilizing natural and renewable resources. Furthermore, RE can serve as a secondary source of income, as consumers have the opportunity to sell surplus electricity back to the grid. Despite the increasing adoption of RE sources for power generation, fossil fuels remain dominant in the global energy mix, primarily due to the intermittent nature of renewable energy sources and the high initial costs associated with their implementation. For instance, photovoltaic systems can only operate during daylight hours, wind turbines depend on adequate airflow, and hydro turbines function only when there is sufficient water flow to generate potential energy. Consequently, researchers worldwide are actively investigating ways to enhance the efficiency of RE technologies and address the challenges associated with their intermittent nature [1]. Intermittent renewable energy sources, such as wind and solar power, are characterized by highly fluctuating, unpredictable, and dispersed energy production. This variability significantly restricts their integration into the grid, primarily due

to the considerable challenges it poses in maintaining a stable equilibrium between energy supply and demand. As renewable energy production continues to rise, the potential for a green energy transition is clear. However, the deployment of this vast potential remains constrained by the intermittent and unpredictable nature of these sources, which complicates grid stability, safety, and efficiency. The electricity grid must be capable of constantly matching supply with demand, yet this balance becomes more difficult as renewable energy integration increases. To fully unlock the potential of renewable energy and meet carbon-free electricity generation goals, the grid must be operated smartly, incorporating greater energy storage capacity, for instance. This will enable the grid to better manage fluctuations in supply and maintain reliability, paving the way for a more sustainable and resilient energy future [2].

Hydropower is one of the most reliable and widely used forms of renewable energy, as it harnesses the kinetic and potential energy of water flowing from higher to lower elevations. Hydroelectricity generation typically involves diverting water from a river through a turbine to produce electricity, and some systems include dams that store large volumes of water to ensure continuous energy production. Compared to other renewable energy sources, hydropower offers the highest energy conversion efficiency, reaching approximately 90%. Today, hydropower is produced in 159 countries and generates around 4100 TWh annually (as of 2016), which accounts for nearly 17% of global electricity production and approximately 70% of all renewable electricity generation. This contribution exceeds that of nuclear energy (9.8%) and is more than double the combined output of all other renewable sources (7.9%) [3]. Various types of hydropower systems exist to meet different energy needs, including pumped hydro energy storage systems, small hydropower plants, cascaded reservoir hydropower plants and hydrokinetic systems.

1.1.1 Pumped Hydro Energy Storage

Pumped hydro energy storage (PHES) is the most largely used energy storage technology in the world today, representing roughly 97% of the energy stored every year, with about 300 GW installed. This energy storage concept uses a combination of turbomachinery equipment, electrical equipment, water reservoirs, piping, and large civil engineering facilities [4]. PHES is a type of hydroelectric storage system that consists of two water reservoirs located at different elevations. The system employs a reversible turbine, capable of functioning both as a generator and as a pump [5]. During electricity generation, water flows from the upper to the lower reservoir, driving the turbine to produce electricity. Conversely, during low demand periods or when electricity prices are low, the turbine operates in reverse acting as a pump using electricity to move water from the lower reservoir back to the upper one, effectively recharging the system's energy storage.

Typically, power generation occurs during peak demand hours, while pumping operations are performed when electricity is abundant or cheaper. Although PHES

systems can reach generation efficiencies of up to 90%, the round-trip efficiency accounting for both pumping and generating phases is approximately 80%, implying that about 20% of the input energy is lost in the full cycle. The energy in a hydroelectric system refers to the amount of potential energy stored in the upper reservoir, while the power capacity indicates the maximum rate at which this energy can be converted into electricity. As illustrated in Figure 1.1 and Figure 1.2, PHES systems can be classified into two main types: open-loop systems, which are connected to natural water bodies, and closed-loop systems, which are isolated from natural water sources. PHES preserves most of the advantages of hydropower plants, even if PHES is not considered a renewable energy source as such. Especially for closed-loop configurations, which consist of two reservoirs that are isolated from a free-flowing water source, the generated energy comes solely from the storage of a second energy source that is not necessarily renewable. On the other hand, closed-loop systems have fewer environmental impacts because, after the initial filling of the reservoir, there is almost no transfer of water from a free-flowing source, thereby greatly reducing environmental impacts [6, 7].

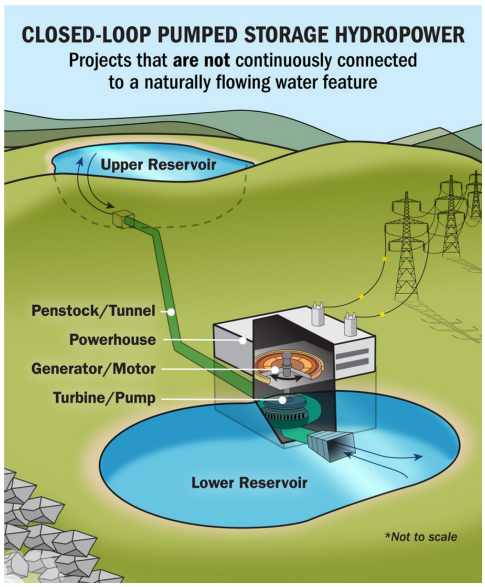

Figure 1.1: Closed-loop pumped storage hydropower [8]

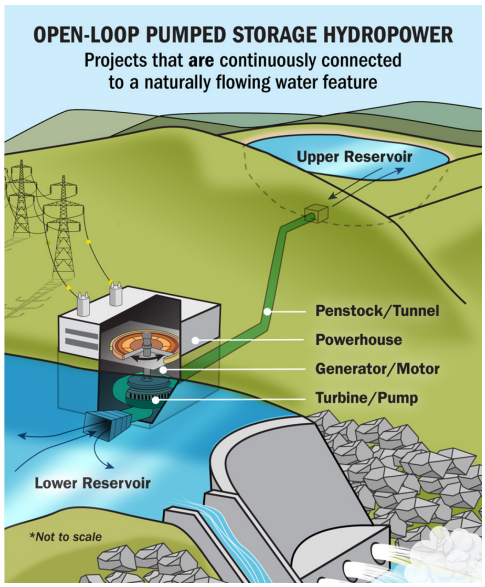

Figure 1.2: Open-loop pumped storage hydropower [8]

1.1.2 Small Hydropower Plants

Small-scale hydropower plants (SHPs) are among the most affordable renewable energy solutions, especially when it comes to supplying electricity to remote or rural areas in developing regions. They also serve as a promising foundation for future advancements in the hydropower sector. These systems typically operate using a run-of-river approach, which means they utilize the natural flow of a river without the need for large reservoirs [9]. As a result, they generally cause minimal environmental disturbance. The classification of what constitutes a "small" hydropower plant varies internationally, depending on each country's regulations and administrative

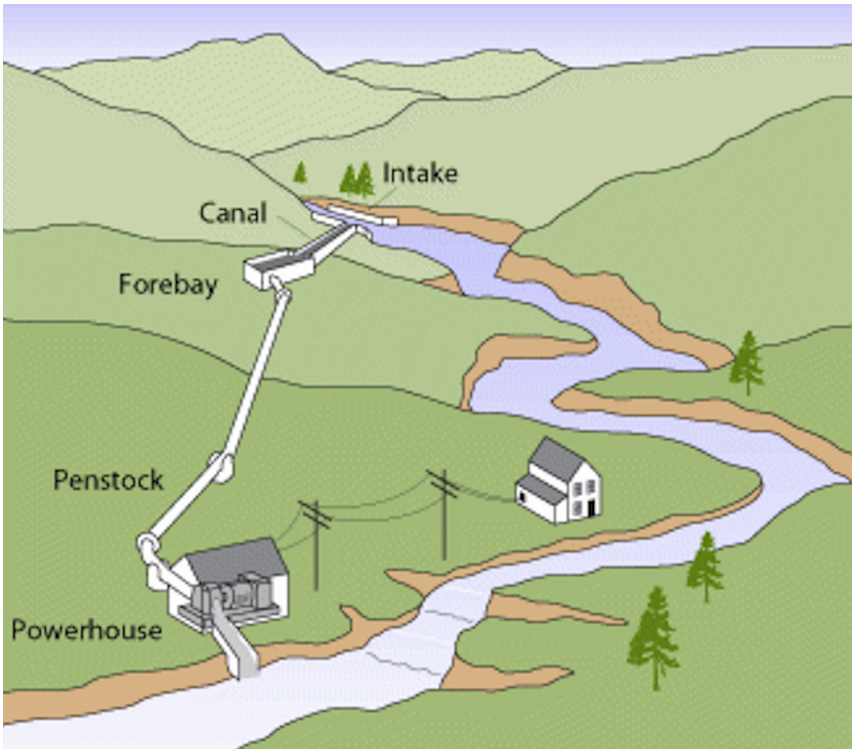

Figure 1.3: Schematic of a small hydropower palant [11]

frameworks. A standard SHP layout involves diverting river water through an intake structure integrated into a weir, which includes a control valve. When the plant is not operational, the valve can be closed to allow river water to bypass the system entirely. To prevent efficiency losses and avoid damage to the hydro turbines, a settling tank is typically installed upstream of the intake. This structure helps remove suspended particles and debris from the river water before it enters the system. Thanks to their adaptability, SHPs can be deployed even in locations with low water flow. They play an important role in providing sustainable and cost-effective energy solutions for both residential and commercial users, while also preserving local ecosystems [10].

1.1.3 Cascaded Reservoir Hydropower Plant

Cascaded reservoir hydropower plants (CRHPs) are systems that use a series of reservoirs placed at different elevations to generate electricity more than once as water flows downstream. The setup can vary in complexity—from simple arrangements with two reservoirs to intricate networks—depending on the landscape. These systems not only produce energy efficiently but also support additional functions like water supply, flood control, and irrigation. CRHPs can operate using sustained water flow, accumulated rainwater, or recycled water, offering flexibility and environmental benefits [12].

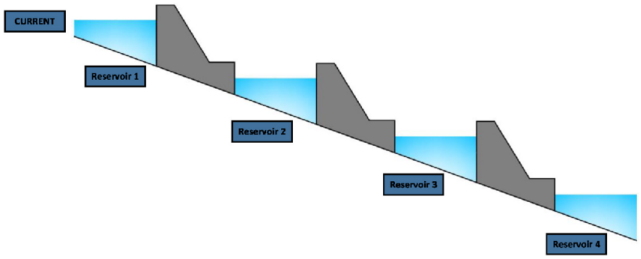

Figure 1.4: Cascaded-Reservoir-Hydropower-Plant-System [1]

1.1.4 Hydrokinetic

Hydrokinetic energy conversion is an emerging renewable energy solution, yet it still presents ambiguity in terms of technology classification, applications, and conversion principles. Generally, a hydrokinetic system consists of an electromechanical device that captures the kinetic energy from moving water such as river or tidal flows and converts it into electricity. These systems typically include a turbine rotated by flowing water and directly coupled to a permanent magnet synchronous generator, without the need for a gearbox. The generated electrical energy is then processed by a power electronics unit for storage or grid integration. The efficiency of hydrokinetic systems depends on various factors, including fluid density, cross sectional area, and the cube of the fluid's velocity. However, mechanical, hydrodynamic, and electrical losses inevitably reduce the overall output. Although turbine-based systems remain the most commonly deployed conversion method, there is growing interest in exploring non turbine alternatives, as ongoing research continues to refine and diversify energy harvesting strategies. Importantly, hydrokinetic systems require no reservoirs or dams, making them compact, easy to install, and minimally invasive to the environment. They are typically deployed in fast flowing rivers, mounted on floating pontoons or anchored to fixed structures, and are increasingly used in decentralized or off-grid energy applications [13].

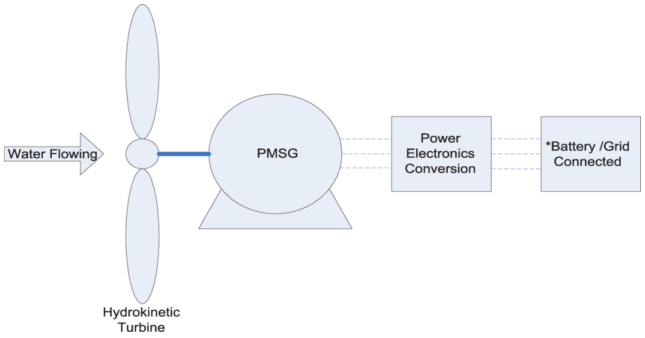

Figure 1.5: Schematic of a hydrokinetic system [13]

1.2 The STOR-HY European Project

As previously highlighted, the surge in unpredictable and intermittent renewable energy sources requires PHS plants to continuously balance the grid. This intensified demand places a severe strain on the mechanical components of hydraulic turbines, which are forced to withstand an increased number of start-stop cycles, demanding ramping duties, and rapid transitions between energy generation and storage modes. Operating frequently in these "off-design" conditions leads to accelerated deterioration, increased operating costs, and unexpected damage to critical equipment.

To address these critical challenges, the present thesis was developed within the framework of **STOR-HY**, a major European research initiative funded by the European Union's Horizon programme, coordinated by the Universitat Politècnica de Catalunya (UPC).

The overarching objective of the **STOR-HY** project is to reduce the capital and operating expenditures (CAPEX and OPEX) of innovative pumped storage projects by improving the lifetime and recyclability of their components. To mitigate the accelerated wear and tear caused by modern grid demands, there is a crucial need for accurate degradation models and advanced control methods. **STOR-HY** tackles this by developing advanced sensor-based condition monitoring systems and a Cyber-physical platform for Advanced Decision Support (CADS). These technologies aim to detect early failure mechanisms, postpone unnecessary maintenance actions, and prevent unplanned outages, even in unconventional storage schemes operating with harsh fluids.

Chapter 2

Fundamentals of Hydraulic Turbines

Hydraulic turbines are fundamental machines in the process of converting hydraulic energy into mechanical and, ultimately, electrical energy. They lie at the core of hydroelectric power plants, where the potential and kinetic energy of water — typically derived from a height differential (head) and a controlled flow rate — is transformed into mechanical rotation, which is then used to drive electric generators. This conversion is accomplished efficiently and with relatively low environmental impact when compared to fossil-fuel-based energy sources.

Hydraulic turbines, or hydraulic motors, utilize the energy of falling or pressurized water in the form of *kinetic energy* — often referred to as *live force* — to perform work. Depending on how this energy is transferred and the structural design of the machine, turbines are subject to a broad classification.

The **runner**, the main rotating element of a hydraulic turbine, is continuously driven by the incoming water. It typically consists of a circular crown enclosed between two annular discs, within which are mounted a series of **curved blades**. These blades receive the working fluid from one side — in a specific direction controlled by the inlet geometry — and discharge it on the opposite side after transferring the kinetic energy to the rotor, to the extent that the turbine is capable of absorbing it.

The delivery of water to the runner is managed by a component known as the **distributor**, which consists of a set of *guide vanes* or channels formed by *stationary diaphragms*, also called *guide blades*. The position and configuration of the distributor relative to the runner is one of the key parameters used to classify different types of turbines. Properly directing the flow is essential not only for efficient blade design and work transfer, but also for determining the flow velocities at the runner, which can be conveniently analyzed using velocity triangles to compute torque, shaft power, and the dynamic forces acting on the rotor. An important aspect that concern turbine analysis and design is the study of velocity triangles, which break down the flow into absolute, relative, and tangential components. These velocity vectors are fundamental in understanding how fluid momentum interacts with the rotating blades to produce mechanical work efficiently [14, 15, 16, 17].

2.1 Velocity Triangles and Work in Turbomachinery

If we consider a hydraulic turbine inserted in a section of a duct between section 1 and section 2, and that it provides the fluid with a work L_i per unit mass that flows through it (the work per unit mass is a specific quantity that indicates the amount of mechanical work produced by the turbine for every kilogram of fluid that passes through it). Under steady one-dimensional flow conditions (a fluid motion in which all the characteristics of the flow, such as velocity, pressure, and flow rate at each single point of the fluid, remain constant over time), the first law of thermodynamics written in Eulerian form and taking into account the second law of thermodynamics allows us to state that:

$$L_i = \frac{p_2 - p_1}{\rho} + \frac{c_2^2 - c_1^2}{2} + g\,(z_2 - z_1) + L_w$$

Where p represents the static pressure (static pressure is the force that a fluid exerts on the walls of the duct that contains it, regardless of its motion); ρ the density of the fluid; c its velocity; z the elevation of the section measured with respect to a vertical z-axis; L_w the work of passive resistances per unit mass flowing in the duct. In the case of turbines, the work is produced by the fluid; therefore, it is possible to highlight the obtained work $(L_i)_{\text{obt}}$ instead of the supplied work L_i, given that:

$$(L_i)_{\text{obt}} = -L_i$$

Consequently:

$$(L_i)_{\text{obt}} = \frac{p_1 - p_2}{\rho} + \frac{c_1^2 - c_2^2}{2} + g\,(z_1 - z_2) + L_w$$

In the previous formula we can notice that, in addition to the term of passive resistances, the following terms appear:

- the **geodetic head** difference $(z_2 - z_1)$;
- the difference in **piezometric heads**, corresponding to the difference $(p_2 - p_1)$ of static pressures;
- the difference in **velocity heads**, corresponding to the difference $\frac{c_2^2}{2} - \frac{c_1^2}{2}$ of kinetic energies.

It is also appropriate to recall that the sum of the geodetic height and the piezometric height is called the geodetic head H; we have:

$$H = z + \frac{p}{\rho g}$$

The sum of the piezometric head and the velocity head is called the total head H_O; thus:

$$H_O = H + \frac{c^2}{2g} = z + \frac{p}{\rho g} + \frac{c^2}{2g}$$

The work can then be reformulated in terms of the total head as follows:

$$L_i = g\,(H_{O2} - H_{O1}) + L_w$$

From this formulation, it follows that in the absence of supplied head and passive resistances, the head remains constant (Bernoulli's theorem).

The mass flow rate $\dot{m}$ in a generic section of a duct is given by the formula:

$$\dot{m} = \rho\, A\, c$$

Since in a liquid the density remains constant, we can state that, in the case of steady one-dimensional flow, as the cross-sectional area of the duct increases the velocity decreases, and vice versa [18].

In turbomachinery **velocity triangles** are a fundamental analytical tool for describing the fluid behavior within the blade channels. They allow for a clear representation and quantification of the velocity relationships that govern momentum exchange between the fluid and the blade. For any turbomachine, it is always possible to draw the velocity triangles at the inlet section (1) and at the outlet section (2) [18, 16, 15, 19].

The three velocities involved are:

- the *absolute velocity* of the fluid $\vec{c}$, measured in a stationary reference frame;
- the *relative velocity* $\vec{w}$, which is the velocity of the fluid relative to the rotating blade;
- the *peripheral velocity* of the blade $\vec{u}$, determined by the angular speed of the rotor and its radial position.

These velocities are related by the fundamental vector equation:

$$\vec{c} = \vec{u} + \vec{w}$$

The absolute velocity $\vec{c}$ can be decomposed into:

- a *meridian (axial or radial) component* c_m, aligned with the primary flow direction,
- a *tangential component* c_u, responsible for angular momentum transfer.

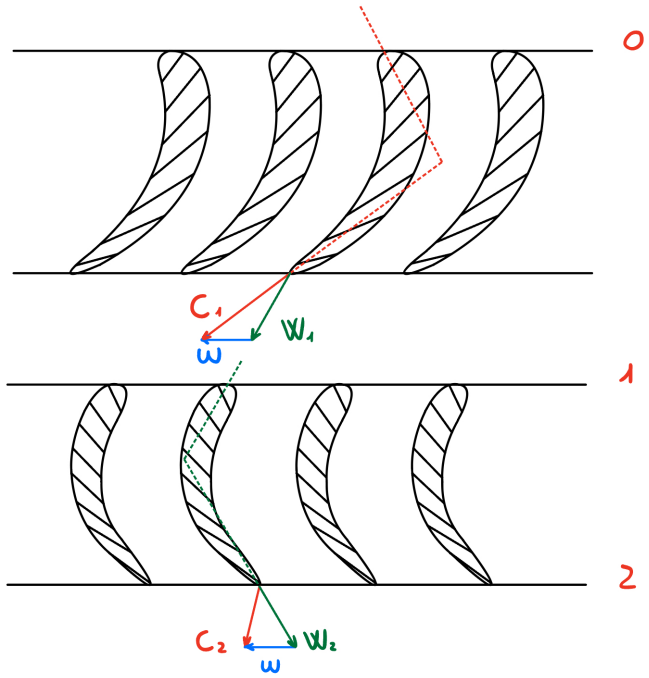

Figure 2.1: Velocity triangle representation: section 0–1 corresponds to the stator, while section 1–2 corresponds to the rotor

The **Euler equation for turbomachinery** is the foundation for computing the *specific work* exchanged between the fluid and the machine:

$$L = u_1 c_{u1} - u_2 c_{u2}$$

where:

- L is the specific work (per unit mass),
- u is the blade peripheral speed,
- c_u is the tangential component of absolute velocity,

This equation can be interpreted differently depending on the type of machine:

- In *power-generating machines* (e.g., turbines), the fluid transfers energy to the rotor. The specific work is:

  $$L = u_1 c_{u1} - u_2 c_{u2}$$

  and $L > 0$, as energy is extracted from the fluid.

- In *power-absorbing machines* (e.g., pumps or compressors), the rotor supplies energy to the fluid. The equation becomes:

  $$L = u_2 c_{u2} - u_1 c_{u1}$$

  with $L > 0$, as energy flows from the machine to the fluid.

With reference to the velocity triangle, by expressing w_1^2 and w_2^2 in terms of u and c through Carnot's theorem, it is possible to obtain a relation that expresses the work supplied as a function of the absolute, relative, and tangential velocities:

$$L_i = \frac{c_2^2 - c_1^2}{2} + \frac{w_1^2 - w_2^2}{2} - \frac{u_1^2 - u_2^2}{2}$$

Or in the form of work obtained:

$$(L_i)_{\mathbf{obt}} = \frac{c_1^2 - c_2^2}{2} + \frac{w_2^2 - w_1^2}{2} - \frac{u_2^2 - u_1^2}{2}$$

In addition to specific work, the **torque** acting on the rotor of a turbomachine can also be derived from the *principle of conservation of angular momentum* (torque = rate of change of angular momentum). Referring to Figure 2.2, the torque T exerted on the runner is given by:

$$T = \rho Q \left(r_1 c_1 \cos\alpha_1 - r_2 c_2 \cos\alpha_2\right)$$

where:

- Q is the volumetric flow rate,
- r_1, r_2 are the radii at the inlet and outlet,
- α_1, α_2 are the angles between the absolute velocity and tangential direction.

This equation expresses the torque as the net angular momentum transferred to the runner, and it can be directly linked to the Euler equation through the relation:

$$P = T \cdot \omega \quad \Rightarrow \quad \frac{P}{\dot{m}} = L$$

where P is the power and ω the angular velocity [18, 15, 20].

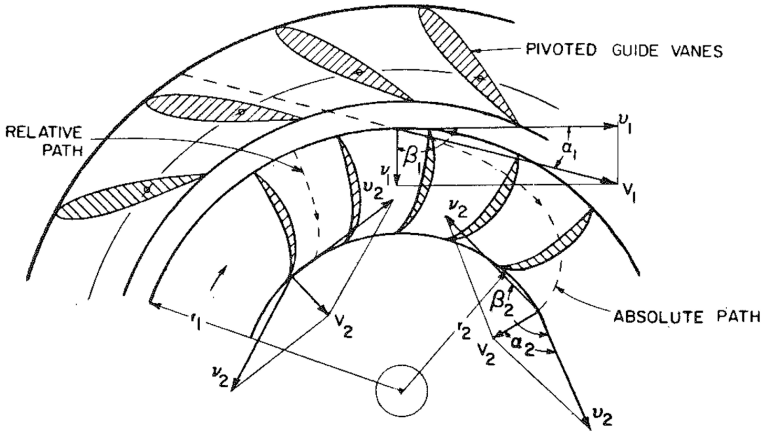

Figure 2.2: Definition sketch for radial flow turbine runner [15]

2.2 Classification of Turbines

Since the key lies in the efficient conversion of the power of water into rotation, the proper selection and operation of the turbine is very important. Turbines in hydroelectric power plants can be classified in several ways. Three major criteria for classification are commonly adopted:

- Classification based upon the direction of flow;
- Classification based upon the pressure of water;
- Classification based upon the shape and orientation of the turbine.

These categories are described in the following sections [20].

2.3 Classification Based Upon Direction of Flow

A more detailed classification considers the **geometry of flow** within the turbine. Water can pass through hydraulic turbines along different flow paths, and depending on the predominant orientation of the water stream relative to the axis of rotation, four main types can be distinguished:

Axial flow turbines

The water flows *approximately parallel to the axis* of the runner. The guide vanes and rotor blades in these machines are generally shaped as *helical surfaces*, generated by a straight line sweeping along the axis of rotation. Kaplan and Propeller turbines are the most representative examples [20].

Radial flow turbines

In these turbines the water moves *perpendicularly to the axis of rotation*, either toward the center (*radial-inflow* or *centripetal*) or away from it (*radial-outflow* or *centrifugal*). The guide and blade surfaces in these configurations are typically *cylindrical*, generated by a line parallel to the axis that follows a curved profile to optimize flow guidance and energy transfer. Pelton turbines belong to this category [20].

Mixed flow turbines

Most hydraulic turbines do not operate with a purely axial or purely radial flow. Instead, the flow exhibits significant components of both directions. These machines are therefore termed *mixed-flow turbines*. The Francis turbine (see Figure 2.3) is the most representative example, with water entering radially and discharging axially [20].

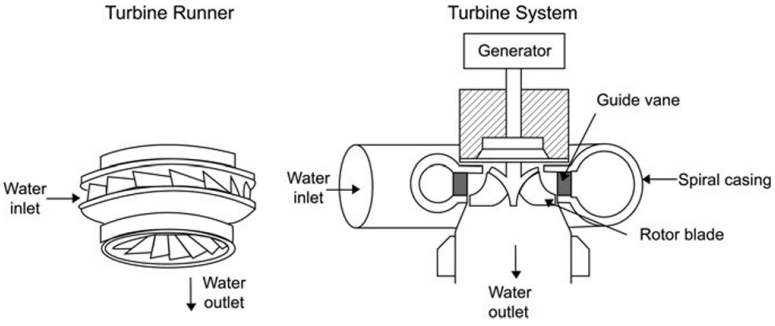

Figure 2.3: Scheme of a Francis turbine [20]

Crossflow turbines

In this configuration, the water jet passes transversely through the blade ring of a cylindrical runner, resembling the blower wheel of an electric air heater. The fluid interacts with the blades twice — once when entering the upper part of the runner and again when exiting through the lower part — thereby transferring energy in two stages. A widely used design is the *Banki* or *Ossberger turbine* (see Figure 8.1), generally employed in the lower power range (below 1 MW). In applications with strongly fluctuating water supply, Ossberger turbines can be built as multi-cell machines, with small and large cells operating in parallel to achieve high efficiency across a wide range of flows [20].

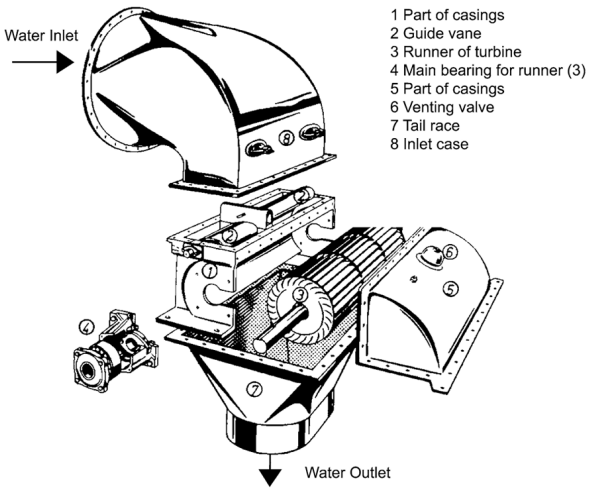

Figure 2.4: Scheme of a Crossflow turbine (Ossberger GmbH) [20]

2.4 Classification Based on Pressure Change of Water

Turbines can be broadly categorized based on the dominant type of energy at the inlet — either *kinetic* or *pressure energy* — as well as on *flow direction* and the available *hydraulic head*. Another fundamental method of classification is based on the change in pressure that occurs as water passes through the rotor: according to this criterion, hydraulic turbines are divided into two main types, **impulse turbines** and **reaction turbines** [20, 17, 16].

- **Impulse turbines**: water reaches the turbine blades with pure kinetic energy and pressure remains constant throughout the runner. The classic example is the *Pelton turbine*.
- **Reaction turbines**: water retains part of its pressure energy and both pressure and velocity contribute to energy conversion. This category includes *Francis* and *Kaplan turbines*.

Table 2.1: Impulse and reaction turbines [9]

Turbine type	**Head classification**		
	High (>50 m)	**Medium (10–50 m)**	**Low (<10 m)**
Impulse	Pelton	Crossflow	Crossflow
	Turgo	Turgo	
	Multi-jet Pelton	Multi-jet Pelton	
Reaction		Low speed Francis	High speed Francis
			Propeller
			Kaplan

2.5 Classification Based Upon Shape and Orientation of Turbines

A further criterion for classification relates to the shape and orientation of the turbine, which depends on constructional features and installation layout. **Bulb turbines** are oriented nearly horizontally, with the generator located inside a bulb-shaped or pear-shaped casing that is partially enveloped by the surrounding water before it flows through the turbine. **Propeller** and **Kaplan turbines** are often designed in this configuration, and an advanced version of the bulb turbine is the **Straflo turbine**, in which the generator poles are mounted on the outer ring of the rotor and the blades are fixed to a supporting ring, effectively transferring motion to the generator. Straflo turbines are generally considered a variation of Propeller turbines. **Vertical turbines**, by contrast, have shafts oriented nearly vertically, with the generator positioned above the water passage. Many Kaplan and Francis turbines adopt this arrangement, although Francis turbines may also be installed horizontally, which often provides advantages in terms of spiral casing design and

water distribution. Another example of turbine design is the Pelton turbine, typically used for high-head, low-flow applications and mounted on vertical shafts. In these machines, only a limited number of buckets interact with the water jet at any given time, meaning the runner is *partially loaded* and individual buckets alternate between periods of loading and rest, illustrating the concept of partial loading that can also occur in other turbine types under specific operating conditions [20].

2.6 Classification based on the performance

The efficiency of a hydraulic turbine strongly depends on the water flow rate and on the specific type of turbine. Pelton and Kaplan turbines generally maintain high efficiency over a wide range of flow conditions, while Propeller and Crossflow turbines exhibit a distinct optimum point. In particular, the maximum efficiency of most turbines (except very small ones) is of the order of 90%, although this maximum is not reached at full load. At very low discharges the efficiency decreases significantly, and a minimum flow rate is required to guarantee turbine operation (e.g., about 30% of the rated flow for Francis turbines). For fixed-blade propeller turbines, efficiency drops rapidly as the discharge decreases. Moreover, the shape of the efficiency curve is influenced by the turbine specific speed [20].

According to the experience of Sulzer Hydro Ltd. (Zurich), the application ranges of various turbine types and pump turbines (PT) are represented in Figure 2.5, plotted on a $\ln Q$ water flow versus $\ln H_E$ head diagram. This diagram reflects the state of the art of hydraulic turbomachinery design, showing the domains where each turbine achieves satisfactory performance. In addition, lines of constant power output are indicated, calculated as

$$P = \eta \, \rho \, g \, Q \, H_E,$$

where an efficiency of $\eta = 0.8$ is assumed throughout the chart [21].

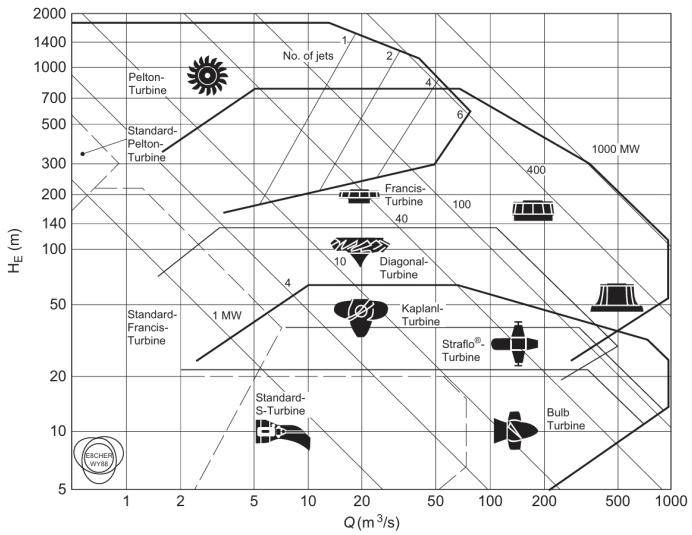

Figure 2.5: Application ranges for various types of hydraulic turbomachines, as a plot of Q versus H with lines of constant power determined assuming $\eta_O = 0.8$ [22]

The selection of a specific turbine type thereby depends on the site's hydraulic conditions — such as head height and flow rate — and on performance considerations like efficiency, cavitation resistance, and structural robustness. As we can see from the Figure 2.5 Pelton turbines is suitable for low flow and high fall height, while, for medium to high fall height and medium to high flow, the Francis turbines is recommended. For low or medium flow and for medium fall height the Kaplan is suitable. It is also notable that there's a region where both Francis and Kaplan could be used, this means that both types of turbines are suitable for such combination of fall height and flow.

2.7 Impulse and Reaction Turbines

Hydraulic turbines are generally categorized into two fundamental types based on the method of energy conversion: impulse turbines and reaction turbines. This distinction applies across both axial and radial flow configurations and is essential to understand the pressure and velocity dynamics at the rotor inlet. The degree of reaction is a useful parameter for characterizing a turbine, as it defines the proportion of the total enthalpy drop that occurs in the rotor compared to the stator.

$$\chi = \frac{-\Delta h_{\text{rotor}}}{-\Delta h_{\text{stator}} - \Delta h_{\text{rotor}}}$$

The degree of reaction can also be expressed in terms of work. If we consider the degree of reaction as the ratio between the variation $\Delta H'$ of the piezometric head in the runner and in the diffuser, and the variation ΔH of the piezometric head throughout the turbine, we can express χ as:

$$\chi = \frac{\Delta H'}{\Delta H}$$

Applying the first principle of thermodynamics we can express $\Delta H'$ and ΔH as:

$$\Delta H = (L_i)_{\mathbf{obt}}$$

$$\Delta H' = (L_i)_{\mathbf{obt}} - \frac{c_1^2}{2}$$

We can also express χ as:

$$\chi = \frac{(L_i)_{\mathbf{obt}} - \frac{c_1^2}{2}}{(L_i)_{\mathbf{obt}}}$$

If $\chi = 0$, the turbine is of the impulse type; therefore $\Delta h_{\text{rotor}} = 0$ and $p_1 = p_2$.

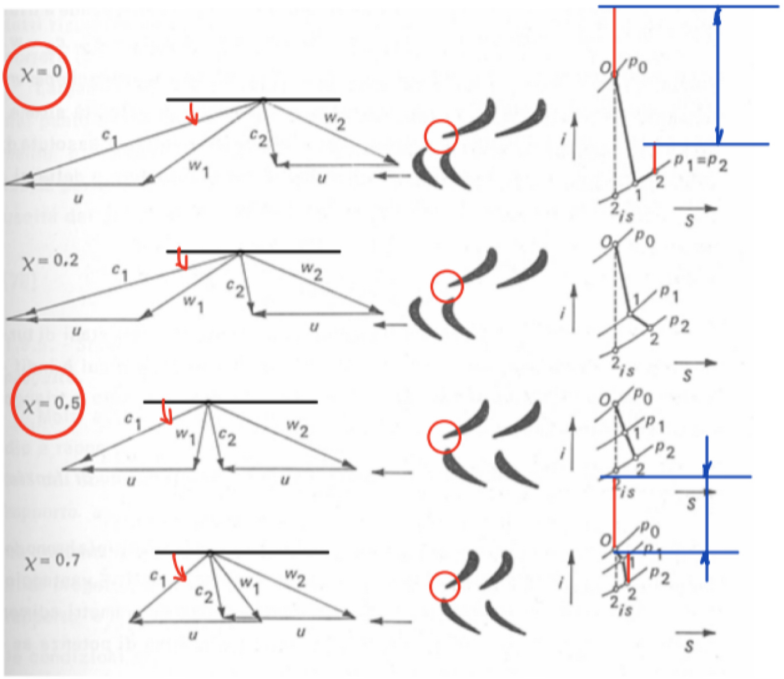

Figure 2.6: Velocity triangles for different degree of reaction

Impulse Turbines

In an impulse turbine, the entire available head is converted into kinetic energy before the fluid reaches the runner. This occurs via nozzles, which accelerate the flow to high velocity, and the fluid impacts the runner blades while operating at atmospheric pressure. Energy transfer is purely through momentum exchange.

Pelton turbines, designed for high-head, low-flow applications, consist of runners with multiple buckets. A high-velocity jet strikes the buckets and is deflected, causing torque on the shaft. Since no draft tube is used, all available head must be converted in the nozzle. Any residual kinetic energy in the outflow is considered inefficient, thus bucket design aims to minimize exit velocity.

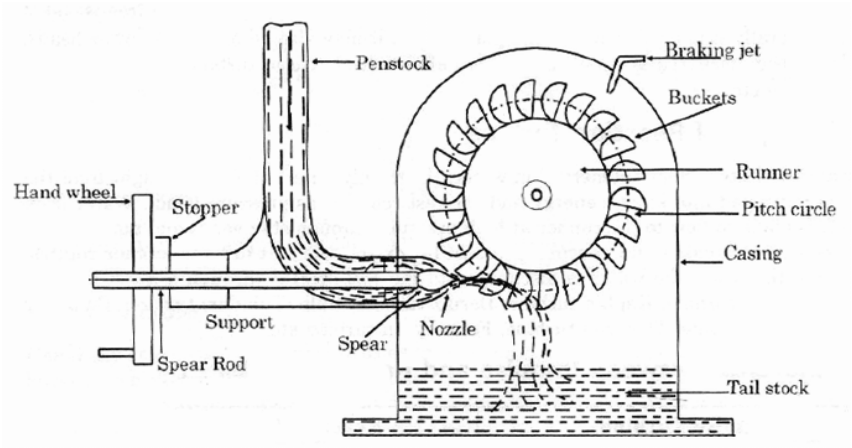

Figure 2.7: Schematic of an impulse (Pelton) turbine [23]

The specific speed of Pelton turbines increases proportionally to the square root of the number of nozzles; it can also be enhanced by jet arrangement, as in Turgo turbines, where the jet passes through the runner obliquely, engaging multiple buckets. Typically, impulse turbines feature a high deflection angle and operate with low flow rates [15, 16, 17, 20].

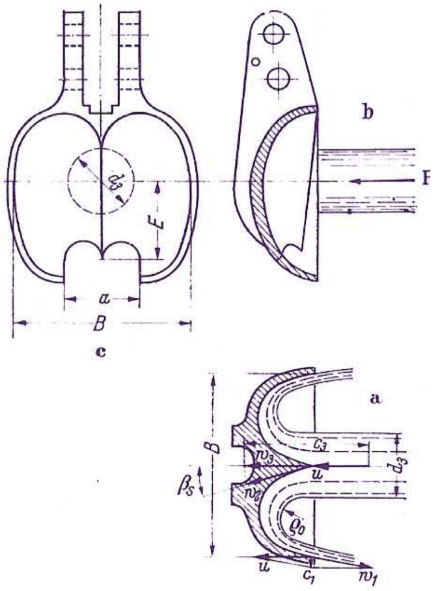

Figure 2.8: Blade of a Pelton turbine.

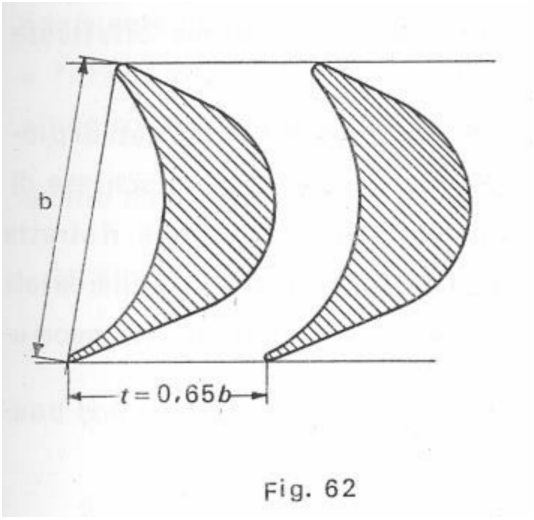

Figure 2.9: High deflection Impulse turbine rotor.

Reaction Turbines

In contrast, reaction turbines have their runners fully submerged, and pressure and velocity both vary across the rotor. Only part of the head is converted into velocity at the inlet, with the remainder present as pressure. As the water flows through the rotating blades, additional kinetic energy is generated via pressure drop [16, 17, 20].

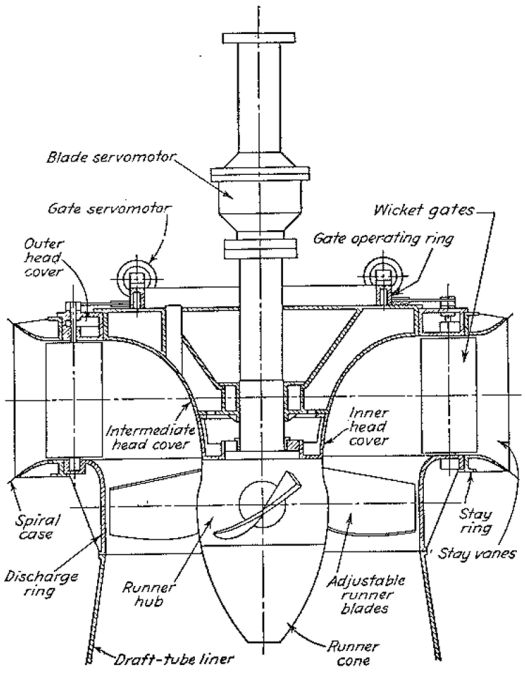

Figure 2.10: Schematic of a reaction (Kaplan) turbine [15]

Typically, the inlet velocity head is less than 50% of the total. Reaction turbines require casings and a draft tube to recover kinetic energy and allow the runner to sit below tailwater. Flow configurations include:

- **Radial flow**: water flows perpendicular to the axis,
- **Mixed flow**: combination of radial and axial components,
- **Axial flow**: flow aligned with the shaft.

The **Francis turbine** is a common radial/mixed flow design, with axial flow increasing with higher specific speeds.

Both turbine types operate under the same mechanical principle captured by the **Euler turbine equation**, expressing torque as the net angular momentum change:

$$T = \dot{m} \cdot (r_1 c_{u1} - r_2 c_{u2})$$

where:

- T = torque on the shaft,
- $\dot{m}$ = mass flow rate,
- c_{u1}, c_{u2} = tangential components of absolute velocity at inlet and outlet,
- r_1, r_2 = respective radii.

This formulation shows how impulse relies on momentum exchange at the nozzle, while reaction adds pressure-driven acceleration within the runner, yet both ultimately depend on angular momentum change.

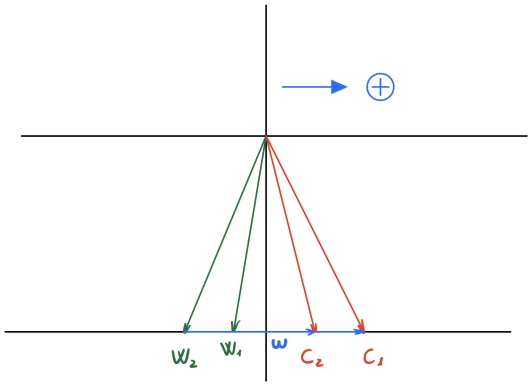

(a) Velocity triangle of a reaction turbine

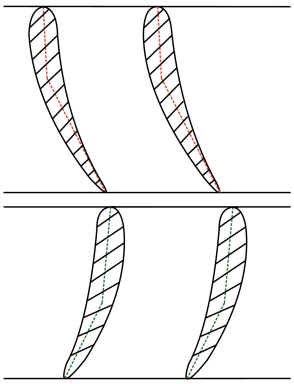

(b) Blade deflection angle in rotor and stator of a reaction turbine

Figure 2.11: Schematics related to the design of the reaction turbine.

Chapter 3

Francis Turbine

3.1 History

The **Francis turbine** was developed in the mid-19th century by the Scottish-American engineer *James B. Francis* (1815–1892). At that time, the challenge in hydraulic engineering was to design machines capable of efficiently converting medium-head water energy into mechanical energy. Earlier water wheels and primitive turbines were limited either to low-head or high-head applications, leaving a gap in the medium range. Francis innovated by creating a mixed-flow reaction turbine, where water enters radially and exits axially. This concept significantly increased efficiency, and over time the Francis turbine became the most widely used hydraulic turbine in the world, forming the backbone of modern hydropower [20, 19].

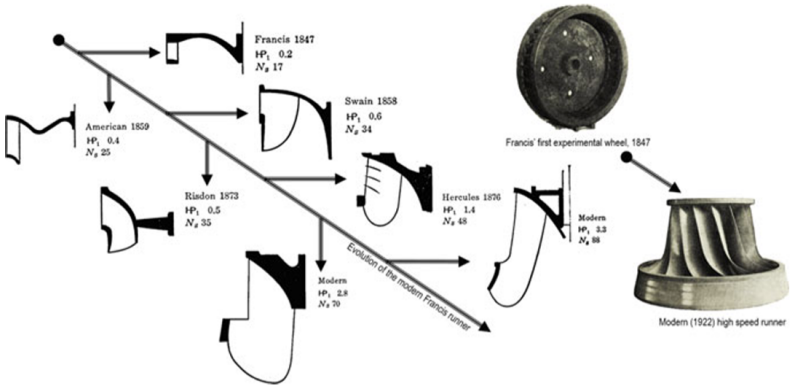

Figure 3.1: Evolution of the modern Francis runner blades [19]

3.2 Main Components

A 3D model of a Francis turbine is shown in Figure 3.2. The hydraulic design mainly concerns the **spiral casing**, **stay vanes**, **guide vanes**, **runner**, **draft tube**, and **labyrinth seals**. Other components such as the **shaft**, **bearings**, **head covers**, and **gate operating ring** relate mostly to the mechanical design. In this section, we will focus primarily on the hydraulic components, although some basic mechanical

considerations will be discussed.

The key components and their roles are summarized below:

- **Spiral Casing:** The spiral casing transfers water from upstream into the runner through the stay vanes and guide vanes. Its cross-sectional area decreases uniformly along the circumference, ensuring that the velocity of the water remains nearly constant as it passes through the stay vanes. Since water enters the runner blades from the very beginning of the casing, the discharge gradually decreases along the spiral path. By reducing the cross-sectional area accordingly, the casing maintains uniform pressure and guarantees that the momentum, and therefore the velocity, of the water striking the runner blades is evenly distributed [19, 14].

- **Stay Vanes:** The stay vanes guide the water towards the runner blades while remaining stationary in their position. Their main purpose, unlike guide vanes, is not to provide a hydraulic impact but to add mechanical strength to the turbine. They provide structural support to the spiral casing, preventing it from tearing apart, and are designed to minimally disturb the flow. To achieve this, stay vanes are shaped according to the free vortex theory, meaning that the flow is guided into the guide vanes along the same path that would be made if the vanes were not present. By reducing the swirling of water caused by radial flow, they increase the efficiency of the turbine. However, due to their geometry, they introduce a slight increment in the tangential component of absolute velocity c_u, in accordance with free vortex theory [19, 14].

- **Guide Vanes:** After passing through the stay vanes, water glides through the guide vanes before entering the runner blades. The guide vanes can rotate and adjust their angle, thereby regulating both the flow rate of water and the angle of attack at which water strikes the runner blades. This capability allows the turbine to adapt to varying operating conditions and control its power output according to the load demand. The guide vane opening corresponding to the designed discharge is called the best efficiency point (BEP), at which the turbine achieves its maximum efficiency [19, 14].

- **Runner:** Considered the heart of the turbine, it converts hydraulic energy into mechanical energy. It is the only rotating hydraulic component and is directly connected to the shaft, meaning that relative velocity concepts are valid only inside the runner. The design of the runner blades strongly influences turbine performance: in a mixed-flow Francis turbine, the upper part of the blades exploits the reaction force of the water passing through, while the lower part is shaped like a small bucket, utilizing the impulse action. The combination of reaction and impulse effects produces the torque that drives the rotation of the runner [19, 14].

- **Labyrinth Seals:** Minimize leakage losses between the runner and the cover

and help balance axial forces. They consist of a static part connected to the covers and a rotating part connected to the runner [19, 14].

- **Draft Tube:** Connects the runner outlet to the tailrace. Its main function is to convert the remaining kinetic energy of the water leaving the runner into pressure energy, thereby improving the overall efficiency of the turbine. To achieve this, the draft tube has an expanding cross-sectional area along its length: as water exits the runner at relatively low pressure, the gradual enlargement of the draft tube allows recovery of pressure while directing the flow smoothly towards the tailrace [19, 14].

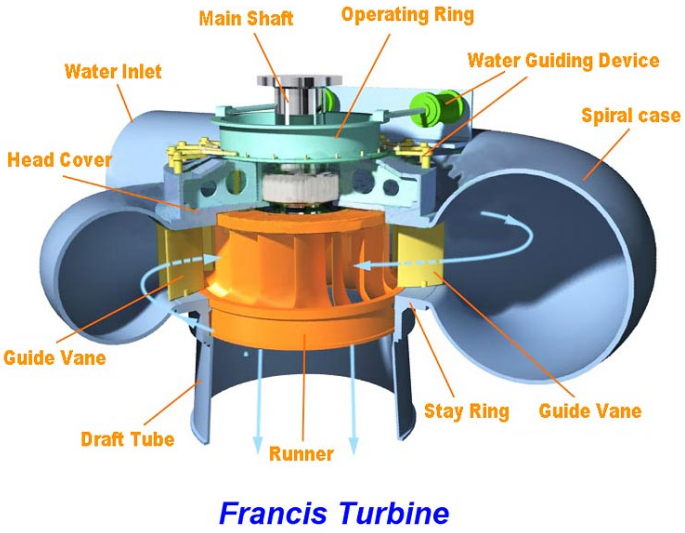

Figure 3.2: Francis turbine main components [14]

Water enters through the **spiral casing** and passes the **stay vanes**, which provide structural support while minimally disturbing the flow. The **guide vanes** then regulate the flow into the **runner**, which rotates and transmits mechanical power through the **shaft**. **Labyrinth seals** minimize leakage and balance axial forces, while the **draft tube** recovers kinetic energy and reduces exit velocity. This configuration allows the Francis turbine to operate efficiently over a wide range of flows while ensuring mechanical stability and long-term reliability.

The theoretical explanation of energy transfer, as we mentioned in the previous chapter, is based on velocity triangles. At the inlet, water reaches the runner with absolute velocity vector $\vec{c}_1$, containing a tangential component c_{u1} in the direction of rotation. The runner rotates at peripheral velocity u, and from the runner's frame the relative velocity is $\vec{w}_1$. At the outlet, water leaves with velocity vector $\vec{c}_2$ and tangential component c_{u2}, while the runner has peripheral velocity u. The torque T exerted on the runner arises from the change in angular momentum of the fluid and is expressed as

$$T = \dot{m}\,(r_1 c_{u1} - r_2 c_{u2})$$

where r_1, r_2 are the radii at outlet and inlet. The mechanical power P delivered by

the turbine is then

$$P = T \cdot \omega = \dot{m} \left(u_1 c_{u1} - u_2 c_{u2} \right)$$

with ω the angular velocity of the runner. The best efficiency point is reached when the relative velocity vectors $\vec{w}_1$ and $\vec{w}_2$ are parallel to the runner blades, minimizing losses.

To increase the rotational speed of a turbine, according to certain relationships, it is necessary to increase both the angle α_1 and the angle β_1. While the outlet velocity triangle remains right-angled with an axial component c_2, the inlet velocity triangle changes as the rotational speed increases. Three characteristic situations are shown in the Figure 3.3, which are representative of a slow Francis turbine, a standard Francis turbine, and a fast Francis turbine.

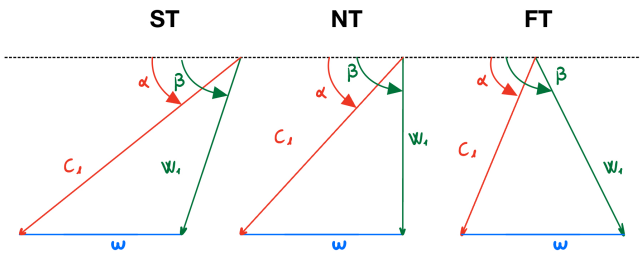

Figure 3.3: Different velocity triangles for diverse rotational speeds (slow, normal, fast)

It can also be stated, as an indicative reference, that the degree of reaction χ is around 0.3 for a slow turbine, around 0.4 for a normal turbine, and around 0.5 for a fast turbine.

Table 3.1: Characteristic angles, degree of reaction, and u_1/c_1 ratio for Francis turbines [18]

Turbine type	$\boldsymbol{\alpha_1}$ (deg)	$\boldsymbol{\beta_1}$ (deg)	χ	$\boldsymbol{u_1/c_1}$
Slow turbine	15–20	60–70	0.3	$< \cos\alpha_1$
Normal turbine	25–30	90	0.4	$\approx \cos\alpha_1$
Fast turbine	35–40	120–130	0.5	$> \cos\alpha_1$

An important design parameter is the **specific speed** n_s, a dimensionless number used to classify turbines according to geometry and operating conditions. In metric units, the relation between the actual rotational speed n and the specific speed n_s is given by

$$n = n_s \cdot H^{3/4} \cdot Q^{1/2}$$

Higher specific speed corresponds to lower rotational speed and larger runner height, allowing the turbine to handle large discharges at low exit velocity, thus avoiding cavitation [20].

We can also find another formulation of the specific speed Ω_{sp} used to compare different turbines:

$$\Omega_{sp} = \frac{\omega \sqrt{P/\rho}}{(gH_E)^{5/4}}$$

where P is the power delivered to the shaft, H_E is the effective head at turbine entry, and ω is the rotational speed in radians per second [21, 15].

It is possible to characterize each class of geometrically similar turbines based on the characteristic specific speed, n_c, defined such that it corresponds to the operating point of maximum efficiency. Once the specific speed at design conditions is determined, it provides a clear guideline for selecting the appropriate turbine type to achieve high efficiency.

The specific speed of a turbine is a dimensionless parameter that encapsulates the performance characteristics of a family of similar machines under unit head and unit power conditions. In particular, it enables designers to identify the runner geometry that typically achieves the best efficiency.

As a practical example, consider a turbine (or pump-turbine) delivering one horsepower (standard mechanical unit) under a net head of one meter. The corresponding characteristic specific speed, n_c, can be expressed as:

$$n_c = \frac{n\sqrt{P_u}}{H_u^{5/4}}$$

where n is the rotational speed in rpm, P_u is the power in horsepower, and H is the hydraulic head in meters. In this simplified scenario, with $P_u = 1$ and $H = 1$, the equation reduces to:

$$n_c = n \cdot \frac{\sqrt{1}}{1^{5/4}} = n.$$

Therefore, under these normalized conditions, the rotor speed n directly equals the characteristic specific speed n_c. Knowing n_c at the design point allows selection of a turbine whose geometric characteristics (such as blade angles, runner diameter, and flow passage shape) are best suited to those specific operating conditions, ultimately ensuring peak hydraulic efficiency.

Table 3.2: Characteristic specific speed ranges for different turbine types [18]

Turbine Type	$\boldsymbol{n_c^*}$ [rpm]
Pelton	5–60
Francis (slow)	60–100
Francis (normal)	100–200
Francis (fast)	200–450
Kaplan	450–1000

The characteristic rotational speed, n_c, has a significant influence on the profile of the runner blades. Denoting by D_1 the runner diameter at the inlet section, by B the axial height of the distributor, and by D_s the diameter of the circular outlet

section, the following observations can be made:

- For low values of n_c, since the ratio B/D_1 is small, the outlet diameter must satisfy $D_s < D_1$.
- For high values of n_c, as $B/D_1 \approx 0.5$, the outlet diameter D_s must be equal to or greater than D_1.

The figure illustrates the different runner profiles according to the turbine type, highlighting how the geometry varies with the characteristic rotational speed[18].

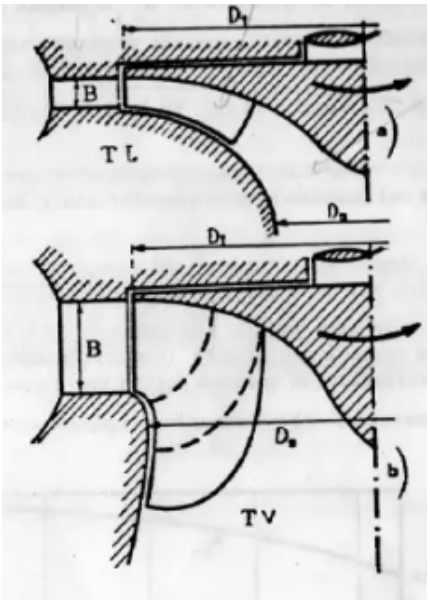

Figure 3.4: Blades profiles for different n_c [18]

3.3 Efficiency

For the calculation of efficiency, we consider a hydraulic turbine installed in a system that uses an upper reservoir from which water flows, passing through the turbine before reaching a lower reservoir. Let point 1 denote the free surface of the upper reservoir and point 2 the free surface of the lower reservoir.

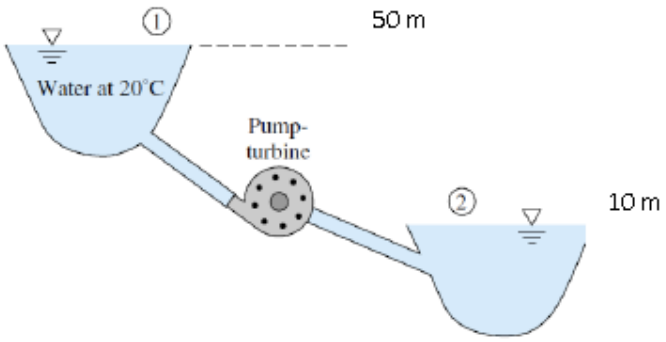

Figure 3.5: Schematic of the hydraulic system [24]

The available head H_D is defined as the difference between the total heads corresponding to the free surfaces of the two reservoirs, that is:

$$H_D = H_1^O - H_2^O = (z_1 - z_2) + \frac{p_1 - p_2}{\gamma} + \frac{c_1^2 - c_2^2}{2g}$$

Where γ is the *specific weight* of the fluid, defined as $\gamma = \rho g$.

If we consider that the tanks communicate with the external environment and therefore the difference between the static pressures is negligible, and the kinetic terms are neglected, we will have that:

$$H_D = z_1 - z_2$$

That is, the available head is reduced to only the geodetic (or elevation) level.

Not all of the available head can be used in the turbine, due to head losses in the penstock or in the connection between the reservoir and the turbine, when there is no penstock. The net or useful head H_U is defined as the difference between the available head H_D and the head losses Y occurring in the penstock and connections.

$$H = H_D - Y$$

The *efficiency of the penstock* η_C is defined as the ratio between the useful head and the available head.

$$\eta_C = \frac{H}{H_D} = \frac{H_D - Y}{H_D}$$

Not all of the useful head is converted into work, due to passive resistances encountered by the fluid while passing through the turbine and possible losses of kinetic energy that are not recovered at the discharge. If such losses correspond to a head H_W, then:

$$L = g\,(H - H_W)$$

The *hydraulic efficiency*, η_y, of the turbine is defined as the ratio:

$$\eta_y = \frac{H - H_W}{H}$$

Reminding that L_w is the work corresponding to the losses encountered by the fluid during its passage through the turbine, and recall that H_w represents the total head variation between the upstream and downstream of the turbine, we can express the work obtained as:

$$(L_i)_{\mathbf{obt}} + L_w = g\,H$$

So the hydraulic efficiency can be also written as:

$$\eta_y = \frac{(L_i)_{\mathbf{obt}}}{(L_i)_{\mathbf{obt}} + L_w}$$

Moreover, not all the flow rate $\dot{m}$ that passes from the reservoir to the turbine can be processed and converted into work: a fraction $\Delta\dot{m}$ leaks through clearances of the penstock and does not act on the blades, thus not contributing to power production.

The *volumetric efficiency* η_v is therefore defined as the ratio:

$$\eta_v = \frac{\dot{m} - \Delta\dot{m}}{\dot{m}}$$

The *internal power* is given by:

$$P_i = (\dot{m} - \Delta\dot{m})(L_i)_{\text{obt}} = \eta_v\,\dot{m}\,(L_i)_{\text{obt}} = \eta_v\,\eta_y\,\dot{m}\,g\,H$$

Not all the internal power can be utilized because part of it is lost due to friction and for driving the auxiliaries. The *mechanical efficiency* η_m is defined as the ratio between the useful power and the internal power:

$$\eta_m = \frac{P_u}{P_i}$$

The useful work obtained, i.e. the ratio between the useful power and the flow rate $\dot{m}$ passing through the turbine, is expressed as:

$$(L_u)_{\text{obt}} = \frac{P_u}{\dot{m}} = \frac{P_i}{\dot{m}}\,\eta_m = \eta_m\,\eta_v\,(L_i)_{\text{obt}} = \eta_m\,\eta_v\,\eta_y\,g\,H$$

The ratio between the useful work obtained and the available head is called the *total efficiency* η_t of the turbine; it is:

$$\eta_t = \eta_m\,\eta_y\,\eta_v$$

We can also define the *Global efficiency* η_g of the plant that is defined as the ratio between the useful work obtained and the available head:

$$\eta_g = \eta_C \cdot \eta_t = \eta_m\,\eta_v\,\eta_y\,\eta_C$$

Consequently, the useful power can be expressed by the following relation:

$$P_u = \dot{m}\,(L_u)_{\text{obt}} = \eta_t\,\dot{m}\,g\,H = \eta_g\,\dot{m}\,g\,H_D = \eta_g\,\dot{m}\,g\,(z_1 - z_2)$$

Typically, the overall efficiency of a hydroelectric plant ranges between 0.80 and 0.90. Most of the losses are of hydraulic nature, since the volumetric and mechanical efficiencies are on the order of 0.98–0.99 [25, 18].

The characteristic quantities that describe the behavior of a turbine are: power, mass flow rate $\dot{m}$ or volumetric flow rate Q, rotational speed, and global efficiency [25]. Since hydraulic turbines are used at constant rotational speed and available head, the first diagram of interest is that of the *part-load curves* Figure 3.6, which show the variation of useful power and global efficiency as a function of the flow passing through the machine. This variation is achieved by adjusting the wicket gate opening while maintaining the design values of rotational speed and available head. The term "available head" is used because the losses in the penstock belong to the plant and not to the turbine itself.

From the diagram, it can be observed that useful power and efficiency drop to zero before the flow reaches zero, due to mechanical losses and auxiliary components, which under such conditions absorb all the internally generated power. Moreover, by the manufacturer's design choice, the overall efficiency at a flow rate of approximately 80% of the maximum is very close to the maximum value. Therefore, under design conditions, the efficiency is slightly lower than the maximum available; however, as the load decreases, the turbine maintains a wide regulation range, with an overall efficiency that remains sufficiently high.

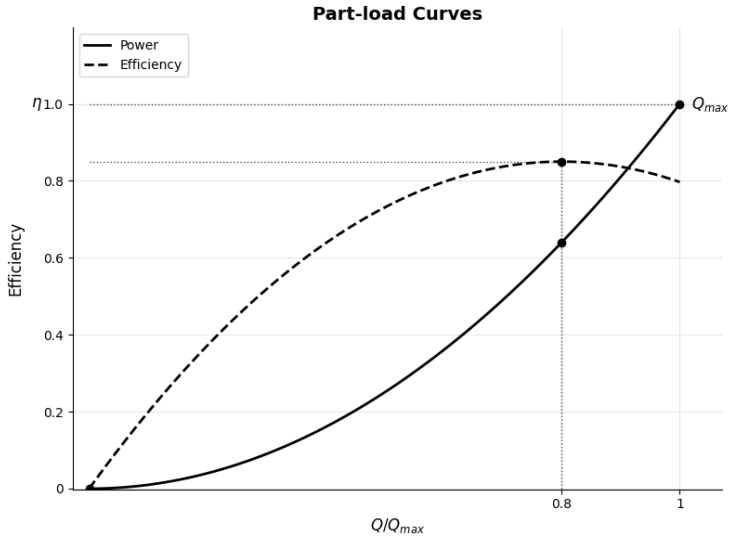

Figure 3.6: Part-load curve

If, instead, we want to determine the behavior of a turbine as the rotational speed varies, it is necessary to refer to a set of diagrams, each corresponding to a different value of the distributor opening A_P. For example, it is necessary to know the η_t diagrams for different distributor openings A_P.

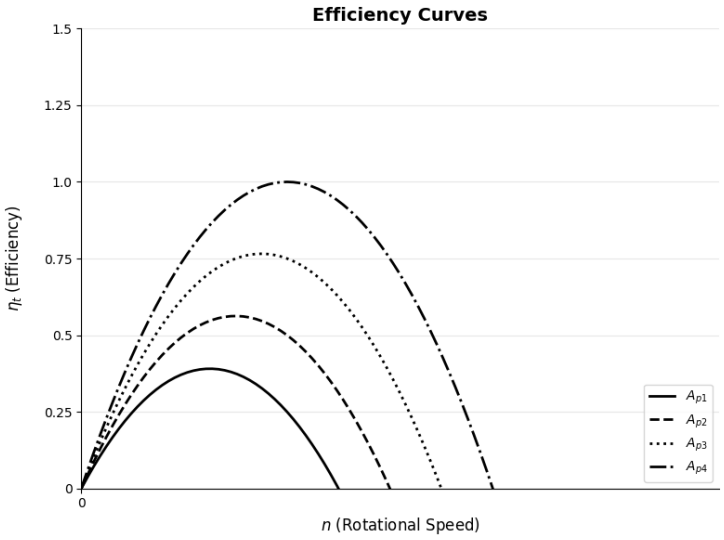

Figure 3.7: Efficiency curves for different guide vane openings $A_\mathbf{p}$

In the Figure 3.8 we can see the different design point efficiency for different kind of turbines. It is remarkable that the efficiency of the multistage Pelton turbine has now reached 92.5% at $\Omega_{sp} \approx 0.2$, and that the Francis turbine can achieve an efficiency of 95%–96% at $\Omega_{sp} \approx 1.0$–2.0 [21].

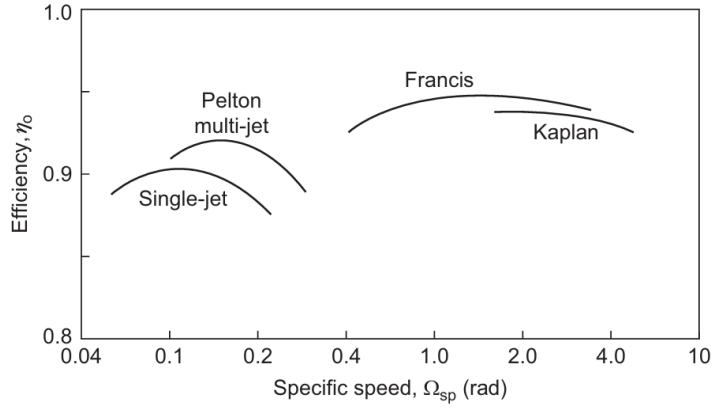

Figure 3.8: Typical design point efficiencies of Pelton, Francis and Kaplan turbines [21]

3.4 Reversible Bladed Hydraulic Machinery in Pumped Storage Systems

The concept of reversibility in bladed hydraulic machinery is fundamental to pumped-storage applications. A Francis turbine, when rotated in the opposite direction, can operate as a pump. This dual functionality enables the same machine to both generate electricity during peak demand and pump water back to the upper reservoir during off-peak periods, thereby stabilizing the grid [25, 6, 26].

For a hydro turbine runner driven to rotate in reverse (the rotational speed

remains unchanged), the magnitude of u is the same, but the direction is opposite. As we can see in Fig 3.9, the blade shape provides the fluid with the same relative velocity w in the opposite direction, and the resultant absolute velocity c also has the same magnitude but reversed direction. The components c_u and c_m follow the same behavior. In this case, the fluid obtains energy H and flows to the upstream reservoir, switching the machine to **pump mode**.

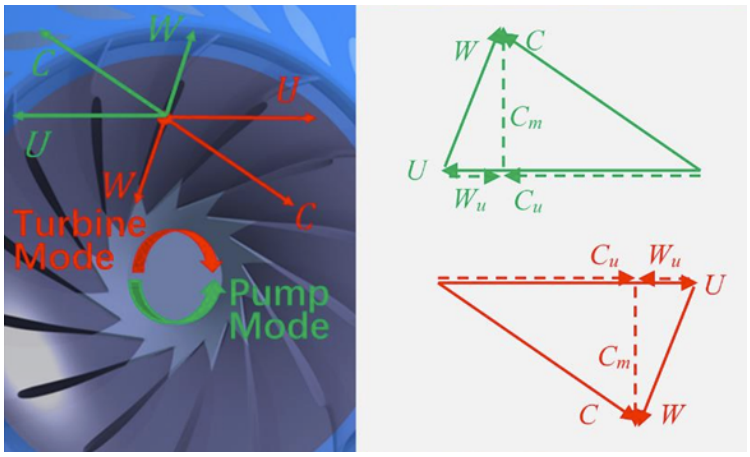

Figure 3.9: Velocity triangles of the blade's runner in the turbine mode and pump mode [6]

Under non-ideal conditions, losses occur, and the runner efficiency in turbine mode η_t and pump mode η_p can be calculated as:

$$\eta_t = \frac{T\omega}{\rho QgH}, \quad \eta_p = \frac{\rho QgH}{T\omega}$$

The reversibility of bladed hydraulic machinery provides an effective solution for pumped storage applications. A single design can operate in both modes, with reverse runner rotation enabling the conversion between turbine and pump operation, thus responding to the power grid's demands. Economically, pumped storage units are generally designed for heads up to 800 m, with the runner usually of the Francis type [25]. For tidal energy, the rising and ebbing tides can be dammed to allow forward and reverse pumping as well as power generation. Low-head, full-condition pumped storage hydro units can also utilize **tubular turbines** or **axial-flow pumps**, achieving efficient two-way operation [26] [6].

Chapter 4

Main Phenomena Affecting Turbine Performance

Hydraulic turbines are designed to ensure high efficiency, robust operation, and long service life. Efficiency and power output are strongly influenced by blade profiles, flow angles, multi-stage runners, and variable-speed operation.

Despite careful design, several phenomena can impair performance, reduce energy conversion efficiency, and increase maintenance requirements. These phenomena can be grouped into four main categories: **hydraulic, mechanical, structural, and operational**.

In recent years, high-head Francis turbines and PT units have been increasingly exposed to a high number of operational transients due to the growing integration of non-dispatchable renewable energy sources into the electrical grid. It has been reported that a Francis turbine can experience more than 3000 transients per year. Startups, emergency shutdowns, load acceptance, and load rejection generate rapid and intense variations in pressure and torque, leading to cyclic stresses and fatigue phenomena [27].

Experimental investigations have shown that pressure and torque fluctuations are particularly high during startup, due to the large inertia of the water mass and the uncontrolled motion of the guide vanes. The inertia of rotating components also plays a critical role in dynamic behavior: older massive runners provided better stability but required long synchronization times (time interval required for the turbine to reach the synchronous speed of the grid). To reduce startup times, lighter runners have been introduced, although at the expense of dynamic stability, making them more prone to vibrations, oscillations, and asymmetric loads. Flow control strategies and the adoption of advanced materials or coatings have mitigated these issues, though not eliminated them [27].

Guide vanes, **stay vanes** and **rotor blades** are subject to similar structural and hydraulic issues, though in different ways. Guide vanes, responsible for flow regulation, are particularly stressed during rapid regime changes and sudden load variations. The stay vanes, although fixed, experience vibrations and hydraulic pulsations that can cause crack initiation at their connections to the stator ring.

Rotor blades are exposed to pressure fluctuations, cavitation, flow-induced vibrations, and cyclic stresses that may cause fatigue, surface erosion, or micro-crack formation, particularly during startup, shutdown, and load rejection events [27, 28].

In general, the loading mechanisms acting on the blade systems, fixed, movable or rotor, can be classified into **static loads** and **dynamic loads**, with the latter further subdivided into fatigue types of high cycle and low cycle.

4.1 Main Phenomena

Hydraulic Losses and Flow-Induced Phenomena

These include losses due to blade surface friction (along-track), localized flow separation, jet impingement, and vortex-induced recirculation. Mitigation strategies involve optimizing flow passages, using drag-reducing materials, adjusting operational parameters, and ensuring regular maintenance. Advanced methods combine entropy production analysis with differential kinetic energy balances to evaluate hydraulic losses from a thermodynamic perspective [25].

Rotor–Stator and Rotor–Rotor Interaction

These interactions occur between guide vanes and runner blades under steady operation, or between multiple rotating components during transient phases. If excitation frequencies coincide with structural natural frequencies, resonance may occur, reducing hydraulic efficiency, increasing vibration, and accelerating fatigue damage (see Figure 4.1 and Figure 4.2) [28].

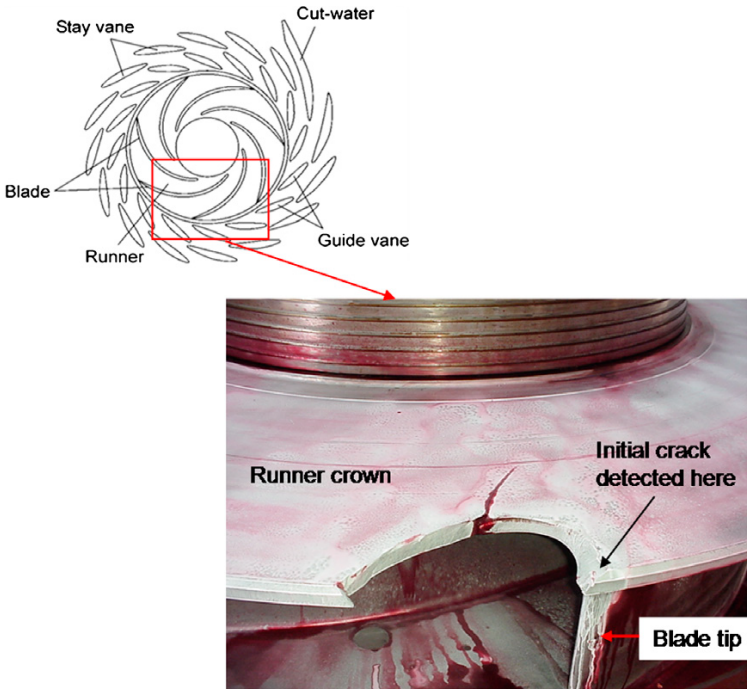

Figure 4.1: Picture of the broken runner [29]

Figure 4.2: Fatigue damage on the runner with the bench marks [29]

Flow-Induced Oscillations and Vibrations

Inevitable during turbine operation, oscillations degrade both mechanical and overall energy efficiency. Modern research couples computational fluid dynamics with structural mechanics and experimental measurements to analyze fluid–structure interactions [25].

Flow-Induced Noise

Noise is generated mainly by turbulence, vortex evolution, and pressure fluctuations. Influencing factors include flow velocity, channel geometry, and fluid characteristics. Noise modeling remains challenging, but acoustic coupling methods and structural optimization are commonly used mitigation strategies [25].

4.2 Loads Types

Turbine components are subjected to several types of loads that may trigger failure mechanisms such as cavitation, vortex shedding, or resonance.

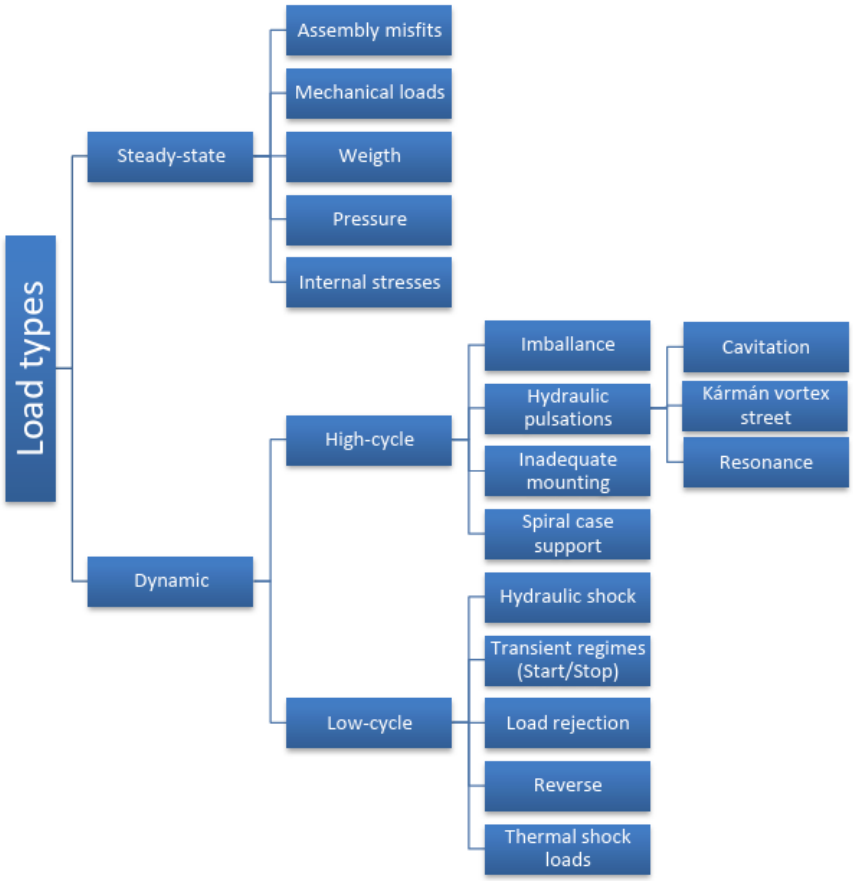

Figure 4.3: Load Types [28]

Loads can be classified into the following categories:

Steady-State Loads

Steady-state loads are those static or quasi-static loads that can cause stresses exceeding the material's elastic limit. They may arise from constructional inaccuracies, operational anomalies, or technological factors. The main steady-state loads include:

- Exceeding the elastic limit of the material.
- Assembly misfits and residual stresses due to misalignment of static guides relative to other structural components.
- Mechanical overloads from debris or atypical operating conditions.
- Unforeseen redistribution of mass or unbalanced pressures, for example in the stator columns.

- Internal stresses resulting from welding or other technological processes.

This kind loads are usually detected during test of the equipment that is carried out after first assembly or after rehabilitation. Each of these potential sources of failures could be recognized and eliminated [28].

High-Cycle Dynamic Loads

High-cycle dynamic loads are those that induce material fatigue over a large number of cycles. They typically arise from operational or structural factors and can lead to crack initiation. They can be classified into:

- **Mass imbalance:** inaccuracies in the distribution of the turbine unit's masses can cause periodic oscillations, leading to fatigue.
- **Hydraulic pulsations:** rapid pressure changes (typically in less than a few seconds) caused by hydrodynamic processes, such as cavitation, standing waves, or sudden opening/closing of movable guide vanes. These include:
  - Pulsations in the turbine wheel rotation due to cavitation.
  - Pressure ripples and resonance phenomena.
  - Kármán vortex shedding, which can interact with the natural frequencies of the structure.

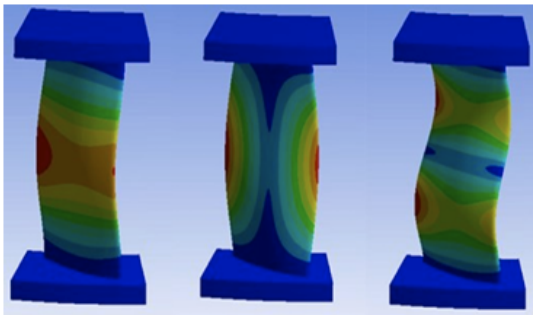

Figure 4.4: Hydraulic pulsation types on a stay vane [28]

- **Improper installation or manufacturing defects:** deviations in the nominal geometry or alignment of components can generate both static and dynamic loads.
- **Spiral case support degradation:** violations in the connection between the spiral case and the concrete casing can cause "breathing" of the metal structure, increasing cyclic stresses.

High-cycle dynamic loads are a potential treat for stay vanes crack initiation. Special attention should be paid on: hydraulic pulsation and spiral case support and its rigidity [28].

Low-Cycle Dynamic Loads

Low-cycle dynamic loads are characterized by relatively large amplitudes and can lead to rapid fatigue failure, particularly under significant overloading. They typically arise from transient operational events and can induce irreversible material deformation. Key sources include:

- **Hydraulic shock:** sudden increases or decreases in flow speed, or abrupt changes in flow direction, causing peak pressure rises due to the conversion of kinetic energy into potential pressure energy.
- **Hydraulic pulsations:** rapid variations in working pressure caused by hydrodynamic processes, particularly during startup, shutdown, or sudden load changes.
- **Load rejection:** abrupt changes in the system's operating mode caused by unplanned disturbances, such as power supply failures in pump mode or sudden load drops in generator mode.
- **Flow reversal:** rapid changes in load or operating mode, including operation in air during pump startup, causing significant variations in structural loads.
- **Thermal shocks:** sudden temperature changes leading to structural loads from differential thermal deformations of components.

Low-cycle dynamic loads are interesting with their amplitudes rather than their frequency. Usually, the fatigue failure mechanism of pressure equipment in PHES is considered to be a combination of low-cycle fatigue from dynamic operational loads and high-cycle fatigue due to hydraulic load fluctuations [28, 25].

It is also remarkable the study in which runner and distributor blockages in pump-turbines were systematically analyzed by means of validated CFD simulations Figure 4.5 [30]. Different obstruction scenarios were considered, varying both the blockage size and its position within the flow passages.

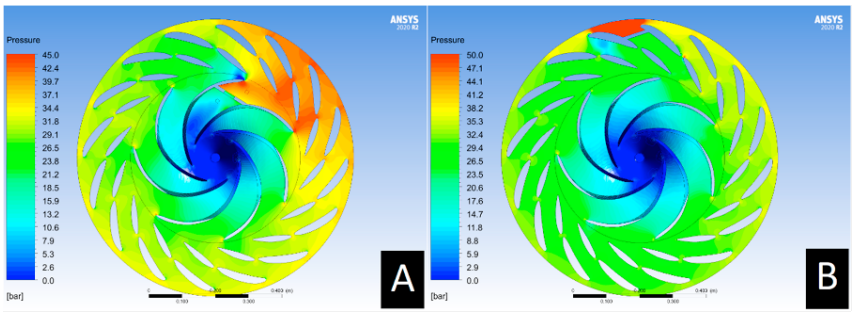

Figure 4.5: Examples of pressure contours obtained for studied cases: (A) obstructed rotor; (B) obstructed distributor [30]

The results demonstrated that runner blockages Figure 4.6agenerate strong hydraulic unbalances that rotate at the runner frequency, amplifying vibration levels

and leading to significant dynamic stresses. Moreover, the excitation amplitude was found to be larger when the blockage occurred closer to the turbine axis, due to the higher flow velocities in this region. Distributor blockages Figure 4.6b, on the other hand, were shown to induce non-uniform pressure distributions at the runner–distributor interface, exciting higher harmonics for partial obstructions and lower harmonics with larger amplitudes for complete blockages. These findings highlight how the presence of ingested bodies can alter the RSI characteristics of the machine, causing both increased vibration and potential cavitation, and thus represent a critical factor to consider when evaluating the dynamic reliability and fatigue life of hydraulic turbines.

(a) Typical runner blockage [31]

(b) Stones blocked in the spiral casing at the entrance of the stay vanes [31]

Figure 4.6: Blockage examples in different parts of the turbine

4.3 Cavitation

Cavitation occurs when local pressures in the flow drop below the vapor pressure, leading to the formation of vapor bubbles that collapse violently near the runner surfaces. These collapses generate shock waves and micro-jets, causing material damage, surface erosion, and potentially accelerating fatigue of turbine components [14, 32, 25]. In addition, cavitation can modify the flow characteristics inside the turbine, generating pressure pulsations, stochastic loads, and vortical structures such as inter-blade vortices or vortex ropes, which may interact with structural resonances, particularly under off-design operating conditions such as deep part load [33, 34, 35]. Recent investigations have shown that inter-blade cavitation vortices exhibit a distinctly stochastic rather than purely periodic behaviour, generating local pressure oscillations particularly on the suction side of the runner blades, with peak negative pressures near the trailing edge. Such oscillations may act as an amplification source for fatigue stresses on the runner [36]. Complementary CFD analyses have confirmed that these vortices originate from flow separation close to the hub region, where a collision between high-velocity jets and separated low-velocity zones produces intense vorticity and low-pressure cores. The simulations further showed that the development of inter-blade vortices is closely linked to the onset of negative incidence

angles at the hub, which explains the high probability of cavitation inception in this area [34].

The nucleation of cavitation can be homogeneous or heterogeneous, depending on local conditions. In hydro turbines, cavitation is largely heterogeneous, forming on blade walls or at interfaces between water and dissolved particles. Typical cavitation types in Francis turbines include travelling bubble cavitation, bubble cavitation beneath shear layers, localized attached cavitation, and detached (inter-blade) vortex cavitation [37, 32]. The leading edge and regions with adverse pressure gradients, such as near the crown curvature, are also prone to attached or shear-layer bubble cavitation. Bubble collapse generates intense noise, pressure pulses, and re-entrant jets that strike the blade surfaces, representing the main mechanism of cavitation erosion. The aggressiveness and onset of cavitation are influenced by blade design, operating load, Thoma number (the Thoma number is a dimensionless parameter used to assess the risk of cavitation in turbines) and water quality.

The Thoma number is calculated as:

$$\sigma = \frac{H_{atm} - H_v - H_s}{H}$$

where:

- H_{atm} = piezometric head corresponding to atmospheric pressure,
- H_v = piezometric head corresponding to the vapor pressure of water,
- H_s = suction head, i.e., the submergence level of the runner,
- H = net head of the turbine.

Travelling bubble cavitation usually occurs at high load when the pressure difference along the blade is large, and the local pressure drops below vapor pressure. Detached inter-blade vortex cavitation and cloud cavitation can occur under off-design or deep part-load conditions, producing large inter-blade cavities that enhance pressure pulsations and modify the effective added mass of the runner, potentially leading to structural resonance. In the study [33], a Francis turbine that suffered multiple trailing-edge blade fractures after just one day of deep part-load operation was analyzed. By incorporating the cavitation volumes identified through CFD simulations into the FSI model, the runner's natural frequencies increased, approaching the excitation frequencies from the Rotor-Stator Interaction and explaining the rapid crack propagation. This phenomenon has been linked to rapid fractures of Francis turbine blades, emphasizing that cavitation impacts both material wear and dynamic structural behavior.

Cavitation also reduces turbine efficiency. The rate of cavitation, defined as the interphase mass transfer between liquid and vapor, increases as the Thoma number decreases. Device modifications, such as fins on the runner, can mitigate cavitation effects at part-load by altering circumferential momentum and reducing low-pressure zones, while having negligible impact at the Best Efficiency Point (BEP) [35, 32].

Transient operating conditions—such as variable-speed operation, ramping, or start-stop sequences—can significantly influence cavitation dynamics. During transient conditions, flow accelerates or decelerates, and local velocities along the blade change continuously. This affects the formation, collapse, and aggressiveness of cavitation bubbles [34].

As confirmed by CFD, the presence of inter-blade vortices and associated backflow deteriorates the pressure distribution along the runner blade height, enhancing localised load fluctuations and vibration risks. These effects can increase the likelihood of structural resonances and accelerate material fatigue, underscoring the importance of blade profile optimization and incidence control strategies for safe deep part-load operation [34, 36]. Monitoring techniques have evolved to detect cavitation in real-time, mainly through high-frequency vibration measurements. Vibrations caused by collapsing bubble clouds are most effectively captured using acoustic emission (AE) sensors mounted on the rotating shaft. Sensors in stationary components are less reliable due to interference from other machine vibrations.

4.3.1 Erosive cavitation

Beyond its hydrodynamic and dynamic effects, cavitation is also associated with **erosive phenomena** that can seriously affect the integrity and lifetime of hydraulic turbine components. When vapor cavities collapse near solid surfaces, the implosion generates localized shock waves and micro-jets, producing pits, surface roughness, and eventually large-scale material loss. Over time, such erosion can accelerate fatigue crack initiation and propagation, representing a major concern for the long-term reliability of Francis turbines.

Escaler et al. [35] investigated sheet and cloud cavitation regimes in a cavitation tunnel using piezoelectric accelerometers with sensitivity up to 200 kHz. Their results showed that cloud cavitation is much more unstable and aggressive than sheet cavitation, with characteristic shedding Strouhal numbers of about 0.28 and 0.16, respectively (dimensionless number defined as $St = \frac{fL}{U}$, where f is the shedding frequency of cavitation clouds, L a characteristic length such as the hydrofoil chord, and U the reference flow velocity). Most importantly, the authors demonstrated a direct correlation between high-frequency vibration levels induced by cavitation and the measured erosion rate (pitting rate) on stainless-steel specimens.

More recent investigations on Francis turbines confirmed that cavitation erosion can lead to severe material loss, with penetration rates reported up to 10 mm per year on runner blades and casings [30]. The aggressiveness of erosive cavitation is further exacerbated under extended off-design operation, particularly at high heads and intermediate guide vane openings, where bubble collapse intensifies local stresses [38]. In addition, vibration analyses have shown that the 800–1000 Hz frequency band is a reliable indicator of bubble impact events on metallic surfaces, thus providing an effective diagnostic tool for detecting erosive cavitation in situ [38].

These findings highlight that **high-frequency vibration monitoring** can be

used as a reliable proxy for erosive potential, offering a practical tool for predicting material damage in hydraulic machinery. From a design and operation perspective, this underlines the importance of controlling cavitation regimes not only to maintain efficiency and avoid pressure pulsations, but also to minimize long-term erosive damage on runner blades and other wetted components.

4.4 Vortex rope

One of the most characteristic flow instabilities in Francis turbines at off-design operation is the development of the **draft tube vortex rope**. When operating at **part-load conditions**, a swirl component develops at the runner outlet due to the mismatch between guide vane angle and runner blade incidence. This swirl induces a central low-pressure region in the draft tube that breaks down into a rotating cavitating vortex, commonly referred to as the vortex rope [39, 40].

The vortex rope can manifest in two main forms:

- a **precessing helical vortex** at part load, rotating at a frequency typically around one third of the runner rotational speed ($f_R \approx \frac{1}{3} f_n$);
- an **axisymmetric vortex** at overload conditions, where the high discharge stabilizes the cavitated core.

At part load, the helical rope produces strong **rotating pressure fields** across the draft tube cross-section, causing asymmetric loads and flow plunging at the elbow. These cyclic loads can couple with the natural frequencies of the hydraulic system, leading to **hydraulic resonance** and large-scale oscillations of torque, head, and power output [39, 38, 41].

From a structural perspective, the fluctuating pressure field acts as a periodic excitation on the runner and shaft line. If the rope frequency or its harmonics coincide with runner or hydraulic circuit eigenfrequencies, severe **fatigue loading** may occur, accelerating crack initiation and propagation [40]. Monitoring and CFD-based studies confirm that the vortex rope amplifies **dynamic stresses** in critical areas such as the trailing edge and crown junction of runner blades, where fatigue failures have been reported in prototypes [40, 42].

The vortex rope is also associated with strong **cavitation phenomena**. Cavitation bubbles develop in the low-pressure vortex core and collapse violently downstream, adding broadband pressure fluctuations and noise to the system. This combination of cavitation and vortex-induced pulsations reduces efficiency and increases the risk of **erosion and structural resonance** [39, 38, 41].

Chapter 5

Rotor–Stator Interaction

Rotor–stator interaction (RSI) is one of the most critical hydraulic and structural phenomena in pump-turbines and Francis turbines, as it strongly affects both efficiency and mechanical integrity. RSI arises from the periodic interaction between the stationary guide vanes and the rotating runner blades, both of which are cyclic–symmetric structures. As the runner rotates, the wakes shed from the guide vanes periodically impinge on the runner blades, generating fluctuating forces that excite the structure at specific frequencies and nodal diameters (ND). These pressure fluctuations propagate through the vaneless space (VS), the guide vane cascade, and further upstream into the spiral casing and inlet conduit, affecting not only the runner but also external components of the powerhouse [43, 29].

5.1 Origin and Mechanisms

The excitation mechanism of RSI can be divided into two main contributions:

- **Potential flow effect:** The rotating runner blades periodically disturb the inviscid flow field in the VS, leading to pressure fluctuations that propagate upstream and downstream. These disturbances decay quickly, but can still trigger structural vibrations when they coincide with natural frequencies.
- **Viscous flow effect:** Wakes generated by the guide vanes create a non-uniform velocity distribution at the vane outlet. Flow separations, secondary flows, and non-ideal flow angles in the distributor amplify this effect, resulting in strong hydrodynamic excitation when the runner blades pass through these wakes.

In stationary conditions, the wake effect produces a non-uniform periodic flow at the guide vane outlet (Figure 5.1a). In rotating conditions, the runner blades introduce additional periodic distortions in the flow field (Figure 5.1b). The combination of both effects gives rise to complex flow patterns (Figure 5.1c).

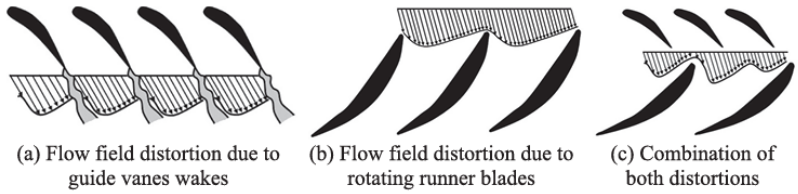

Figure 5.1: Schematic representation of rotor–stator interaction (RSI): (a) stationary reference frame, non-uniform wake at guide vane outlet; (b) rotating reference frame, periodic distortion introduced by runner blades; (c) combined effect leading to complex flow patterns. [44]

5.2 Frequency Characteristics

The dominant frequencies associated with RSI are the *blade passing frequency* (BPF) and its harmonics:

$$f_{\mathrm{BPF}} = Z_r \cdot f_n \quad \text{(stationary frame)}, \qquad f_{\mathrm{RSI}} = Z_s \cdot f_n \quad \text{(rotating frame)},$$

where Z_r and Z_s are the number of runner blades and guide vanes, respectively, and f_n is the rotational frequency of the runner. The phase of pressure pulsation depends on the number of runner blades and guide vanes, while the excitation frequency depends on the shaft rotational speed. The superposition of these excitations generates a spectrum of harmonic frequencies, some of which may coincide with natural structural frequencies, thus inducing resonance [45, 37, 46, 38].

Nodal Diameter Modes

Experimental investigations have been conducted to determine the natural frequencies and nodal diameter modes of pump-turbine runners. Egusquiza et al. [47] performed impact hammer tests with accelerometers mounted on the runner, allowing the identification of modal parameters and the validation of FEM simulations.

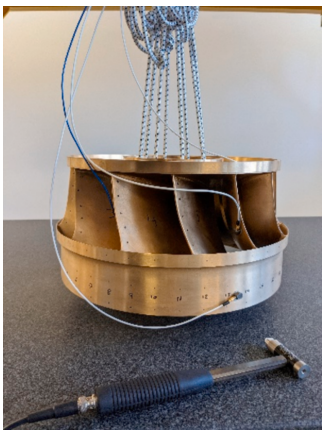

Figure 5.2: Runner used for the test [48]

More recently, Egusquiza et al. [48] demonstrated the feasibility of detecting runner vibrations with stationary sensors installed on the casing, by exciting the runner with piezoelectric patches and comparing the measured response in both rotating and stationary frames. These experimental studies also revealed the significant influence of the surrounding fluid on the modal response. While tests in air provide a first estimate of the natural frequencies, the presence of water leads to a substantial frequency reduction due to added mass effects. Reported differences are typically in the range of 30–40%, and in some cases can reach up to 50% depending on the mode shape and the specific geometry of the runner [47, 49].

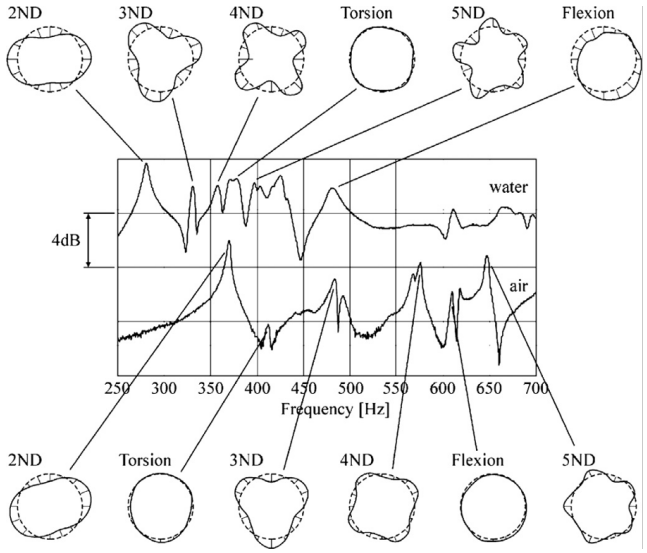

Figure 5.3: Frequency responses and nodal diameters for a model Francis runner in air and water [50]. The runner has the following properties: specific speed ($\nu = 0.56$), material density 8300 kg/m^3, runner mass 55 kg, Young's modulus 110 GPa, Poisson's ratio 0.34, reference diameter 0.4 m, and 17 blades.

The dynamic response of runners is usually described in terms of *nodal diameters*, where a vibrational mode with k nodal diameters is characterized by k diametrical lines crossing at the runner center, dividing the periphery into $2k$ sectors oscillating in opposite phase. The 2-ND and 3-ND modes are the most relevant from an engineering point of view, as they are the ones most easily excited by the RSI. The next Figure 5.4 illustrates the frequency response obtained from accelerometer for the 2-ND and the 3-ND traveling waves mode, highlighting the difference between forward (red) and backward (blue) propagation with respect to the runner rotation.

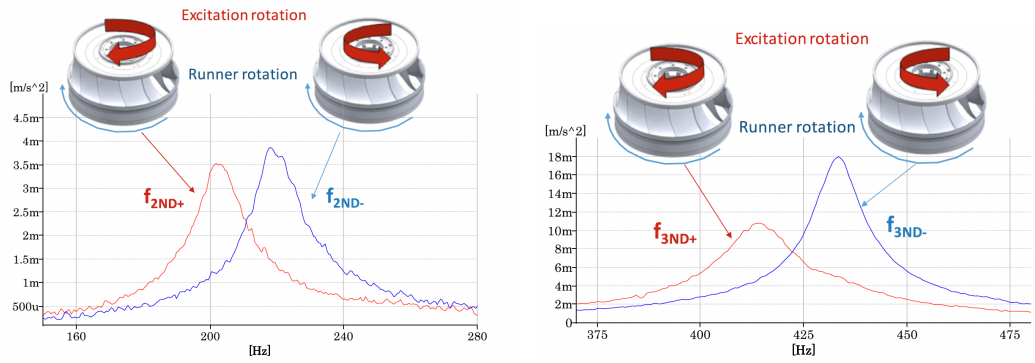

(a) Frequency response from accelerometer to 2-ND traveling wave in same (red) and opposite (blue) direction of runner rotation [48]

(b) Frequency response from accelerometer to 3-ND traveling wave in same (red) and opposite (blue) direction of runner rotation [48]

Figure 5.4: Representation of frequency response for different nodal diameter

In parallel with these experimental investigations, numerical simulations were also conducted to support and complement those measurements. Finite element models, see Figure 5.5, often coupled with fluid-structure interaction (FSI) analyses, were employed to predict natural frequencies, mode shapes, and deformation patterns of the runner [51]. The numerical results generally showed good agreement with the experimental observations, and provided additional insights into the added mass effect, the influence of fluid forces, and the relative deformation between crown and band [52, 47, 50].

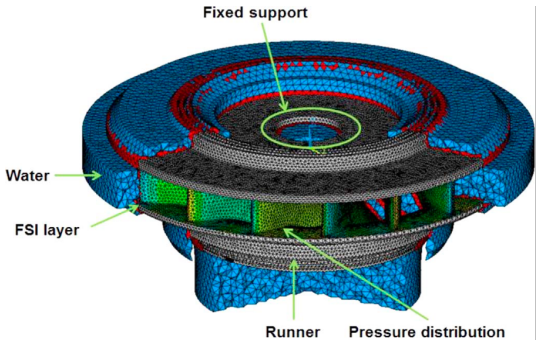

Figure 5.5: FEM model of the turbine runner and surrounding fluid domain [52]

In the 2-ND mode, as shown in Figure 5.6, the crown and the band deform mainly in the axial direction, moving in phase, while the eye region exhibits a marked radial displacement.

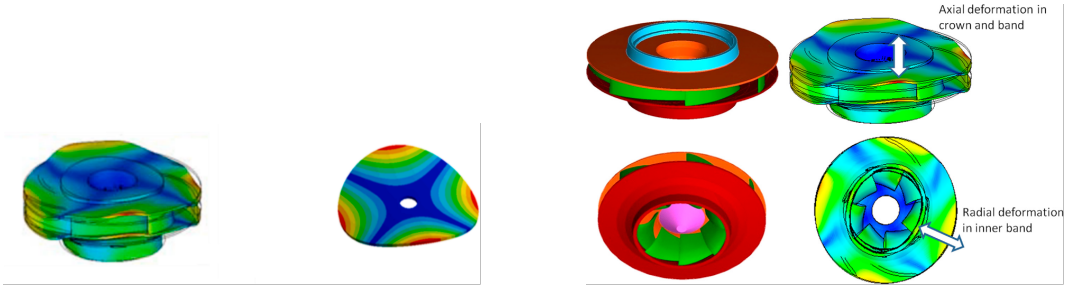

(a) 2-ND mode shape for a pump-turbine runner (left) and a disc (right) [48]

(b) 2-ND mode for pump-turbine impeller [47]

Figure 5.6: Representation of the typical deformation of the rotor

In the 3-ND mode, the deformation pattern shows three nodal diameters: crown and band again move in phase, although the crown generally experiences larger displacements than the band. Because of the geometry of pump-turbine runners, typically with an odd number of blades and wide span angles, the modal response is not perfectly symmetric. For the same ND value, different variants may appear, such as in-phase, counter-phase, crown dominant or band-dominant deformations [47, 49].

5.3 Diametrical Vibration Modes

Through both theoretical and experimental studies, Tanaka [53] developed a model to determine the diametrical vibration modes in high-head pump-turbines. Due to the large thickness of the guide vanes, a significant hydraulic excitation force is generated when the runner blades pass through the wakes shed by the vanes. This interference induces vibrations in the runner at characteristic frequencies, which, as introduced in Sec. 5.2, correspond to multiples of the RSI in the rotating frame and multiples of the BPF in the stationary frame.

The vibration mode with k diametrical nodes can be identified using:

$$n\,Z_g \pm k = m\,Z_r, \quad n, m \in \mathbb{Z}^+.$$

This relation expresses that a vibration mode with k nodes can only be excited when the interference between runner and guide vanes satisfies a structural resonance condition. Tanaka interpreted this in terms of progressive and retrogressive waves travelling along the runner periphery. In his formulation, the amplitudes of these waves vanish unless the denominator of the response function becomes zero, which happens exactly when the condition above is satisfied. In other words, as represented in Figure 5.7, only specific combinations of guide vane number, runner blade number, and node number lead to physically realizable diametrical modes. Moreover, Tanaka showed that in real machines the observed mode shapes often result from the superposition of two elementary counter-phase modes, which satisfies the structural boundary conditions imposed by the blades.

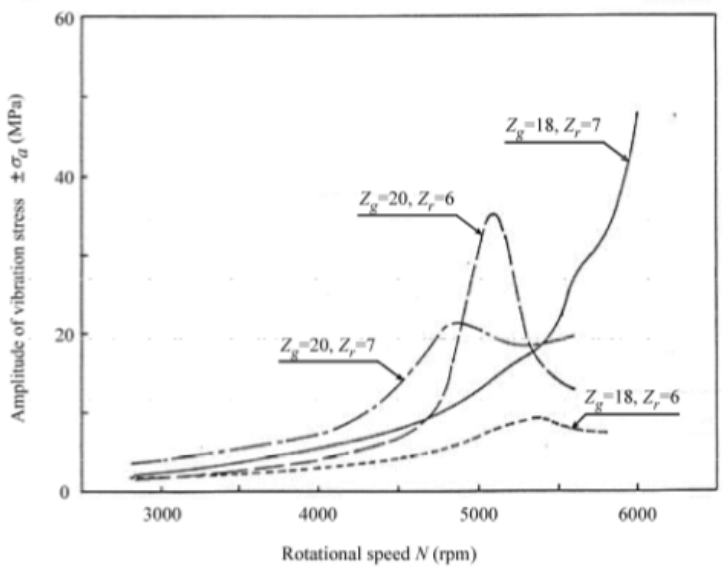

Figure 5.7: Experimental results of the resonance curves for different combination of number of rotor and stator blade [53]

The same resonance condition can also be found in the earlier model of Kubota et al. [54], who expressed it as:

$$hZ_v \pm N = qZ_b,$$

where Z_b and Z_v are the numbers of moving and stationary blades, respectively, N is the excited diametrical mode, and h and q are integers related to harmonic orders. In this approach, the excitation frequencies are restricted to harmonics of the BPF, and each harmonic can excite a specific diametrical mode in forward or backward direction depending on the sign. An example of the predicted combinations for $Z_b = 7$ and $Z_v = 16$ is given in Table 5.1. Although Kubota's method generates a large number of possible excited modes, it is generally the lower-order modes that dominate the vibration spectrum [45] [54].

Table 5.1: Expected frequencies and diametrical modes [45]. N: excited diametrical mode; h: harmonic order of the stator excitation; q: harmonic order of the rotor excitation; (+) / (–) indicates forward/backward propagation of the mode.

N	h					
	1	2	3	4	5	...
1	—	—	—	(–) $q = 9$	—	
2	(–) $q = 2$	—	—	—	—	
3	—	(+) $q = 5$	—	—	(–) $q = 11$	
4	—	(–) $q = 4$	—	—	(+) $q = 12$	
5	(+) $q = 3$	—	—	—	—	
6	—	—	(–) $q = 6$	—	—	
7	—	—	—	(+) $q = 10$	—	
8	—	(–) $q = 4$	—	(–) $q = 8$	—	
9	(–) $q = 1$	—	—	—	—	
⋮						

Tanaka's model provided a theoretical framework that explained why only certain diametrical modes could exist, linking the excitation directly to the structural response of the runner. Kubota's formulation, although simpler, offered a practical way to enumerate the possible harmonics and excited modes.

Egusquiza et al. [46] conducted a study on RSI, and Figure 5.8 depicts the sequence of blade–vane interactions for a machine with $Z_s = 20$ guide vanes and $Z_r = 6$ runner blades. In the first interaction, blade 1 of the runner faces guide vane 1 (Figure 5.8a); as the runner rotates slightly clockwise, blade 4 meets vane 8 (Figure 5.8b), blade 2 faces vane 15 (Figure 5.8c), and so forth.

Each runner blade experiences the same pressure pulsation, but with a **phase shift** relative to the other blades. For instance, when the pulsation on blade 1 reaches its maximum, other blades may experience a minimum or a different value depending on their relative position. This phase distribution generates the overall diametrical pattern of the excitation.

For the 2ND mode shown in Figure 5.8, there are two positive and two negative pressure pulses around the runner at any instant. The rotational direction of these diametrical modes can be opposite to the runner rotation.

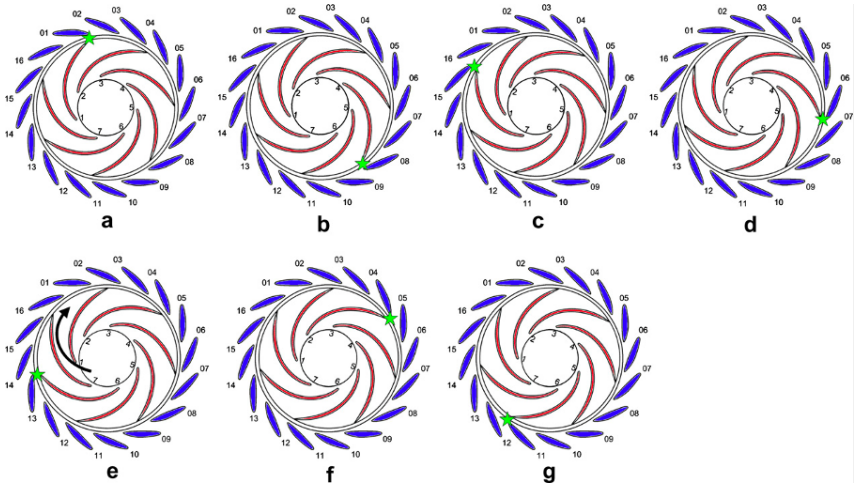

Figure 5.8: Rotor-stator interaction sequence for a 7-blade runner, 16 guide vanes machine [46]

The shape of the pressure pulsation generated by the RSI around the whole runner can be determined with the Kubota et al. model [54]:

$$hZ_g - k = qZ_b$$

For this combination of blades and vanes ($Z_b = 7$, $Z_g = 16$), the main diametrical mode of the excitation is $k = 2$, rotating opposite the runner rotation. This means that at any instant there are two positive and two negative pressure pulses around the runner. This is a two-nodal diameter (2ND) excitation.

Table 5.2 shows the complete sequence of interactions, indicating which blades interact with which vanes. When these excitations occur in phase, they generate a vibration mode with two diametrical nodes (2ND) [46].

Table 5.2: RSI characteristics: rotor-stator interaction sequence [46].

Iteration, n	1	2	3	4	5	6	7	8
Runner blade number	1	4	7	3	6	2	5	1
Stator vane number	1	8	15	6	13	4	11	2

Another relevant study led by Rodriguez et al. [37] demonstrated that RSI can be effectively monitored not only through pressure measurements distributed along the perimeter of the impeller-runner, but also via vibrations measured directly on the rotating shaft.

5.4 Impact on Operation

RSI manifests differently depending on turbine operating conditions:

- **Low load (small GVO):** The vaneless space is relatively large, reducing RSI intensity. The amplitude of BPF is significant, but strong low-frequency

fluctuations may dominate due to operation far from the best efficiency point (BEP).

- **Medium load (critical GVO):** The vaneless space decreases, leading to higher RSI intensity. Low-frequency stochastic fluctuations appear with amplitudes comparable to the BPF.
- **High load (near BEP/overload):** The vaneless space shrinks drastically, producing a sharp increase in RSI intensity. The BPF becomes dominant, while low-frequency components diminish.

5.5 Transient Effects

During start-up and shutdown sequences, the runner accelerates or decelerates, producing a frequency sweep of RSI excitations. If this sweeping frequency coincides with structural eigen frequencies, transient resonance may occur, leading to high stress levels in the runner [46]. RSI may also interact with upstream penstock waves, intensifying the excitation and potential for resonance. Several numerical and experimental investigations have been carried out to better understand these transient phenomena in Francis turbines. In particular, unsteady CFD analyses of rotor–stator interaction and vortex rope formation have shown how pressure fluctuations evolve during off-design and time-dependent operating conditions. These studies highlighted the strong coupling between hydraulic instabilities and transient loads, confirming that resonance effects and flow-induced vibrations are critical aspects to consider when assessing the dynamic behavior and structural reliability of hydraulic turbines [55].

5.6 Consequences for Powerhouse Structures

The pressure waves generated by RSI propagate throughout the hydraulic machine and may excite external components such as columns, foundations, and floors. On-site studies report intense vibrations of local components linked to RSI-induced pressure fluctuations, emphasizing the critical importance of this phenomenon for both turbine safety and structural integrity [19].

Chapter 6

Objective of the Study

The main objective of this thesis within the framework of the **STOR-HY** European project is to design and validate a *data processing and validation tool*. This tool is essential to establish the robust baseline and predefined thresholds required by the project's future Artificial Neural Network (ANN) virtual sensor. Once developed, the ANN sensor will be capable of monitoring critical operating parameters in real time, providing an early-warning signal to the control interface or triggering an automatic shutdown when the monitored variables approach the critical thresholds. This strategy is intended to enhance turbine safety and reliability, reducing the risk of damage due to fatigue, cavitation, or rotor–stator interaction (RSI) phenomena.

To achieve this goal, the work focuses on four main aspects:

- **Data preprocessing and validation.** A dataset containing measured operational signals was analyzed and validated at a qualitative level. Several candidate databases were compared by examining the quality of the raw data, the sampling frequencies, and the spectral contents of the signals. In particular, Fourier analysis was employed to identify dominant frequency components and to compare them with analytical estimations of RSI excitations, which depend on the number of runner blades and guide vanes.

- **Analytical vs Experimental comparison.** By combining analytical formulas for RSI frequencies with FFT analysis of the measured signals, discrepancies between theory and measurements were quantified. This step allowed for the assessment of data consistency and the identification of the most representative operating conditions for training purposes.

- **Optimization of sampling requirements.**

  A primary objective of this study was to define the minimum sampling frequency necessary to preserve spectral integrity while reducing computational overhead. The developed tool implements a physics-informed approach that automatically identifies the dominant spectral peak (f_{max}) and recommends an optimized sampling rate, typically set at five times f_{max} to ensure a robust safety margin above the theoretical Nyquist-Shannon limit. The methodology validates this

data reduction through a professional decimation pipeline that applies a low-pass anti-aliasing filter before subsampling. This process ensures that the signal's original characteristics are preserved.

- **Preparation for machine learning models.** Preparation for machine learning models. Once the dataset was validated, it was structured to serve as input for neural network models in the training phase. In particular, the preprocessing pipeline was designed to extract physically meaningful features from the signals, primarily through spectral analysis and normalization in the order domain. The quality and suitability of the training data were ensured by systematically validating the spectral consistency of the signals and by defining appropriate analysis windows for feature extraction. This approach allows the dataset to retain the key information related to hydrodynamic phenomena while reducing redundancy and noise. As a result, the processed dataset is not only optimized in terms of size and consistency, but also formatted in a generalized and scalable manner, making it suitable for the development of robust and transferable machine learning models for virtual sensing applications.

The purpose of this work lies in the integration of traditional hydraulic turbine monitoring with modern data-driven approaches. While previous studies have shown how numerical simulations and experimental measurements can characterize unsteady hydrodynamic effects such as RSI or vortex rope formation, this study aims to develop a practical tool for real-time diagnosis. The final AI virtual sensor will therefore be able to reproduce the expected physical behavior of the machine and also to provide actionable information for preventive maintenance and control strategies.

Chapter 7

Francis-99 Case Study

7.1 Background and Motivation

The Francis-99 initiative was created to address limitations in the analysis and design of hydraulic turbines, particularly Francis turbines, due to the scarcity of publicly available experimental data and the complexity of the fluid dynamics involved. Key challenges include restricted access to modern turbine designs because of industrial confidentiality, difficulties in validating numerical models due to complex flows characterized by high Reynolds numbers, flow separation, secondary vortices, cavitation, and hydraulic losses, as well as the high cost of performing rigorously verified CFD simulations.

Francis-99 provides open-access experimental data and reference designs, offering benchmark cases for the verification and validation of computational fluid dynamics (CFD) and fluid-structure interaction (FSI) models. To date, three workshops have been held: the first focused on steady-state operating conditions, the second on transient events such as load variations and start-stop sequences, and the third on fluid-structure interactions in Francis turbines and hydrofoils.

7.2 Experimental Facility

The Francis-99 experiments were carried out at the Waterpower Laboratory of NTNU, which has been active in turbine research and development since 1917. The laboratory is equipped with state-of-the-art infrastructure that allows the operation of test rigs in a variety of prototype-like configurations. Among its facilities are two major test rigs dedicated to Francis/pump-turbines and Pelton turbines, capable of conducting experiments in compliance with IEC 60193 standards. The maximum hydraulic efficiency achieved with the Francis-99 model turbine is 93.4%. In addition, the laboratory hosts smaller rigs for basic research, including hydrofoil rigs in three configurations: single hydrofoil, a linear cascade of three hydrofoils, and a radial cascade of eight hydrofoils. The conduit system can be pressurized up to 100 m head, with 700 kW pumping power available and a maximum discharge of 1.1 m^3/s. The infrastructure is regularly upgraded, with major improvements completed in 2003,

2007, and most recently in 2023, including the turbine generator, conduit system, and flow measurement instruments.

The Francis-99 turbine is a scaled model (1:5.1) of the turbines operating at the Tokke power plant in Norway. It is a splitter-blade type runner with 15 full blades and 15 splitters, with leading edge profiles designed to be similar. The blades are twisted up to 180° along their chord length, from inlet to outlet, and the trailing edge thickness is approximately 3 mm. The runner inlet and outlet diameters are 0.630 m and 0.349 m, respectively. During model tests conducted in 2012, the best efficiency point (BEP) efficiency was measured at 93.4% with an uncertainty of ±0.16%. The Francis-99 facility is extensively used for studies on rotor-stator interaction (RSI), vortex rope formation, rotating stall in pump-turbine runners, water hammer, and cavitation. The open-loop hydraulic system is particularly suited for transient tests, including load variations, start-stop conditions, and total load rejection experiments.

7.3 Test Case Description

The Francis-99 turbine test rig consists of a closed hydraulic loop. Water from the basement reservoir (9) is pumped to an overhead tank (2), from where it flows down through the turbine (7). A feed pump (1) is operated at a constant speed to maintain a fixed head. The draft tube outlet connects to a downstream vessel (8), where the head is maintained at atmospheric pressure, and excess water is returned to the basement reservoir (9). The test rig can generate up to 16 m of head in open-loop operation and up to 100 m (for flow rates ≤ 0.5 m^3/s) in closed-loop operation.

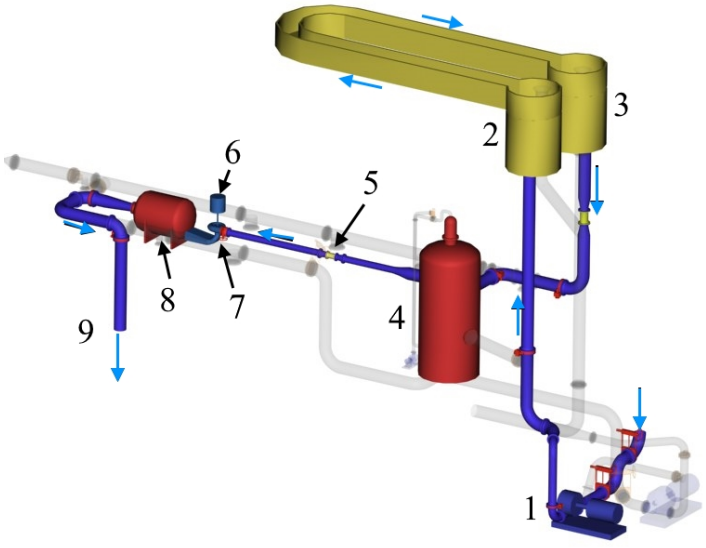

Figure 7.1: Open-loop hydraulic system of the model Francis turbine at the Waterpower Laboratory, NTNU. 1 – feed pump, 2 – overhead tank-primary, 3 – overhead tank-secondary, 4 – pressure tank, 5 – magnetic flowmeter, 6 – generator, 7 – Francis turbine, 8 – downstream tank and 9 – basement. [56]

The Francis-99 model turbine includes 14 stay vanes integrated in the spiral casing, 28 guide vanes, a runner with 15 blades and 15 splitters arranged alternately,

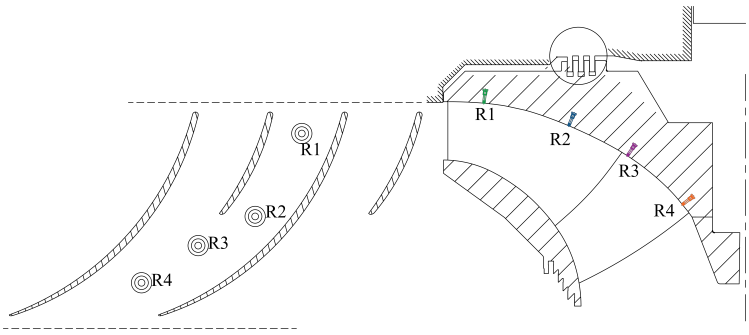

Figure 7.2: Locations of pressure sensors in the Francis-99 runner [56]

and an elbow-shaped draft tube. The runner inlet and outlet diameters are 0.63 m and 0.347 m, respectively. The runner is directly coupled to a DC generator, which can also function as a motor in pump mode. The facility is often used for industrial model tests in closed loop configurations (30 m head, $Re = 4 \times 10^6$) and is equipped with standard instruments to measure head, discharge, torque, water temperature, and rotational speed.

7.4 Measurements and Data Acquisition

Pressure measurements were carried out on the Francis-99 runner, with sensor locations shown in Figure 7.2 and coordinates listed in Table 7.1. The sensors allow determination of the guide vane passing frequency (f_{gv}) and its harmonics at different runner positions. Measurements were conducted at five operating points with fixed guide vane opening, but varying runner speeds and heads (summarized in Table 7.2). The results showed significant variations in RSI amplitudes, with relatively high values observed at certain conditions. These high amplitudes suggest the presence of resonance phenomena under those operating points, which are of interest for further numerical analysis.

Sensor name	x (mm)	y (mm)	z (mm)	Type	Mount
R1	180.50	158.81	21.73	Entran 7bar	Flush
R2	84.30	132.85	-9.50	Entran 7bar	Flush
R3	25.75	118.88	-31.61	TE XP5	Flush
R4	-17.40	85.19	-59.59	TE XP5	Flush

Table 7.1: Pressure sensor locations [56]

Description	Flow rate (m^3s^{-1})	n_{ED}	Q_{ED}	Head (m)	α (degree)	Speed (rpm)
BEP-1	0.134	0.179	0.154	5.2	10	219.8
BEP-2	0.160	0.176	0.156	7.2	10	254.3
BEP-3	0.183	0.178	0.154	9.6	10	297.8
BEP-4	0.209	0.178	0.155	12.6	10	340.5
BEP-5	0.232	0.180	0.154	15.55	10	381.7

Table 7.2: Operating parameters and range [56]

A number of challenges are associated with blade loading measurements in the Francis-99 runner. First, the runner blades are bolted to the crown and band, creating the possibility of rotational asymmetry due to assembly conditions. Moreover, the trailing edges of the blades near the band are free over a length of about 94 mm (Figure 7.3), resulting in variations in the gap between blade and band. Impact hammer tests indicated differences in blade preloading (likely due to pretension). A second challenge lies in the crown design, which includes several holes and cable channels (Figure 7.4) for pressure measurements. These openings introduce asymmetrical stiffness, meaning the crown's bending stiffness depends on the direction of bending. Consequently, uncertainties in strain measurements at these locations must be carefully considered. For this reason, the test case is mainly limited to FSI studies based on pressure measurements.

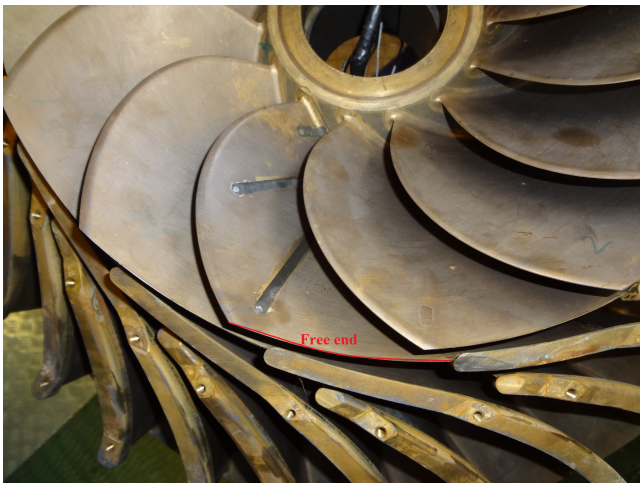

Figure 7.3: Francis-99 runner with free end trailing edge joined to band (marked in red color) [56]

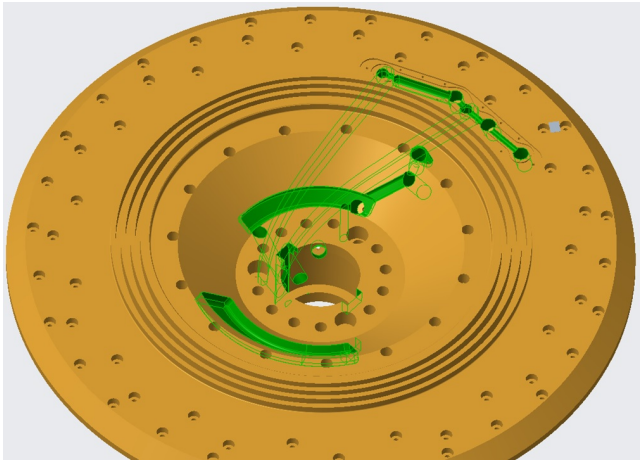

Figure 7.4: Francis-99 runner with holes on the crown for the pressure sensors and the instrumentation [56]

The pressure sensors were statically calibrated using a dead-weight tester as the primary reference. All components in the pressure measurement chain, from sensors to the data acquisition system, have resonance frequencies above 10 kHz. Therefore, dynamic uncertainty is considered negligible, and only repeatability and hysteresis contribute to the overall uncertainty. A repeatability test at 1 Hz with alternating pressures of 100 kPa and 90 kPa absolute confirmed the calibration. The uncertainty budget for RSI amplitudes is summarized in Table 7.3. Additionally, vibration tests with the runner in air were conducted to check for vibration sensitivity of the pressure sensors, and no additional uncertainty was observed.

Location	BEP-1	BEP-2	BEP-3	BEP-4	BEP-5
R1	0.979 ± 0.034	1.053 ± 0.024	1.077 ± 0.021	1.074 ± 0.019	1.082 ± 0.018
R2	0.714 ± 0.036	0.775 ± 0.027	0.802 ± 0.020	0.803 ± 0.015	0.818 ± 0.014
R3	0.550 ± 0.025	0.591 ± 0.018	0.605 ± 0.015	0.611 ± 0.013	0.623 ± 0.011
R4	0.295 ± 0.024	0.337 ± 0.023	0.348 ± 0.023	0.348 ± 0.015	0.359 ± 0.013

Table 7.3: Amplitudes pertained to rotor–stator interaction (f_{GV}). The amplitudes are in percentage of head value at the corresponding operating point. [56]

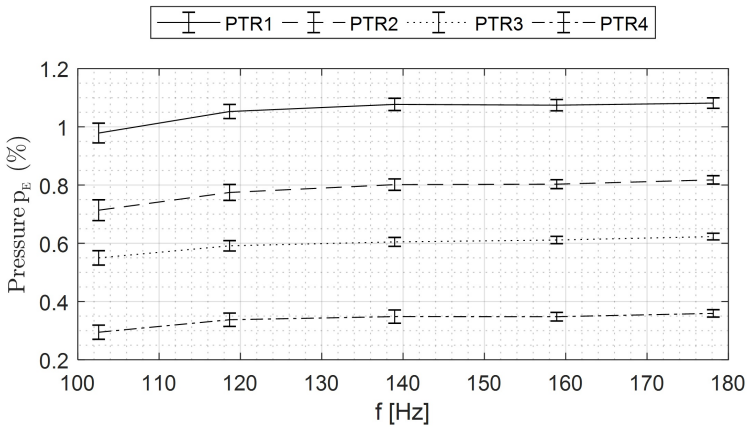

Figure 7.5: Rotor stator interaction fundamental frequency ($f_{\mathbf{GV}}$). Amplitudes are normalized by the head value of the corresponding operating point [56].

RSI amplitudes were normalized with respect to head at each operating point. The uncertainty includes the 95% measurement confidence interval and the 95% probability of amplitude variations, obtained using short-time Fourier transform (STFT). The analysis used a window length of 100 RSI signal periods with 50% overlap. Results showed that the second harmonic of the guide vane passing frequency increased toward measurements at 280 Hz (Figure 7.6), suggesting resonance with the nodal diameter 4 (ND4) mode. The main objective of the third Francis-99 workshop was therefore to perform FSI simulations to analyze pressure distributions in the runner channels under resonance. Although a single CFD analysis could reproduce the excitation pressures, alternative excitation methods could also be used to impose an ND4-type pressure field. The aim was not to match the exact resonance frequency, given uncertainties in runner assembly, but rather to replicate the spatial pressure distribution observed in experiments. Exact amplitude matching with measurements was not considered essential.

Location	BEP-1	BEP-2	BEP-3	BEP-4	BEP-5
R1	0.086 ± 0.034	0.109 ± 0.029	0.152 ± 0.024	0.091 ± 0.020	0.076 ± 0.017
R2	0.072 ± 0.033	0.097 ± 0.028	0.167 ± 0.024	0.091 ± 0.021	0.059 ± 0.017
R3	0.056 ± 0.020	0.080 ± 0.019	0.154 ± 0.019	0.072 ± 0.016	0.041 ± 0.011
R4	0.042 ± 0.031	0.050 ± 0.026	0.124 ± 0.023	0.045 ± 0.019	0.025 ± 0.016

Table 7.4: Amplitudes pertained to rotor–stator interaction (harmonic $2f_{GV}$). The amplitudes are in percentage of head value at the corresponding operating point [56].

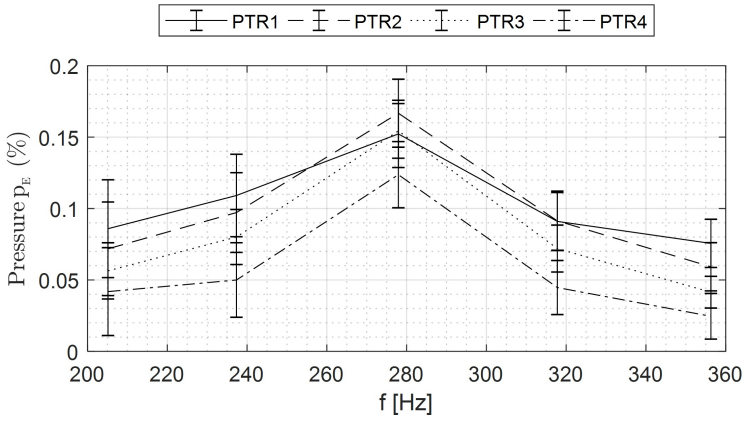

Figure 7.6: Rotor stator interaction harmonic frequency ($2f_{\mathbf{GV}}$). Amplitudes are normalized by the head value of the corresponding operating point [56].

Chapter 8

Implementation

In order to achieve the objectives defined in chapter 6, a specific computational tool was developed. The implementation of this code represents the core contribution of the present thesis, as it enables the processing of experimental data and the identification of dynamic phenomena affecting turbine performance. The following sections describe the methodology adopted, the structure of the implemented code, and the main results obtained from its application.

8.1 Dataset Selection and Validation

At the beginning of the research, several publicly available datasets were examined. However, these datasets proved unsuitable for the purposes of the present work, mainly due to limitations such as insufficient sampling frequency or the absence of variables of direct interest for the analysis. The process of identifying an appropriate dataset was therefore particularly time-consuming, requiring a careful evaluation of the available information and its quality.

To guide this process, specific requirements were established, including:

- a minimum sampling frequency sufficient to resolve pressure pulsations and rotor–stator interaction phenomena;
- constant sampling intervals, in order to avoid interpolation procedures that could compromise data accuracy;
- the availability of synchronized operating parameters, such as rotational speed and guide vane opening;
- a measurement duration long enough to ensure robust spectral analysis.

Datasets not meeting these requirements were excluded from consideration.

For this study the dataset provided by the Norwegian University of Science and Technology (NTNU) for academic purposes was selected [56]. This dataset, belonging to the Francis-99 initiative, is widely recognized as a benchmark case for the validation of computational models in hydraulic turbomachinery. Its adoption enabled the development of a robust and generalizable code and also allowed for

the validation of the obtained results through comparison with the analyses already supplied by the dataset authors. In this way, the research outcomes could be based in reliable experimental data and connected more solidly to the existing scientific literature.

It should be noted that, although the NTNU dataset originates from a scaled laboratory model rather than from a full-scale industrial unit, it provides high-quality, well-documented signals that are particularly suitable for methodological development and validation. As such, it represents an optimal compromise between experimental reliability and research accessibility.

8.1.1 Dataset Characteristics

The selected dataset consists of 25,000 uniformly sampled data points and includes a total of nine variables, both dynamic signals and operating parameters. The dataset used in this thesis was acquired under steady-state operating conditions, specifically at the best efficiency point (BEP) of the Francis-99 turbine. This ensures that the recorded signals are not affected by transient phenomena such as startup, shutdown, or load changes, thus providing a reliable basis for spectral analysis and methodological development. In addition to the BEP, the Francis-99 dataset also includes measurements at part load (PL) and high load (HL), which represent alternative steady-state operating conditions. The structure of the dataset is summarized in Table 8.1:

Table 8.1: Summary of the variables included in the NTNU dataset.

Variable	**Unit**	**Description**
t	s	Time vector of the acquisition
VL2	kPa	Pressure measurement at location VL2
DT5	kPa	Pressure measurement at location DT5
DT6	kPa	Pressure measurement at location DT6
P_{in}	kPa	Inlet pressure
H	m	Net head
Q	m^3/s	Volumetric flow rate
Ω	rad/s	Angular velocity of the runner
α	deg	Guide vane opening angle

For the pressure measurements, a pressure sensor VL2 was mounted at the vaneless space, and two pressure sensors DT5 and DT6 were mounted at the draft tube cone. Exact locations of the sensors and observed uncertainties are provided in Table 8.2.

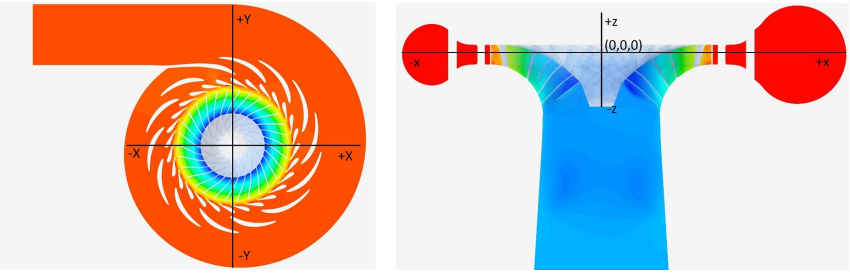

Figure 8.1: Global coordinates for the measurement locations and geometry [56]

Table 8.2: Locations of pressure sensors in the turbine.

Sensor	x [mm]	y [mm]	z [mm]	Uncertainty [%]
VL2	-320.0	62.2	-29.4	±0.01
DT5	-149.1	-100.6	-305.8	±0.10
DT6	149.1	100.6	-305.8	±0.10

The dataset therefore provides both local pressure measurements, necessary to analyze unsteady hydrodynamic phenomena (RSI and pressure pulsations) and global operating parameters (head, discharge, speed, and guide vane angle) that allow the characterization of the turbine operating condition. Table 8.3 reports the first five rows of the dataset as an illustrative example.

Table 8.3: First five rows of the NTNU dataset.

t[s]	VL2[kPa]	DT5[kPa]	DT6[kPa]	Pin[kPa]	H[m]	Q[m^3/s]	Omega[rad/s]	Alpha[deg]
0.0004	173.0300	0.3360	0.1210	216.8740	11.9620	0.2030	34.8290	9.8400
0.0006	173.2940	0.3010	0.0700	217.0490	11.9740	0.2030	34.8290	9.8400
0.0008	173.2120	0.2370	0.0190	216.8730	11.9510	0.2040	34.8290	9.8400
0.0010	173.7970	0.1740	-0.0340	216.8850	11.9450	0.2050	34.8290	9.8400
0.0012	174.0960	0.1140	-0.0710	217.0480	11.9430	0.2030	34.8290	9.8400

8.2 Code Structure and Preprocessing

The initial part of the Python script provided in Appendix A is dedicated to reading the raw data from Excel files and performing an automated cleaning process. This includes the handling of European decimal formats by replacing commas with dots and the conversion of object-type columns into numeric values.

Beyond simple data cleaning, the script now integrates an analytical calculation block where the user provides the number of runner blades and guide vanes. This allows the system to determine the rotational frequency (f_n) and the theoretical pressure pulsation frequency (f_p) directly from the selected rotational speed signal.

Furthermore, the preprocessing has been enhanced with a sampling optimization step: based on the identified peak frequency, the code suggests a target sampling rate and performs a decimation.

This step ensures that the input data are consistent and properly formatted but also allows to make the code as flexible as possible so that it can also be used with other types of datasets, which is essential for the reliable execution of the subsequent analytical and experimental analysis.

8.3 Analytical vs Experimental Comparison

As anticipated in chapter 6, the developed code was designed to enable a direct comparison between analytical predictions of RSI frequencies and the results obtained through Fast Fourier Transform (FFT) of the measured pressure signals.

In the first step, the analytical RSI frequency was computed by combining the shaft rotational speed with the number of runner blades and guide vanes, following the classical blade passing frequency formulation reported in [46]. This relationship can be expressed as:

$$f_{RSI} = n \cdot z_r \cdot f_f, \tag{8.1}$$

where n is the harmonic number ($n = 1, 2, \dots$), z_r is the number of rotor blades, and $f_f = N/60$ is the shaft rotational frequency in Hz, with N being the rotational speed in revolutions per minute (rpm).

To this end, the script prompts the user to provide the main turbine parameters, namely the number of runner blades, the number of guide vanes, and the column corresponding to the runner angular velocity. Based on these inputs, the analytical frequency is determined, representing the expected dominant pulsation due to the RSI. For the nodal diameter formulations detailed in the section 5.3 was used.

Table 8.4: Analytical rotor–stator interaction (RSI) frequencies and corresponding harmonics.

Harmonic number n	**Frequency [Hz]**	**Nodal Diameter**	**Description**
1	83.148	2-ND	Fundamental RSI frequency (blade passing)
2	166.296	4-ND	Second harmonic
3	249.444	6-ND	Third harmonic
4	332.592	7-ND	Fourth harmonic

Subsequently, the FFT was applied to the experimental dataset provided by NTNU. By comparing the spectral peak identified in the pressure measurements with the analytical prediction, it was possible to quantify discrepancies between theory and experiments. This procedure allowed for the assessment of the data consistency and for the identification of the operating condition BEP as the most representative case to be used for further development and training purposes.

Figure 8.3 reports an example of the results obtained from the implemented code. The upper panel shows the time series of the pressure signal measured at location VL2, while the lower panel presents the corresponding FFT spectrum. A clear spectral peak can be observed around the analytically predicted RSI frequency,

confirming the consistency between the theoretical formulation and the experimental data.

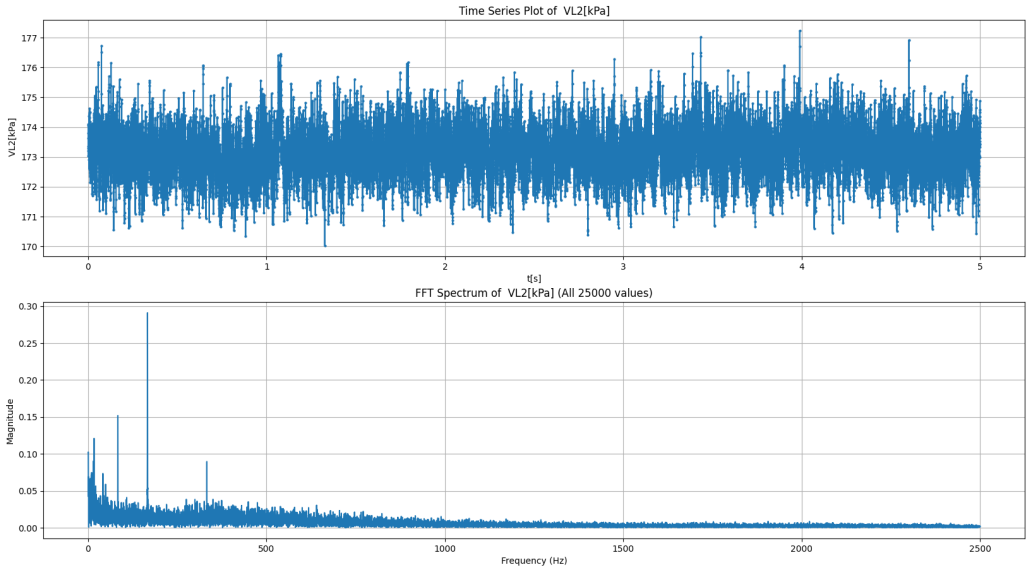

Figure 8.2: Time series and FFT spectrum of the VL2 pressure signal from the NTNU dataset.

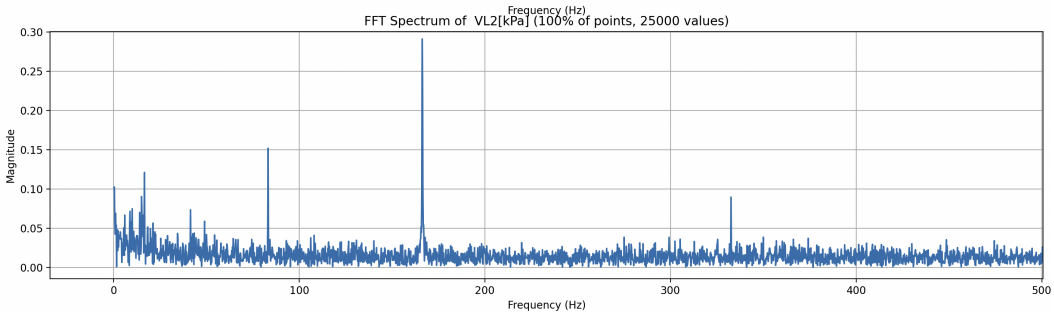

Figure 8.3: Zoom of the FFT of the VL2 pressure signal

The lower panel illustrates the FFT spectrum computed from the entire dataset (25,000 samples). The spectral content is dominated by a pronounced peak at approximately 166 Hz, which corresponds to the analytically predicted second harmonic of the rotor–stator interaction (4st ND). This indicates that the VL2 pressure sensor, located in the vaneless space, is primarily sensitive to the second blade-passing frequency. Additional peaks are visible at higher frequencies, including the fourth harmonic (around 330 Hz), although their amplitude is significantly lower. The strong correspondence between the analytical prediction and the dominant experimental peak indicates that the dataset is consistent with the analytical calculation done in the previous steps.

The same type of plots, including both the time series and the FFT spectra, are reported below for the DT5 and DT6 pressure signals.

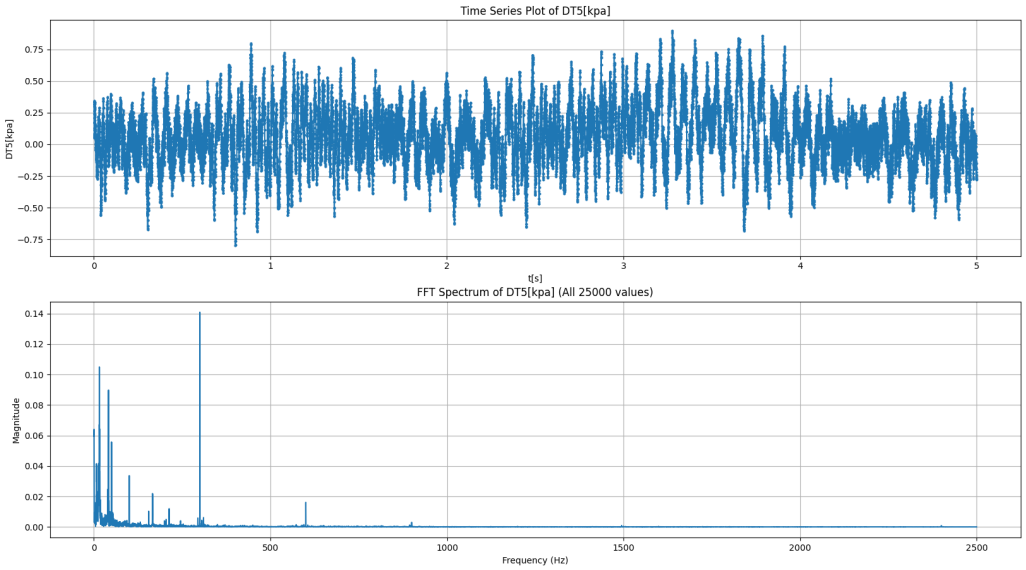

Figure 8.4: Time series and FFT spectrum of the DT5 pressure signal from the NTNU dataset.

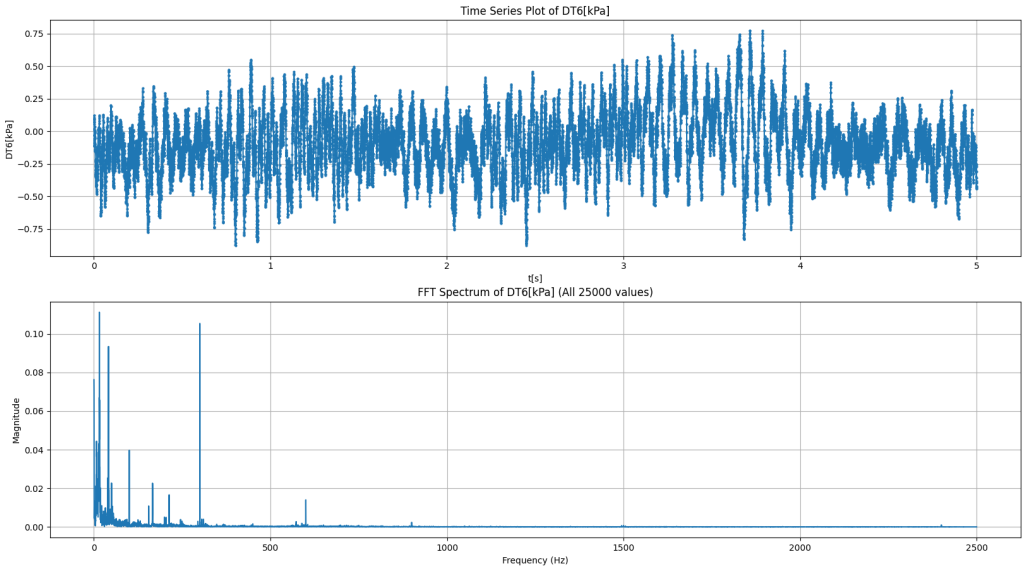

Figure 8.5: Time series and FFT spectrum of the DT6 pressure signal from the NTNU dataset.

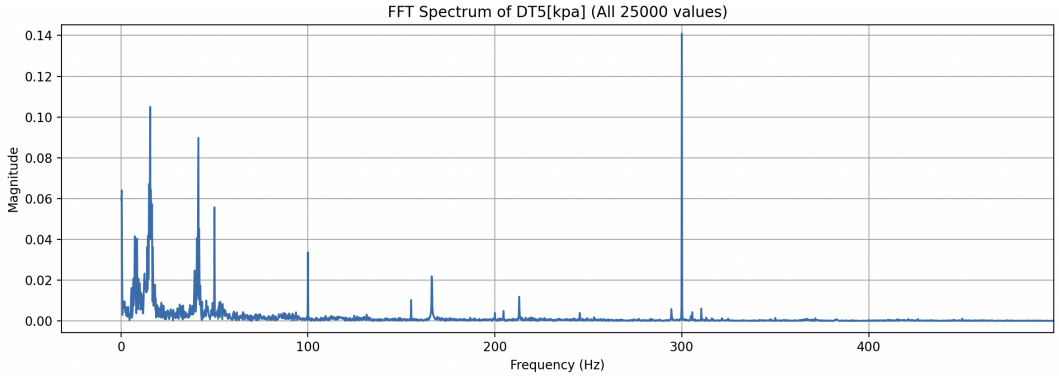

Figure 8.6: Zoom of the FFT of the DT5 pressure signal

Figure 8.4 shows the time-domain signal and the corresponding FFT spectrum of the pressure measurement at DT5. In the upper panel, the time series highlights pronounced low-frequency oscillations superimposed on the local mean pressure, reflecting the unsteady flow conditions in the draft tube cone.

The lower panel illustrates the spectral content, where the dominant peak is clearly located at approximately 330 Hz. This frequency corresponds to the fourth harmonic of the analytically predicted rotor–stator interaction frequency. The second harmonic (166 Hz, 4th ND) is also present in the spectrum, but with a considerably lower amplitude. The prevalence of the 7th ND component indicates that the DT5 sensor is primarily sensitive to a four-per-revolution modulation of the blade-passing phenomenon, which is consistent with the flow features developing in the draft tube region. Similar behavior was observed for DT6, confirming that both draft tube sensors are more strongly associated with the fourth harmonic of the RSI.

8.3.1 Extension to Part Load Conditions

The same analytical vs experimental analysis was also applied to the Part Load (PL) operating condition. Unlike the BEP, where the pressure signals are characterized by a dominant contribution at the second RSI frequency (VL2) and by a clear prevalence of the fourth harmonic in the draft tube sensors (DT5 and DT6), the PL condition exhibited a markedly different spectral behaviour.

At PL, the velocity distribution within the runner passages and the draft tube is less uniform, and the flow is strongly affected by instabilities such as vortex rope formation and enhanced turbulence levels. As a consequence, the FFT spectra of the pressure signals tend to show a broader distribution of energy, with the RSI-related peaks being less sharp and sometimes partially masked by low-frequency fluctuations. This behaviour is consistent with the literature, which reports that part-load operation of Francis turbines is often dominated by hydrodynamic instabilities that can lead to pronounced vibrations and pressure pulsations not directly linked to the fundamental RSI mechanism.

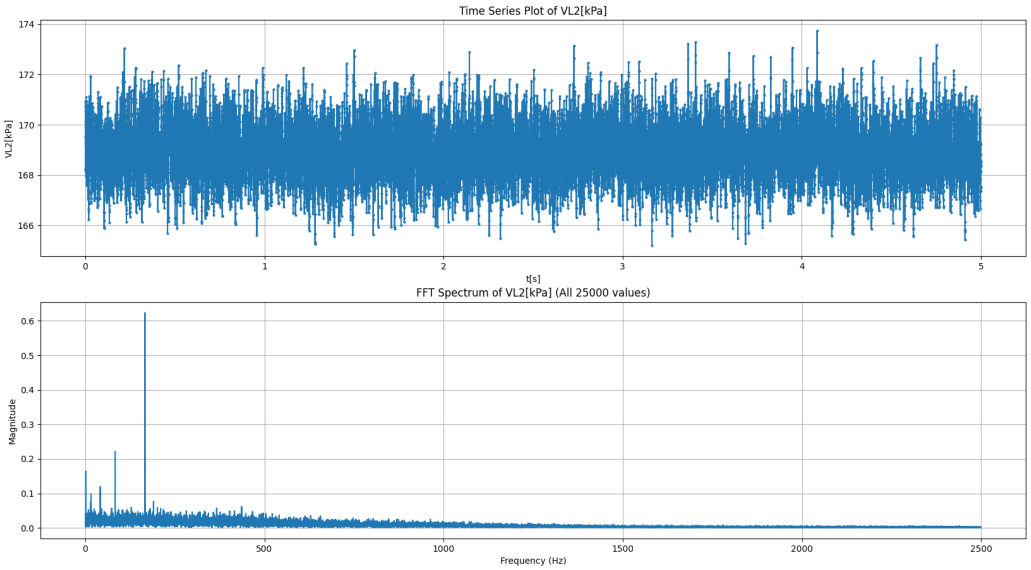

Figure 8.7: PL condition — time series and FFT spectrum of the VL2 pressure signal.

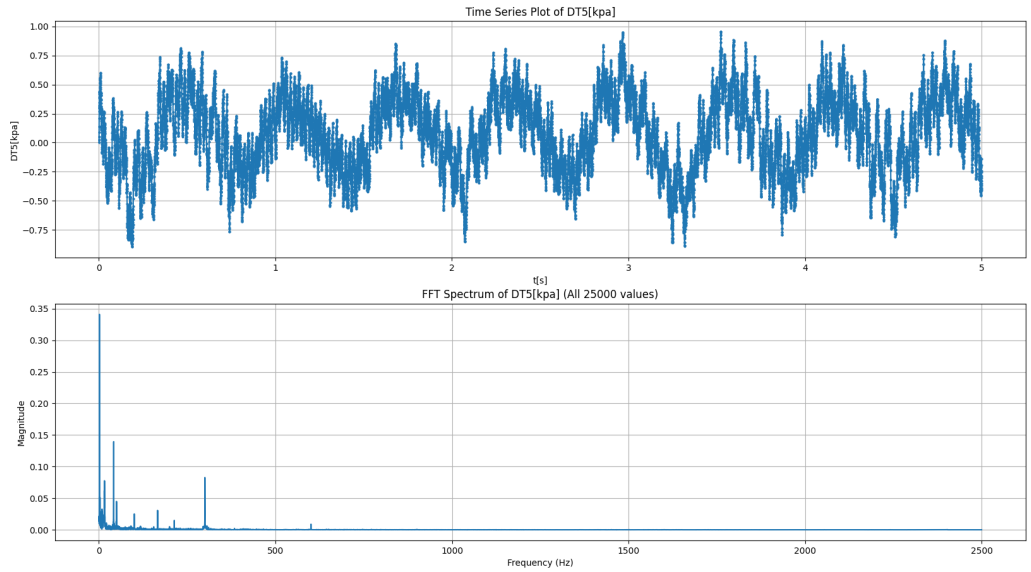

Figure 8.8: PL condition — time series and FFT spectrum of the DT5 pressure signal.

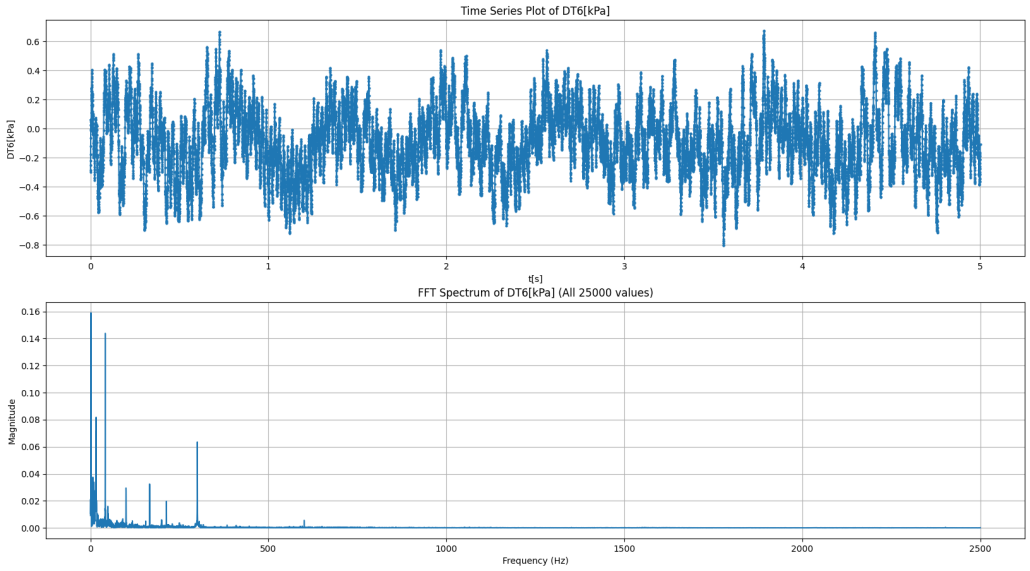

Figure 8.9: PL condition — time series and FFT spectrum of the DT6 pressure signal.

The results obtained in this work confirm these considerations. For the VL2 sensor, the FFT spectrum still displays a clear dominant peak around 165 Hz, which corresponds to the second RSI harmonic (4st ND), indicating that the second RSI frequency remains detectable at PL in the vaneless space. Conversely, the draft-tube sensors (DT5 and DT6) exhibit spectra dominated by strong low-frequency contributions below 50 Hz, which overshadow the RSI tones. These low-frequency components are consistent with the typical signature of cavitating vortex rope dynamics, whose precession frequency is known to occur in the range of 0.20–0.35 of the runner rotational frequency. Such structures generate pressure pulsations that propagate through the draft tube and can strongly affect the dynamic stability of the machine.

Although the fourth harmonic (7th ND, around 330 Hz) is still detectable at PL, it no longer constitutes the leading component as observed at BEP. Instead, the spectral energy distribution highlights the predominance of vortex-induced fluctuations in the draft tube, confirming that part-load operation is characterized by hydrodynamic instabilities rather than by the classical RSI mechanism.

Overall, the comparison between BEP and PL highlights the strong dependence of the spectral content on the operating condition: RSI-dominated at BEP, and instability-dominated at PL.

8.4 Optimization of Sampling Requirements

A further component of the developed code is devoted to the optimization of sampling requirements, with the objective of determining the minimum number of data points necessary to accurately capture the spectral content of the signals. This aspect is of practical relevance, since recording and storing very large datasets can be computationally demanding, whereas undersampling may lead to the loss of essential information. To address this, the methodology focuses on two key aspects: determining the optimal sampling frequency to accurately capture the spectral content while minimizing computational and storage costs and formatting the extracted features into a generalized, dataset suitable for the Virtual Sensor approach.

The implemented procedure operates through a physics-informed analytical step followed by an interactive validation loop. Initially, the code computes the Fast Fourier Transform (FFT) of the original high-resolution signal and identifies the dominant frequency peak (f_{max}). Based on this physical feature, the algorithm automatically calculates a recommended optimal sampling rate—typically set to five times f_{max}, ensuring a robust margin above the Nyquist-Shannon sampling limit.

At this stage, the software informs the user of the detected peak and the recommended sampling frequency, offering the immediate option to generate and save an optimized, downsampled version of the entire dataset in XLSX format.

In the second step, an interactive mode is introduced, allowing the user to manually select the percentage of data points to retain and directly compare the reduced FFT spectrum with the full-resolution reference. This functionality enables a visual validation of the automatic sampling optimization procedure and highlights the trade-off between data reduction and spectral accuracy.

More specifically, during the "Sampling Validation" phase, the code suggests an optimal data retention percentage (e.g., retaining 16% of the original samples) and prompts the user to test alternative values. For each selected percentage, the algorithm evaluates two distinct downsampling strategies:

1. A professional decimation process incorporating a low-pass anti-aliasing filter (`scipy.signal.decimate`).

2. A naive subsampling approach based on simple array slicing without prior filtering.

The resulting spectra are then plotted alongside the full-resolution reference, providing a direct visual comparison. This analysis clearly demonstrates the effectiveness of proper anti-aliasing filtering and highlights the severe spectral distortions that arise when it is neglected, thereby validating the robustness and reliability of the proposed data reduction approach.

The use of an anti-aliasing filter during the downsampling process is essential to ensure the physical consistency of the signal. When a signal is resampled at a lower frequency, frequency components above the new Nyquist limit (half of the target sampling frequency) cannot be correctly represented and are folded back into the

lower frequency range, generating aliasing. This phenomenon introduces non-physical spectral components that can severely distort the frequency content of the signal.

This filter removes all frequency components above the admissible limit, ensuring that only the information that can be correctly captured at the reduced sampling rate is retained. In the implemented workflow, this operation is automatically handled by the `scipy.signal.decimate` function, which combines low-pass filtering with subsampling in a single step.

As a result, the downsampled signal preserves the original spectral characteristics within the valid frequency range, enabling a reliable reduction of the dataset size without introducing artificial distortions.

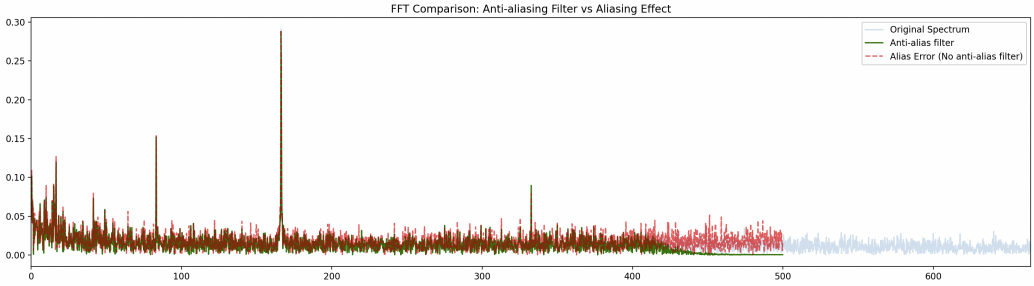

Figure 8.10: FFT spectrum comparison of the VL2 signal.

In the Figure 8.10 a comprehensive spectral comparison is presented, highlighting the critical impact of anti-aliasing filtering during data reduction. The figure is structured with the original, full-resolution FFT spectrum displayed in blue at the top. The red and green plots display the decimated signal at the same optimized target frequency. In the green plot the signal processed through an appropriate anti-aliasing filter is shown, while in red, the signal subjected to naive subsampling (array slicing) is presented.

Notably, the horizontal axis of these spectral plots is no longer expressed in absolute frequencies (Hz), but is instead normalized as multiples of the machine's fundamental rotational frequency (f_n), referred to as *Orders*. This shift from a linear frequency scale to an Order-based domain is a strategic choice for the Virtual Sensor development: it ensures that the identified spectral features, such as the Blade Passing Frequency, remain anchored to their respective physical origins regardless of the specific turbine's rotational speed. This normalization effectively decouples the signal's information from the machine's operational scale, providing a generalized and consistent input for the neural network.

The fundamental difference between proper decimation and naive subsampling is clearly demonstrated by the contrast between the green and red plots. In the green plot, the anti-aliasing filter has effectively suppressed all frequency components above the new Nyquist limit (which is half the target sampling frequency). This results in a clean, physically consistent spectrum that fully preserves the original peaks within the admissible frequency range, ensuring they retain their position and relative magnitude.

Conversely, the red plot exhibits a severe spectral distortion. Due to the absence of prior filtering, the high-frequency component that should have been removed has been "folded back" into the lower frequency range, creating a false peak. This phenomenon, known as aliasing error, introduces a non-physical artifact into the spectrum, masking real features and making the dataset unreliable for Machine Learning applications. This direct comparison visually validates the necessity of the proposed anti-aliasing pipeline, demonstrating that it is the only viable approach for generating a physically coherent and optimized dataset for the training phase of Artificial Intelligence models.

This comparison highlights the importance of incorporating an anti-aliasing filtering stage within the proposed downsampling procedure. By removing frequency components above the admissible limit, the approach ensures that the reduced dataset remains physically consistent and suitable for subsequent data-driven applications.

The analysis also indicates that the NTNU dataset, originally sampled at 5 kHz, is significantly oversampled with respect to the dominant spectral content. As a result, a substantial reduction in the number of samples can be achieved without compromising the accuracy of the relevant frequency information.

For the draft tube sensors (DT5 and DT6), the dominant spectral contribution is associated with the second harmonic (2ND, approximately 310 Hz). In this case, the Nyquist–Shannon criterion still governs the minimum sampling requirement, implying a higher threshold compared to signals dominated by the fundamental frequency. However, the original sampling frequency remains well above this limit, confirming that data reduction can be consistently applied while preserving the essential spectral characteristics of the signals.

8.5 Preparation for Machine Learning Models

The final step in the data processing pipeline was to structure the validated and optimized dataset for its potential use in machine learning applications. In particular, the goal was to ensure that the spectral features of the pressure signals could serve as a generalized and reliable input for neural network models aimed at monitoring and predicting turbine behavior across different operating scales and machines.

To this end, the following actions were undertaken:

- **Feature Extraction via Sliding Windows:** The optimized signals were segmented into temporal windows of a user-defined duration (e.g., 1.0 second). To maintain temporal continuity and increase the number of training samples, a sliding window approach with a configurable overlap (e.g., 50%) was implemented. For each window, the Fast Fourier Transform (FFT) was computed, focusing on the positive frequency range to extract the spectral intensity associated with each Order.

- **Regime-Specific Normalization Strategies:** To ensure the generalizability of the Virtual Sensor, the normalization method adapts to the turbine's operating state:
  - *Stationary Regime (Peak Scaling [0, 1]):* In steady-state conditions, where the Rotor-Stator Interaction (RSI) presents a clear and stable maximum amplitude, a **Peak Scaling** method was preferred, mapping the intensities strictly within the range $[0, 1]$. Unlike the Z-score standardization, this approach does not depend on the global variance of the dataset, thus preserving the relative ratios between different spectral peaks. By mapping the maximum observed amplitude within each window to 1, the network is trained to recognize the "reference" spectral signature for a specific operating point. This setup is particularly effective for fault diagnosis: since the model learns that the dominant RSI harmonic should reach a normalized value of 1, any future deviation, such as an amplitude drop or an unexpected surge due to mechanical degradation, will shift the feature away from this reference, allowing, for example, the system to trigger an anomaly alarm. Furthermore, restricting the input space to a bounded $[0, 1]$ range significantly accelerates the convergence speed of the training process, helping the gradient descent algorithm find the optimal weights in fewer steps.
  - *Transient Regime (Z-score Standardization):* During non-stationary events such as start-ups or shutdowns, spectral frequencies and amplitudes shift rapidly, making fixed-range scaling less effective. In these cases, **Z-score Standardization** is applied by transforming each spectral feature x according to the formula:

    $$z = \frac{x - \mu}{\sigma} \tag{8.2}$$

    where μ represents the mean amplitude and σ is the standard deviation of the frequency bin across the dataset. This process centers the data around a mean of 0 and scales it in terms of **standard deviation units**.

    The physical advantage of this approach in transient analysis is twofold:
    - **Identification of Statistical Outliers:** Rather than observing absolute values, the neural network observes how many standard deviations a peak deviates from the average behavior. This is crucial for detecting impulsive events (like water hammers) or sudden structural resonances that emerge abruptly from the background noise.
    - **Energy Independent Scaling:** During a startup, the overall energy of the signal increases drastically. The Z-score "filters out" this global trend, allowing the model to focus on the *shape* of the spectral evolution and on which specific frequencies are growing faster than others relative to their own historical variance.

By highlighting these statistical "shocks," the Z-score facilitates the detection of rapid dynamic changes that would otherwise be masked by the shifting scales of a transient operation.

- **Input Feature Vectorization and Matrix Structuring:** The final processed data is organized into a numerical matrix designed for high-performance training. In this structure, each row represents a single temporal window, providing a snapshot of the turbine's dynamic state at a specific time interval. Conversely, each column corresponds to a specific frequency bin, expressed in dimensionless Orders. The value contained at the intersection of a row and a column represents the normalized spectral amplitude at that precise Order and time. This systematic arrangement allows the neural network to treat each column as a consistent input feature, facilitating the recognition of spectral patterns across the entire dataset.

Upon completion of the processing, the software generates a report. This report provides critical metadata for the subsequent training phase, including the selected operating regime, the final matrix shape (representing the number of temporal windows versus the number of frequency bins), and the spectral resolution expressed in Orders.

Finally, the processed data is exported as a structured CSV file. Each row of this file represents a single temporal window, while the columns contain the normalized spectral amplitudes labeled by their respective Order.

Chapter 9

Application of Neural Networks to Turbine Condition Monitoring

Artificial Neural Networks (ANNs) have become increasingly relevant in the context of condition monitoring and predictive maintenance for hydraulic turbines. Their ability to model complex nonlinear relationships between input and output variables makes them well suited for detecting anomalies, identifying early-stage faults, and providing robust diagnostic indicators in systems where conventional linear models are insufficient [57, 58]. In particular, ANNs are able to handle large datasets and extract hidden patterns across multiple operating conditions, providing significant advantages over classical signal-based methods.

9.1 State of the Art

Condition monitoring in hydropower plants traditionally lean on spectral analysis of vibration and pressure signals. Approaches such as root mean square (RMS) evaluation of frequency bands and alarm thresholds are widely applied [46, 59]. These robust methods, often fail to capture subtle nonlinear interactions between operating conditions (head, guide vane opening, discharge) and the resulting dynamic response.

In recent years, the integration of data-driven models, and in particular ANNs, has been proposed to complement or replace classical alarm-band approaches [60, 61]. ANNs are capable of learning complex relationships from historical datasets, thus enabling the creation of "normal behavior models" against which deviations can be identified. Compared to regression or interpolation methods, neural networks provide better generalization, adaptability to different regimes, and robustness to noisy data.

9.2 Case Study: Zhao et al. (2020)

A detailed study on the application of ANNs to hydraulic turbines was presented by Zhao et al. [38], focusing on pump-turbines operating across an extended range of conditions. Their work compared different modeling techniques for vibration prediction, including:

- Multivariate Linear Regression (MLR);
- Locally Weighted Scatterplot Smoothing (LOWESS);
- Scattered Data Interpolation (SDI);
- Artificial Neural Networks (ANN), specifically a feed-forward Multi-Layer Perceptron (MLP).

The evaluation was performed through 10-fold cross validation, using the predicted determination coefficient (preR^2) as the main performance metric. The results showed that the ANN model achieved the highest prediction accuracy (preR^2 = 0.8445), significantly outperforming LOWESS (0.8063), SDI (0.7755) and MLR (0.4180). This confirmed the superior capacity of ANNs to capture non-linear relationships in turbine dynamics.

9.2.1 Data Preprocessing and Training

Before training, raw monitoring data underwent preprocessing steps such as validity checks, removal of outliers, and normalization of variables into the range $[-1, 1]$. The dataset, consisting of 521 valid samples, was partitioned into 80% for training, 10% for validation (to avoid overfitting via early stopping), and 10% for testing. This strategy ensured both accuracy and applicability of the trained model.

9.2.2 Network Configuration

The chosen architecture was a Multi-Layer Perceptron (MLP), consisting of an input layer, a hidden layer, and an output layer. The number of neurons was optimized by trial and error to minimize the mean squared error (MSE). For example, to predict the overall vibration level in the turbine bearing, the best performance was obtained with a single hidden layer of 8 neurons.

Training was performed with the Levenberg–Marquardt (LM) backpropagation algorithm, which balances the stability of gradient descent with the accuracy of the Gauss–Newton method. Multiple runs with different random initializations were conducted to mitigate local minima, and the configuration with the lowest MSE was selected.

9.2.3 Results and Implications

The ANN-based model successfully mapped operating parameters (head, guide vane opening, flow rate) to vibration levels across the full operating range of the turbine. This enabled the definition of a "normal behavior model," which represents the expected system response under healthy conditions. This type of model would change only in case of structural damage, making it a valuable tool for early fault detection.

Furthermore, Zhao et al. showed that vibration levels peaked at low head and partial guide vane openings (30–40%), often exceeding recommended limits for continuous operation. These findings suggest that alarm thresholds should be adapted to specific operating conditions rather than applied uniformly.

9.3 Neural Networks as Virtual Sensors

Beyond predictive modeling, neural networks can be interpreted as *virtual sensors*. By integrating signals from multiple sources simultaneously (e.g. pressure pulsations, vibration indicators, head, flow rate, and guide vane angle), ANNs can detect nonlinear combinations of variables that may indicate abnormal behavior.

This approach enhances monitoring capabilities, since abnormal operating conditions often emerge not from the variation of a single parameter, but from specific multi-variable interactions. For instance, a moderate rise in vibration might be benign when occurring alone, but combined with specific flow and guide vane conditions it may signal the onset of a dangerous instability. Neural networks are capable of identifying these subtle interactions and issuing early warnings, thereby acting as intelligent synthetic sensors [60, 59].

Chapter 10

Conclusions

The work presented in this thesis contributed to the initial design phase of an AI-based virtual sensor for reversible pump-turbines, specifically focusing on the data processing pipeline. With the overarching goal of improving the monitoring and diagnosis of unsteady hydrodynamic phenomena, the study leveraged analytical formulations and spectral analysis. By establishing a robust methodology for feature extraction and thresholding, this work provides the essential data-driven groundwork required for subsequent machine learning implementations, aiming to enhance turbine reliability, efficiency, and sustainability

10.1 Summary of the Main Contributions

A first key result lies in the validation of the dataset and the development of a general-purpose dataset processing tool. The Francis-99 benchmark dataset proved to be an invaluable resource, enabling robust analysis of turbine dynamics under different steady-state conditions (BEP, PL, HL). The implemented Python script ensured flexible preprocessing and spectral analysis of signals, allowing for consistent and reproducible results across datasets.

The analytical and experimental comparison of rotor–stator interaction (RSI) frequencies confirmed that the methodology was able to distinguish between different hydrodynamic regimes. At BEP, VL2 captured the fundamental RSI harmonic, while DT5 and DT6 highlighted the second harmonic, evidencing spatial variability. At part load, spectra revealed vortex rope phenomena at low frequencies, consistent with the literature.

The optimization of sampling requirements further strengthened the contribution of this work. Rather than relying on a fixed data reduction ratio, the developed methodology adopts a physics-informed approach based on the identification of the dominant spectral content. In particular, the maximum significant frequency is extracted from the signal through FFT analysis, and an optimal sampling rate is automatically determined to ensure a safe margin above the Nyquist–Shannon limit.

This procedure is complemented by an interactive validation step, allowing the user to assess the impact of different downsampling levels and to directly compare

the resulting spectra with the full-resolution reference. The analysis demonstrated that, when combined with proper anti-aliasing filtering, significant data reduction can be achieved while preserving the physically relevant spectral features.

These results highlight that future monitoring systems can adaptively optimize acquisition rates based on the actual signal content, reducing data storage and computational costs without compromising the reliability of the extracted information

Finally, the exploration of artificial neural networks highlighted their potential to act as virtual sensors: adaptive tools capable of simultaneously processing multiple heterogeneous signals and identifying abnormal conditions before they manifest into failures. Neural networks therefore represent a step toward the implementation of predictive maintenance and intelligent monitoring in hydropower plants.

10.2 Limitations and Challenges

Some limitations remain. The reliance on a laboratory-scale dataset does not fully capture the complexity of industrial turbines, where scaling effects, structural resonances, and environmental variability can be more pronounced. Moreover, the ANN models used were relatively simple; more advanced architectures and larger, more diverse datasets could provide even stronger predictive capabilities.

Some limitations remain. The reliance on a laboratory-scale dataset does not fully capture the complexity of industrial turbines, where scaling effects, structural resonances, and environmental variability can be more pronounced.

Furthermore, a significant constraint was the inability to validate the preprocessing pipeline and the resulting models with a dataset containing real transient operations. Although the developed computational tool is already equipped with a specific logic for transient regimes—utilizing Z-score standardization and order-based tracking—the current analysis was limited to steady-state conditions (BEP, PL, and HL) provided by the Francis-99 benchmark. Consequently, the transition between different operating points, characterized by rapidly varying loads and non-stationary hydraulic phenomena, remains a critical area for future experimental validation.

Moreover, the ANN architectures explored in this preliminary phase were relatively simple. The integration of more advanced deep learning structures, trained on larger and more diverse datasets that include startup, shutdown, and load rejection sequences, could provide even stronger predictive capabilities and enhance the robustness of the Virtual Sensor in real-world industrial scenarios.

10.3 Future Developments

Based on these findings, future research should focus on:

1. Validation on full-scale hydropower units to ensure scalability of the proposed methodology.
2. Incorporating reliable transient datasets into the training phase, encompassing startup, shutdown, and load acceptance conditions, which are essential for improving the robustness and reliability of the model.
3. Adoption of deep learning architectures (e.g., LSTMs, CNNs) to capture temporal dependencies and spatial features more effectively.
4. Deployment in real-time monitoring frameworks, with embedded code within turbine control systems to provide early-warning alerts.
5. Multi-sensor data fusion, combining pressure, vibration, and electrical measurements for more robust and comprehensive diagnostics.

10.4 Economic Impact

From an industrial perspective, the adoption of virtual sensors and intelligent monitoring systems directly aligns with the primary economic objectives of the **STOR-HY** European project: the reduction of Capital Expenditures (CAPEX) and Operational Expenditures (OPEX) for pumped storage plants.

By reducing the reliance on dense physical instrumentation, the initial costs associated with hardware purchasing, cabling, and installation (CAPEX) can be significantly lowered. Moreover, the implementation of predictive maintenance strategies minimizes unexpected plant shutdowns, extends the service life of critical components, and optimizes resource allocation, leading to a drastic reduction in ongoing maintenance costs (OPEX).

Furthermore, the specific results obtained in this thesis—such as the demonstrated possibility of reducing sampling rates without information loss—directly translate into lower computational, data-transmission, and cloud-storage requirements. This technical optimization further reduces the daily operational costs of the monitoring IT infrastructure, fully supporting the economic viability and scalability of the proposed data-driven approach within the European energy framework.

10.5 Environmental and Sustainability Implications

Hydropower is one of the most powerful renewable energy, but its sustainability depends on the long-term safety and efficiency of turbine operation. By enabling early detection of damaging instabilities and optimizing operation, the proposed methodology contributes to:

- Reducing energy losses, improving the overall efficiency of electricity generation.
- Preventing catastrophic failures, which could have severe environmental and social consequences.
- Supporting sustainable operation, by enabling turbines to operate closer to their optimal efficiency points while avoiding damaging regimes.

Thus, the integration of virtual sensors and neural networks into hydropower monitoring systems aligns with the broader goals of sustainable energy production and environmental stewardship.

10.6 Final Remarks

In conclusion, this thesis has shown that combining analytical models, signal processing, and artificial intelligence enables the development of intelligent monitoring systems for hydraulic turbines. The methodology proved effective in identifying rotor–stator interaction, detecting vortex rope instabilities, and optimizing data acquisition strategies. By opening new opportunities for predictive maintenance and cost reduction, the integration of artificial neural networks as virtual sensors directly supports the STOR-HY project's goal of extending component lifespans, thereby actively promoting the United Nations' SDG 9 (Industry, Innovation and Infrastructure) and SDG 12 (Responsible Consumption and Production).

Furthermore, by bridging traditional hydraulic analysis with modern machine learning approaches, this research contributes both to the academic understanding of turbine dynamics and to the practical advancement of hydropower monitoring technologies. With further validation on full-scale units and integration into real-time frameworks, these data-driven virtual sensors will become a cornerstone of future pumped storage plants. Ultimately, by ensuring grid reliability and economic efficiency, this methodology enables a more flexible integration of renewable sources, driving forward SDG 7 (Affordable and Clean Energy) and SDG 13 (Climate Action) in the global energy sector.

Appendix A

Python Code for Data Analysis

The following Python script was developed to process the NTNU dataset, perform the Fast Fourier Transform (FFT), and compare the results with the analytical rotor–stator interaction frequency.

Listing A.1: Full Python script for dataset analysis.

```
import pandas as pd
import matplotlib.pyplot as plt
import numpy as np
from scipy.signal import decimate
from scipy.fft import fft, fftfreq
from sklearn.preprocessing import StandardScaler
import math
import os


def prepare_ml_dataset(df, target_col, fs_original, fs_target,
    window_sec, fn, overlap=0.5, regime='stationary'):

    # 1. SAMPLING OPTIMIZATION (Downsampling with Anti-aliasing)
    decimation_factor = int(fs_original / fs_target)
    if decimation_factor < 1: decimation_factor = 1

    y_resampled = decimate(df[target_col].values, decimation_factor)
    new_fs = fs_original / decimation_factor

    # 2. OPTIMIZED SAMPLING WINDOWS
    samples_per_window = int(window_sec * new_fs)
    step = int(samples_per_window * (1 - overlap))

    if len(y_resampled) < samples_per_window:
        raise ValueError("Dataset too short for the selected window
    size.")

    fft_dataset_raw = []
    fft_dataset_processed = []

    # 3. SLIDING WINDOW LOOP
    for i in range(0, len(y_resampled) - samples_per_window, step):
```

```
32          window_data = y_resampled[i : i + samples_per_window]
33
34          # Local detrending (subtracting mean)
35          window_data = window_data - np.mean(window_data)
36
37          # 4. SPECTRAL TRANSFORMATION (FFT)
38          yf = fft(window_data)
39          amplitudes = 2.0/samples_per_window * np.abs(yf[:
    samples_per_window//2])
40
41          fft_dataset_raw.append(amplitudes.copy())
42
43          # --- REGIME-BASED PREPROCESSING (Inside the window loop) ---
44          if regime == 'stationary':
45              # Peak Scaling (0-1) for stable, sharp peaks
46              max_amp = np.max(amplitudes)
47              if max_amp > 0:
48                  amplitudes_scaled = amplitudes / max_amp
49              else:
50                  amplitudes_scaled = amplitudes
51              fft_dataset_processed.append(amplitudes_scaled)
52
53          elif regime == 'transient':
54
55              fft_dataset_processed.append(amplitudes)
56
57      fft_array_raw = np.array(fft_dataset_raw)
58      fft_matrix_processed = np.array(fft_dataset_processed)
59
60      # --- REGIME-BASED PREPROCESSING (Matrix level) ---
61      if regime == 'stationary':
62          # Matrix is already normalized 0-1 window by window
63          fft_final = fft_matrix_processed
64      elif regime == 'transient':
65          # Apply Z-score standardization across the whole dataset (
    column-wise)
66          scaler = StandardScaler()
67          fft_final = scaler.fit_transform(fft_matrix_processed)
68
69      # 6. FREQUENCY TO ORDERS CONVERSION
70      xf = fftfreq(samples_per_window, 1/new_fs)[:samples_per_window//2]
71      safe_fn = fn if fn > 0 else 1.0
72      x_orders = xf / safe_fn
73
74      return fft_final, x_orders, fft_array_raw
75
76  def plot_ai_comparison(x_orders, original_fft_matrix,
    normalized_fft_matrix, col_name, regime):
77      """
78      Plots the comparison between raw FFT amplitudes and fully
    normalized FFT for AI.
79      """
80      fig, (ax1, ax2) = plt.subplots(2, 1, figsize=(12, 10))
```

```
81
82      mean_raw = np.mean(original_fft_matrix, axis=0)
83      mean_norm = np.mean(normalized_fft_matrix, axis=0)
84
85      ax1.plot(x_orders, mean_raw, color='blue')
86      ax1.set_title(f'Mean Raw FFT Spectrum - {col_name}')
87      ax1.set_ylabel('Absolute Amplitude')
88      ax1.set_xlabel('Orders (Multiples of Rotational Frequency)')
89      ax1.grid(True)
90
91      ax2.plot(x_orders, mean_norm, color='orange')
92      if regime == 'stationary':
93          ax2.set_title(f'Peak Scaling (0-1) Standardizationfor
        Stationary Regime - {col_name}')
94          ax2.set_ylabel('Normalized Intensity (0 - 1)')
95      else:
96          ax2.set_title(f'Z-Score Standardization for Transient Regime -
        {col_name}')
97          ax2.set_ylabel('Standardized Intensity (Z-Score)')
98
99      ax2.set_xlabel('Orders (Multiples of Rotational Frequency)')
100     ax2.grid(True)
101
102     plt.tight_layout()
103     plt.show()
104
105 def save_optimized_xlsx(df, time_col, target_fs, original_fs, file_path
        ):
106     q = int(original_fs / target_fs)
107     if q <= 1:
108         print("\n[Optimization] Target frequency is too high. No
        reduction needed.")
109         return
110     print(f"\n[Optimization] Reducing frequency from {original_fs:.1f}
        Hz to {original_fs/q:.1f}Hz")
111     optimized_data = {}
112     optimized_data[time_col] = df[time_col].values[::q]
113     for col in df.columns:
114         if col == time_col:
115             continue
116         try:
117             optimized_data[col] = decimate(df[col].values, q)
118         except Exception as e:
119             optimized_data[col] = df[col].values[::q]
120     min_len = min(len(v) for v in optimized_data.values())
121     opt_df = pd.DataFrame({k: v[:min_len] for k, v in optimized_data.
        items()})
122     base, _ = os.path.splitext(file_path)
123     new_filename = f"{base}_optimized_{int(original_fs/q)}Hz.xlsx"
124     try:
125         opt_df.to_excel(new_filename, index=False, engine='openpyxl')
126         print(f"Optimized Excel file saved: {new_filename}")
127         print(f"Rows reduced: {len(df)} -> {len(opt_df)}")
```

```
    except Exception as e:
        print(f" Error saving Excel file: {e}")

# --- MAIN EXECUTION ---

file_path = input('Enter the path to the XLSX file: ')

try:
    df = pd.read_excel(file_path)
    for col in df.columns:
        if df[col].dtype == object:
            df[col] = df[col].astype(str).str.replace(',', '.')

    print('Column names:')
    print(list(df.columns))

    fn = 1.0

    try:
        runner_blades = int(input('Enter the number of runner blades: '
    ))
        guide_vanes = int(input('Enter the number of guide vanes (
    stator blades): '))

        print('\nAvailable columns for rotational speed:')
        for i, col in enumerate(df.columns):
            print(f'{i}: {col}')
        omega_col_idx = int(input('Enter the column number containing
    rotational speed (omega in rad/s): '))
        omega_col_name = df.columns[omega_col_idx]
        omega_value = pd.to_numeric(df[omega_col_name], errors='coerce'
    ).dropna().iloc[0]
        fn = omega_value / (2 * np.pi)

        print(f'Rotational speed (omega): {omega_value:.4f} rad/s')
        print(f'Rotational frequency (fn): {fn:.4f} Hz')

        n_input = input('Enter the harmonic number n (press Enter for n
    =1): ')
        n = int(n_input) if n_input.strip() else 1
        fp = n * runner_blades * fn
        print(f'Analytical pressure pulsation frequency: fp = {fp:.4f}
    Hz')
    except Exception as e:
        print(f'Could not compute analytical frequency: {e}')

    fs = float(input('Enter the sampling frequency (Hz): '))

    while True:
        print('\nAvailable columns:')
        for i, col in enumerate(df.columns):
            print(f'{i}: {col}')

```

```
175         col_input = input('\nEnter the column number to plot (or type "
    exit" to quit): ')
176         if col_input.lower() == 'exit':
177             break
178 
179         if col_input.isdigit():
180             col_idx = int(col_input)
181             if 0 <= col_idx < len(df.columns):
182                 col_name = df.columns[col_idx]
183                 df[col_name] = pd.to_numeric(df[col_name], errors='
    coerce')
184 
185                 clean_data = df[col_name].dropna()
186                 time_col = df.columns[0]
187                 time_data = pd.to_numeric(df[time_col], errors='coerce'
    ).dropna()
188 
189                 if len(clean_data) > 0 and len(time_data) > 1:
190                     fft_data = clean_data
191                     N = len(fft_data)
192                     fft_result = np.fft.fft(fft_data.values)
193                     freqs = np.fft.fftfreq(N, 1/fs)
194 
195                     positive_freq_indices = freqs > 0
196                     positive_freqs = freqs[positive_freq_indices]
197                     magnitude = 2/N * np.abs(fft_result[
    positive_freq_indices])
198 
199                     fig, (ax1, ax2) = plt.subplots(2, 1, figsize=(12,
    10))
200                     ax1.plot(time_data, clean_data, marker='o',
    linestyle='-', markersize=2)
201                     ax1.set_title(f'Time Series Plot of {col_name}')
202                     ax1.grid(True)
203 
204                     ax2.plot(positive_freqs, magnitude)
205                     ax2.set_title(f'FFT Spectrum of {col_name} (
    Original)')
206                     ax2.grid(True)
207                     plt.tight_layout()
208                     plt.show()
209 
210                     peak_idx = np.argmax(magnitude)
211                     peak_freq = positive_freqs[peak_idx]
212                     peak_mag = magnitude[peak_idx]
213                     fmax = peak_freq
214 
215                     print(f'\nFFT Analysis for {col_name}: Peak at {
    fmax:.6f} Hz')
216 
217                     print(f"\nRecommendation: Significant content found
     at {fmax:.2f} Hz.")
218                     opt_choice = input("Generate optimized Xlsx for
```

```
    this dataset? (yes/no): ").strip().lower()
219                 final_target = fs
220                 if opt_choice in ['yes', 'y']:
221                     suggested_fs = fmax * 5
222                     target_input = input(f"Target sampling Hz [
    Default {suggested_fs:.0f}]: ").strip()
223                     final_target = float(target_input) if
    target_input else suggested_fs
224                     save_optimized_xlsx(df, time_col, final_target,
     fs, file_path)
225
226                 suggested_percentage = min(100, int(((fmax * 5) /
    fs) * 100))
227                 print(f"\n--- Sampling Validation for Virtual
    Sensor ---")
228                 print(f"Recommended Sampling: {fmax*5:.0f} Hz (~{
    suggested_percentage}%)")
229
230                 while True:
231                     perc_input = input(f'\nEnter percentage to test
     (Recommended: {suggested_percentage}% or "done" to stop): ').strip
    ()
232
233                     if perc_input.lower() == 'done':
234                         break
235
236                     perc = suggested_percentage if not perc_input
    else int(perc_input)
237
238                     if 1 <= perc <= 100:
239                         q = int(100 / perc)
240
241                         y_opt = decimate(fft_data.values, q)
242                         y_alias = fft_data.values[::q]
243                         t_opt = time_data.values[::q]
244
245                         N_opt = len(y_opt)
246                         fft_opt_filtered = np.fft.fft(y_opt)
247                         fft_opt_alias = np.fft.fft(y_alias)
248
249                         freq_opt = np.fft.fftfreq(N_opt, 1/(fs/q))
250                         pos_idx_opt = freq_opt > 0
251
252                         mag_opt = 2/N_opt * np.abs(fft_opt_filtered
    [pos_idx_opt])
253                         mag_alias = 2/N_opt * np.abs(fft_opt_alias[
    pos_idx_opt])
254
255                         fig, (ax_time, ax_freq) = plt.subplots(2,
    1, figsize=(12, 10))
256
257                         limit = 500
258                         ax_time.plot(time_data.values[:limit],
```

```
    fft_data.values[:limit], alpha=0.3, label='Original (5kHz)')
259                         ax_time.plot(t_opt[:limit//q], y_opt[:limit
    //q], 'g', label='Optimized (Filtered)')
260                         ax_time.set_title("Time Domain: Signal
    Integrity (Zoomed View)")
261                         ax_time.legend()
262
263                         ax_freq.plot(positive_freqs, magnitude,
    alpha=0.2, label='Original Spectrum')
264                         ax_freq.plot(freq_opt[pos_idx_opt], mag_opt
    , 'g', label='Anti-alias filter')
265                         ax_freq.plot(freq_opt[pos_idx_opt],
    mag_alias, 'r--', alpha=0.6, label='Alias Error (No anti-alias
    filter)')
266
267                         ax_freq.set_xlim(0, fmax * 4)
268                         ax_freq.set_title("FFT Comparison: Anti-
    aliasing Filter vs Aliasing Effect")
269                         ax_freq.legend()
270
271                         plt.tight_layout()
272                         plt.show()
273
274                         ai_choice = input("\nGenerate a normalized
    dataset for AI? (yes/no): ").strip().lower()
275                         if ai_choice in ['yes', 'y']:
276                             try:
277                                 # --- NEW SECTION: REGIME SELECTION
     ---
278                                 print("\nSelect the physical regime
     of the turbine for this dataset:")
279                                 print("1: Stationary (Constant
    speed/load -> uses Peak Scaling 0-1)")
280                                 print("2: Transient (Start-up,
    shutdown, varying load -> uses Z-Score)")
281                                 regime_choice = input("Enter 1 or 2
     [Default 1]: ").strip()
282
283                                 regime_type = 'transient' if
    regime_choice == '2' else 'stationary'
284
285                                 window_input = input("Enter window
    size in seconds [Default 1.0]: ").strip()
286                                 window_sec = float(window_input) if
     window_input else 1.0
287
288                                 overlap_input = input("Enter
    overlap percentage (0 to 99) [Default 50]: ").strip()
289                                 overlap_val = float(overlap_input)
    / 100.0 if overlap_input else 0.5
290
291                                 print(f"Processing {col_name} in {
    regime_type.upper()} regime for AI readiness...")
```

```
292
293                                     ml_ready_data, x_orders_ai,
    raw_fft_matrix = prepare_ml_dataset(
294                                         df, col_name, fs, final_target,
     window_sec, fn, overlap=overlap_val, regime=regime_type
295                                     )
296
297                                     print(f"\n--- AI Readiness Report
    ---")
298                                     print(f"Regime: {regime_type.
    capitalize()}")
299                                     print(f"Matrix Shape: {
    ml_ready_data.shape} (Windows x Frequency Bins)")
300                                     print(f"Order Resolution: {
    x_orders_ai[1] - x_orders_ai[0]:.4f} Orders")
301
302                                     plot_ai_comparison(x_orders_ai,
    raw_fft_matrix, ml_ready_data, col_name, regime_type)
303
304                                     save_name = f"{col_name}
    _ai_dataset_{regime_type}_{int(final_target)}Hz.csv"
305                                     header_cols = [f"Order_{order:.3f}"
     for order in x_orders_ai]
306                                     pd.DataFrame(ml_ready_data, columns
    =header_cols).to_csv(save_name, index=False)
307                                     print(f"AI dataset saved as: {
    save_name}")
308
309                                 except Exception as e:
310                                     print(f"Error preparing AI dataset:
     {e}")
311
312                             break
313                         else:
314                             print("Please enter a valid percentage.")
315             else:
316                 print('Invalid column number. Try again.')
317
318 except Exception as e:
319     print(f'Error: {e}')
```

Bibliography

[1] Tze-Zhang Ang, Mohamed Salem, Mohamad Kamarol, Himadry Shekhar Das, Mohammad Alhuyi Nazari, and Natarajan Prabaharan. "A comprehensive study of renewable energy sources: Classifications, challenges and suggestions". In: *Energy Strategy Reviews* 43 (2022), p. 100939. ISSN: 2211-467X. DOI: 10.1016/j.esr.2022.100939. URL: https://www.sciencedirect.com/science/article/pii/S2211467X2200133X (cit. on pp. 1, 5).

[2] Giovanna Cavazzini, Jean-Bernard Houdeline, Giorgio Pavesi, Olivier Teller, and Guido Ardizzon. "Unstable behaviour of pump-turbines and its effects on power regulation capacity of pumped-hydro energy storage plants". In: *Renewable and Sustainable Energy Reviews* 94 (2018), pp. 399–409. ISSN: 1364-0321. DOI: 10.1016/j.rser.2018.06.018. URL: https://www.sciencedirect.com/science/article/pii/S1364032118304532 (cit. on p. 2).

[3] Ånund Killingtveit. "Hydroelectric Power". In: *Future Energy*. Ed. by Trevor M. Letcher. Trondheim, Norway: Elsevier, 2020. Chap. 15, pp. 315–329. DOI: 10.1016/B978-0-08-102886-5.00015-3 (cit. on p. 2).

[4] Patrick Hendrick. "Introduction to Hydro Energy Storage". In: *Reference Module in Earth Systems and Environmental Sciences*. Elsevier Inc., Jan. 2021. ISBN: 9780124095489. DOI: 10.1016/B978-0-12-819723-3.00158-X (cit. on p. 2).

[5] W.P.T. Office. *Pumped-Storage Hydropower*. https://www.energy.gov/eere/water/pumped-storage-hydropower. Office of Energy Efficiency & Renewable Energy. Accessed: 13 June 2021. 2000 (cit. on p. 2).

[6] Ran Tao, Xijie Song, and Changliang Ye. "Pumped Storage Technology, Reversible Pump Turbines and Their Importance in Power Grids". In: *Water* 14 (Nov. 2022), p. 3569. DOI: 10.3390/w14213569 (cit. on pp. 3, 30, 31).

[7] Zhengye Liu. "Development and application of pumped storage power generation system". In: *E3S Web of Conferences* 606 (Jan. 2025), pp. 1–4. DOI: 10.1051/e3sconf/202560602003 (cit. on p. 3).

[8] U.S. Department of Energy. *Pumped Storage Hydropower*. Accessed: 2025-05-06. 2025. URL: https://www.energy.gov/eere/water/pumped-storage-hydropower (cit. on p. 3).

[9] Oliver Paish. "Small hydro power: technology and current status". In: *Renewable and Sustainable Energy Reviews* 6.6 (2002), pp. 537–556. ISSN: 1364-0321. DOI: 10.1016/S1364-0321(02)00006-0. URL: https://www.sciencedirect.com/science/article/pii/S1364032102000060 (cit. on pp. 3, 14).

[10] Olayinka S. Ohunakin, Sunday J. Ojolo, and Oluseyi O. Ajayi. "Small hydropower (SHP) development in Nigeria: An assessment". In: *Renewable and Sustainable Energy Reviews* 15.4 (2011), pp. 2006–2013. ISSN: 1364-0321. DOI: 10.1016/j.rser.2011.01.003. URL: https://www.sciencedirect.com/science/article/pii/S1364032111000049 (cit. on p. 4).

[11] Shamsul Sarip, Khairul Kamarudin, Khamarrul Razak, Rozaimi Che Hasan, Mohamad Hassan, Mohamed Suhot, Fitri Yakub, Mohd Yusof, and Mohd Yusof Md Daud. "The Potential of Micro-Hydropower Plant for Orang Asli Community in Royal Belum State Park, Perak, Malaysia". In: *Conference Proceedings*. May 2016 (cit. on p. 4).

[12] M. Mahmoud, K. Dutton, and M. Denman. "Dynamical modelling and simulation of a cascaded reserevoirs hydropower plant". In: *Electric Power Systems Research* 70.2 (2004), pp. 129–139. ISSN: 0378-7796. DOI: 10.1016/j.epsr.2003.12.001. URL: https://www.sciencedirect.com/science/article/pii/S0378779603002992 (cit. on p. 4).

[13] M.J. Khan, G. Bhuyan, M.T. Iqbal, and J.E. Quaicoe. "Hydrokinetic energy conversion systems and assessment of horizontal and vertical axis turbines for river and tidal applications: A technology status review". In: *Applied Energy* 86.10 (2009), pp. 1823–1835. ISSN: 0306-2619. DOI: 10.1016/j.apenergy.2009.02.017. URL: https://www.sciencedirect.com/science/article/pii/S0306261909000713 (cit. on p. 5).

[14] Mechanical Booster. *Francis Turbine: Main Components, Working, Advantages and Disadvantages*. Accessed: 2025-08-20. 2018. URL: https://mechanicalbooster.com/2018/01/francis-turbine.html (cit. on pp. 7, 22, 23, 38).

[15] Roger E. A. Arndt. "Fundamentals of Hydraulic Turbine Design". In: *Renewable Energy Review Journal* 3.2 (Dec. 1981), pp. 25– (cit. on pp. 7, 9, 11, 18, 19, 25).

[16] Miroslav Nechleba. *Hydraulic Turbines: Their Design and Equipment*. Translated from the Czech edition by Charles Mayer and A. G. Evans. Prague, Czechoslovakia: ARTIA, 1957 (cit. on pp. 7, 9, 14, 18, 19).

[17] Egidio Garuffa. *Macchine motrici ed operatrici a fluido*. Seconda edizione completamente riformata. Volume I, con 1036 figure intercalate nel testo. Milano, Italia: Ulrico Hoepli, Editore-Libraio della Real Casa, 1897 (cit. on pp. 7, 14, 18, 19).

[18] A. Dadone. *Macchine idrauliche*. Torino, Italia: CLUT Editrice, 1987, p. 180. ISBN: 8879920502, 9788879920506 (cit. on pp. 9, 11, 24–26, 29).

[19] Zhiwei Guo, Sailesh Chitrakar, Zhongdong Qian, and Bhola Thapa. *Design of Francis Turbine and OpenFOAM Methods*. 1st ed. Springer Singapore, 2024, pp. VIII, 123. ISBN: 978-981-99-8381-0. DOI: 10.1007/978-981-99-8381-0. URL: https://doi.org/10.1007/978-981-99-8381-0 (cit. on pp. 9, 21–23, 50).

[20] Hermann-Josef Wagner and Jyotirmay Mathur. *Introduction to Hydro Energy Systems. Basics, Technology and Operation*. Green Energy and Technology. Springer Berlin, Heidelberg, 2011, pp. X, 130. ISBN: 978-3-642-20709-9. DOI: 10.1007/978-3-642-20709-9. URL: https://doi.org/10.1007/978-3-642-20709-9 (cit. on pp. 11–15, 18, 19, 21, 24).

[21] S.L. Dixon and C.A. Hall. "Chapter 9 - Hydraulic Turbines". In: *Fluid Mechanics and Thermodynamics of Turbomachinery (Sixth Edition)*. Ed. by S.L. Dixon and C.A. Hall. Sixth Edition. Boston: Butterworth-Heinemann, 2010, pp. 303–355. ISBN: 978-1-85617-793-1. DOI: https://doi.org/10.1016/B978-1-85617-793-1.00009-2. URL: https://www.sciencedirect.com/science/article/pii/B9781856177931000092 (cit. on pp. 15, 25, 30).

[22] Deniz Sarper Semerci and Tahir Yavuz. "CFD-Based Performance Analyses of a Francis Turbine in Several Guide Vane Positions". In: *Proceedings of the International Conference on Advanced Technologies (ICAT)*. Konya, Turkey: The Scientific & Technological Research Council of Turkey, Dec. 2020. URL: https://www.researchgate.net/publication/346628318_CFD-Based_Performance_Analyses_of_a_Francis_Turbine_in_Several_Guide_Vane_Positions (cit. on p. 16).

[23] Mechanical Technology. *Impulse Turbine*. Accessed: 2025-08-08. 2014. URL: https://4mechtech.blogspot.com/2014/06/impulse-turbine.html (cit. on p. 18).

[24] Author Unknown. *homework-help*. Homework problem. URL: https://www.chegg.com/homework-help/questions-and-answers/pump-turbine-system-draws-water-upper-reservoir-daytime-produce-power-city-night-pumps-wat-q15015451 (cit. on p. 27).

[25] Xiuli Mao, Jiaren Hu, Zhongyong Pan, Pengju Zhong, and Ning Zhang. "A Brief Review of Recent Research on Reversible Francis Pump Turbines in Pumped Storage Plants". In: *Energies* 18.2 (2025), p. 394. ISSN: 1996-1073. DOI: 10.3390/en18020394. URL: https://www.mdpi.com/1996-1073/18/2/394 (cit. on pp. 29–31, 33, 34, 37, 38).

[26] S.H. Ahn, X. Zhou, L. He, Y. Luo, and Z. Wang. "Numerical estimation of prototype hydraulic efficiency in a low head power station based on gross head conditions". In: *Renewable Energy* 153 (2020), pp. 175–181 (cit. on pp. 30, 31).

[27] Chirag Trivedi, Bhupendra Gandhi, and Michel J. Cervantes. "Effect of transients on Francis turbine runner life: a review". In: *Journal of Hydraulic Research* 51.2 (2013), pp. 121–132. DOI: 10.1080/00221686.2012.732971.

URL: http://dx.doi.org/10.1080/00221686.2012.732971 (cit. on pp. 32, 33).

[28] Georgi Todorov, Ivan Kralov, Konstantin Kamberov, Yavor Sofronov, and Blagovest Zlatev. "Failure Mechanisms of Stay Vanes in a Pumped Hydroelectric Energy Storage Francis Turbine Unit". In: *13th International Scientific Conference TECHSYS 2024 – Engineering, Technologies and Systems*. Vol. 3274. AIP Conference Proceedings. AIP Publishing, 2024, pp. 050001-1–050001-11. DOI: 10.1063/5.0258647 (cit. on pp. 33, 35–37).

[29] Zhigang Zuo, Shuhong Liu, Yuekun Sun, and Yulin Wu. "Pressure fluctuations in the vaneless space of High-head pump-turbines,A review". In: *Renewable and Sustainable Energy Reviews* 41 (Jan. 2015), pp. 965–974. DOI: 10.1016/j.rser.2014.09.011 (cit. on pp. 33, 34, 42).

[30] Alfredo Guardo, Alfred Fontanals, Mònica Egusquiza, Carme Valero, and Eduard Egusquiza. "Characterization of the Effects of Ingested Bodies on the Rotor–Stator Interaction of Hydraulic Turbines". In: *Energies* 14.20 (2021), p. 6669. ISSN: 1996-1073. DOI: 10.3390/en14206669. URL: https://www.mdpi.com/1996-1073/14/20/6669 (cit. on pp. 37, 40).

[31] Eduard Egusquiza, Carme Valero, Aida Estévez, Alfredo Guardo, and Miguel Coussirat. "Failures due to ingested bodies in hydraulic turbines". In: *Engineering Failure Analysis* 18.1 (2011), pp. 464–473. ISSN: 1350-6307. DOI: 10.1016/j.engfailanal.2010.09.039. URL: https://www.sciencedirect.com/science/article/pii/S1350630710001913 (cit. on p. 38).

[32] Chirag Trivedi, Igor Iliev, Ole Gunnar Dahlhaug, Zoran Markov, Fredrik Engstrom, and Henning Lysaker. "Investigation of a Francis turbine during speed variation: Inception of cavitation". In: *Renewable Energy* 166 (2020), pp. 147–162. ISSN: 0960-1481. DOI: 10.1016/j.renene.2020.11.108. URL: https://www.sciencedirect.com/science/article/pii/S0960148120318607 (cit. on pp. 38, 39).

[33] Xin Liu, Yongyao Luo, Alexandre Presas, Zhengwei Wang, and Lingjiu Zhou. "Cavitation Effects on the Structural Resonance of Hydraulic Turbines: Failure Analysis in a Real Francis Turbine Runner". In: *Energies* 11.9 (2018), p. 2320. ISSN: 1996-1073. DOI: 10.3390/en11092320. URL: https://www.mdpi.com/1996-1073/11/9/2320 (cit. on pp. 38, 39).

[34] Keita Yamamoto, Andres Müller, Arthur Favrel, Christian Landry, and François Avellan. "Numerical and experimental evidence of the inter-blade cavitation vortex development at deep part load operation of a Francis turbine". In: *IOP Conference Series: Earth and Environmental Science* 49.8 (2016), p. 082005. DOI: 10.1088/1755-1315/49/8/082005 (cit. on pp. 38–40).

[35] Xavier Escaler, Mohamed Farhat, Eduard Egusquiza, and François Avellan. "Dynamics and Intensity of Erosive Partial Cavitation". In: *Journal of Fluids*

Engineering 129.7 (2007), pp. 886–893. DOI: 10.1115/1.2742748 (cit. on pp. 38–40).

[36] Keita Yamamoto, Arthur Favrel, Andres Müller, Christian Landry, and François Avellan. "Onboard measurements of inter-blade cavitation vortex development at deep part load operation of a Francis turbine". In: *Experiments in Fluids* 58.12 (2017), p. 165. DOI: 10.1007/s00348-017-2421-z (cit. on pp. 38, 40).

[37] Cristian Rodriguez, Eduard Egusquiza, and Borja Mateos-Prieto. "Monitoring of Rotor-Stator Interaction in Pump-Turbine Using Vibrations Measured with On-Board Sensors Rotating with Shaft". In: *Shock and Vibration* 2014 (Feb. 2014). DOI: 10.1155/2014/276796 (cit. on pp. 39, 43, 49).

[38] Weiqiang Zhao, Mónica Egusquiza, Carme Valero, David Valentín, Alexandre Presas, and Eduard Egusquiza. "On the use of artificial neural networks for condition monitoring of pump-turbines with extended operation". In: *Measurement* 163 (2020), p. 107952. ISSN: 0263-2241. DOI: https://doi.org/10.1016/j.measurement.2020.107952. URL: https://www.sciencedirect.com/science/article/pii/S0263224120304905 (cit. on pp. 40, 41, 43, 74).

[39] J. O. Kverno, I. Iliev, and O. G. Dahlhaug. "High flexibility in Francis turbine operation and design philosophy: A review". In: *IOP Conference Series: Earth and Environmental Science*. Vol. 1037. 1. IOP Publishing, June 2022, p. 012011. DOI: 10.1088/1755-1315/1037/1/012011. URL: https://doi.org/10.1088/1755-1315/1037/1/012011 (cit. on p. 41).

[40] David Valentin, Alexandre Presas, Monica Egusquiza, Carme Valero, and Eduard Egusquiza. "Transmission of High Frequency Vibrations in Rotating Systems. Application to Cavitation Detection in Hydraulic Turbines". In: *Applied Sciences* 8.3 (2018), p. 451. ISSN: 2076-3417. DOI: 10.3390/app8030451. URL: https://www.mdpi.com/2076-3417/8/3/451 (cit. on p. 41).

[41] Weiqiang Zhao, Alexandre Presas, Monica Egusquiza, David Valentin, Eduard Egusquiza, and Carme Valero. "Increasing the operating range and energy production in Francis turbines by an early detection of the overload instability". In: *Measurement* 181 (2021), p. 109580. ISSN: 0263-2241. DOI: 10.1016/j.measurement.2021.109580. URL: https://www.sciencedirect.com/science/article/pii/S0263224121005558 (cit. on p. 41).

[42] Chirag Trivedi. "A Systematic Validation of a Francis Turbine Under Design and Off-Design Loads". In: *Journal of Verification, Validation and Uncertainty Quantification* 4.1 (June 2019), p. 011003. ISSN: 2377-2158. DOI: 10.1115/1.4043965. URL: https://doi.org/10.1115/1.4043965 (cit. on p. 41).

[43] Bhushan R. Rode and Arun Kumar. "Unstable Pressure Fluctuations in the Vaneless Space of High-Head Reversible Pump-Turbines: A Systematic Review". In: *Journal of Energy Storage* 72 (2023), p. 108397. ISSN: 2352-152X. DOI: 10.1016/j.est.2023.108397. URL: https://www.sciencedirect.com/science/article/pii/S2352152X23017942 (cit. on p. 42).

[44] Deyou Li, R.Z. Gong, Hongjie Wang, Xianzhu Wei, Z.S. Liu, and D.Q. Qin. "Analysis of Rotor-Stator Interaction in Turbine Mode of a Pump-Turbine Model". In: *Journal of Applied Fluid Mechanics* 9 (July 2016), pp. 2559–2568. DOI: 10.18869/acadpub.jafm.68.236.25086 (cit. on p. 43).

[45] C. G. Rodriguez, E. Egusquiza, and I. F. Santos. "Frequencies in the Vibration Induced by the Rotor Stator Interaction in a Centrifugal Pump Turbine". In: *Journal of Fluids Engineering* 129.11 (May 2007), pp. 1428–1435. ISSN: 0098-2202. DOI: 10.1115/1.2786489. URL: https://doi.org/10.1115/1.2786489 (cit. on pp. 43, 47, 48).

[46] Eduard Egusquiza, Carme Valero, Xingxing Huang, Esteve Jou, Alfredo Guardo, and Cristian Rodriguez. "Failure investigation of a large pump-turbine runner". In: *Engineering Failure Analysis* 23 (2012), pp. 27–34. ISSN: 1350-6307. DOI: 10.1016/j.engfailanal.2012.01.012. URL: https://www.sciencedirect.com/science/article/pii/S1350630712000210 (cit. on pp. 43, 48–50, 62, 73).

[47] Eduard Egusquiza, Carme Valero, Alex Presas, Xingxing Huang, Alfredo Guardo, and Ulrich Seidel. "Analysis of the dynamic response of pump-turbine impellers. Influence of the rotor". In: *Mechanical Systems and Signal Processing* 68-69 (2016), pp. 330–341. ISSN: 0888-3270. DOI: 10.1016/j.ymssp.2015.05.034. URL: https://www.sciencedirect.com/science/article/pii/S0888327015002988 (cit. on pp. 43–46).

[48] Monica Egusquiza, Alexandre Tessier, Alexandre Presas, David Valentin, Yves St-Amant, and Sebastien Houde. "Experimental study on the detection of vibrations of an operating turbine runner with sensors on the casing". In: *Measurement* 248 (2025), p. 116773. ISSN: 0263-2241. DOI: 10.1016/j.measurement.2025.116773. URL: https://www.sciencedirect.com/science/article/pii/S0263224125001320 (cit. on pp. 43–46).

[49] International Design Engineering Technical Conferences, Computers, and Information in Engineering Conference, eds. *Fluid Added Mass Effect in the Modal Response of a Pump-Turbine Impeller*. Vol. Volume 1: 22nd Biennial Conference on Mechanical Vibration and Noise, Parts A and B. ASME. Aug. 2009, pp. 715–724. DOI: 10.1115/DETC2009-86830. eprint: https://asmedigitalcollection.asme.org/IDETC-CIE/proceedings-pdf/IDETC-CIE2009/48982/715/2772340/715_1.pdf. URL: https://doi.org/10.1115/DETC2009-86830 (cit. on pp. 44, 46).

[50] C.G. Rodriguez, E. Egusquiza, X. Escaler, Q.W. Liang, and F. Avellan. "Experimental investigation of added mass effects on a Francis turbine runner in still water". In: *Journal of Fluids and Structures* 22.5 (2006), pp. 699–712. ISSN: 0889-9746. DOI: 10.1016/j.jfluidstructs.2006.04.001. URL: https://www.sciencedirect.com/science/article/pii/S0889974606000338 (cit. on pp. 44, 45).

[51] Anup KC, Bhola Thapa, and Young-Ho Lee. "Transient numerical analysis of rotor–stator interaction in a Francis turbine". In: *Renewable Energy* 65 (2014). SI:AFORE 2012, pp. 227–235. ISSN: 0960-1481. DOI: https://doi.org/10.1016/j.renene.2013.09.013. URL: https://www.sciencedirect.com/science/article/pii/S0960148113004801 (cit. on p. 45).

[52] Chirag Trivedi and Michel J. Cervantes. "Fluid-structure interactions in Francis turbines: A perspective review". In: *Renewable and Sustainable Energy Reviews* 68 (2017), pp. 87–101. ISSN: 1364-0321. DOI: https://doi.org/10.1016/j.rser.2016.09.121. URL: https://www.sciencedirect.com/science/article/pii/S1364032116306335 (cit. on p. 45).

[53] Hiroshi Tanaka. "Vibration Behavior and Dynamic Stress of Runners of Very High Head Reversible Pump-turbines". In: *International Journal of Fluid Machinery and Systems* 4.2 (Apr. 2011). Review Paper (Invited), pp. 289–306. ISSN: 1882-9554. DOI: 10.5293/IJFMS.2011.4.2.289 (cit. on pp. 46, 47).

[54] Y. Kubota, T. Susuki, H. Tomita, T. Nagafuji, and T. Okamura. "Vibration of Rotating Bladed Disc Excited by Stationary Distributed Forces". In: *Bulletin of the JSME* 26 (1983), pp. 1952–1957 (cit. on pp. 47, 49).

[55] Anup KC, Bhola Thapa, and Young-Ho Lee. "Transient Numerical Analysis of Rotor–Stator Interaction in a Francis Turbine". In: *Renewable Energy* 65 (2014). SI:AFORE 2012, pp. 227–235. ISSN: 0960-1481. DOI: 10.1016/j.renene.2013.09.013. URL: https://www.sciencedirect.com/science/article/pii/S0960148113004801 (cit. on p. 50).

[56] NTNU Norwegian Hydropower Center. *Francis-99 Third Workshop (2019): Test case - Turbine / Test facility*. Online. Available at: https://www.ntnu.edu/nvks/f99-third-workshop (accessed: YYYY-MM-DD). 2019 (cit. on pp. 54–59, 61).

[57] Q. Zhu, X. Zhang, and H. Wang. "A review of machine learning applications for condition monitoring in hydropower plants". In: *Renewable and Sustainable Energy Reviews* 141 (2021), p. 110795. DOI: 10.1016/j.rser.2021.110795 (cit. on p. 73).

[58] S. Chakraborty, R. Kumar, and A. Jain. "Artificial intelligence and machine learning in hydropower: A review of recent advances". In: *Energy Reports* 8 (2022), pp. 3072–3085. DOI: 10.1016/j.egyr.2022.02.042 (cit. on p. 73).

[59] D. Valentín, C. Valero, A. Presas, M. Egusquiza, and E. Egusquiza. "Experimental investigation of a Francis turbine runner natural frequencies and its stability under operating conditions". In: *Mechanical Systems and Signal Processing* 79 (2016), pp. 39–54. DOI: 10.1016/j.ymssp.2016.02.049 (cit. on pp. 73, 75).

[60] J. Zhang, K. Ma, and Y. Liu. "Virtual sensing and deep learning for condition monitoring of rotating machinery: A survey". In: *Mechanical Systems and Signal Processing* 149 (2021), p. 107334. DOI: 10.1016/j.ymssp.2020.107334 (cit. on pp. 73, 75).

[61] Y. Li, T. Sun, and H. Guo. "Hybrid machine learning methods for hydropower unit fault diagnosis". In: *Applied Energy* 308 (2022), p. 118363. DOI: 10.1016/j.apenergy.2021.118363 (cit. on p. 73).

Dedications

Ai miei genitori, che hanno reso possibile questo straordinario percorso.

A mia sorella Iole, che è stata e sarà sempre la persona più importante della mia vita; senza di lei non sarei qui.

A mio fratello Walter, che ha svolto il fondamentale ruolo di fratello maggiore.

A mio nonno Sebastiano, maestro di vita, che mi ha trasmesso i valori del sacrificio, dell'impegno dell'umiltà e dell'onestà, a lui dedico questo traguardo.

A tutti i miei amici, vicini e lontani, che mi permettono di essere davvero me stesso e di sentirmi a casa.

A Matteo, compagno di avventure e di studi, con cui ho scoperto un nuovo lato dell'amicizia.

A tutte le persone che ho incontrato durante la mia esperienza Erasmus, i veri protagonisti delle mie giornate, che hanno reso quel periodo indimenticabile e ricco di significato.

A me stesso, per aver affrontato le mie paure, per aver resistito nei momenti difficili, quando stavo per arrendermi.